UNIVERSITÀ DEGLI STUDI DELL'INSUBRIA

Dipartimento di Scienza e Alta Tecnologia

Anno Accademico 2018-2019

Dottorato in Fisica ed Astrofisica XXXI Ciclo

THE PROTOTYPE PHASE OF THE ENUBET POSITRON TAGGER

Author: Claudia Brizzolari
ID number 727619

Tutor:	Prof.ssa Michela Prest
	Università degli Studi dell'Insubria
Co-Tutor:	Prof. Francesco Terranova
	Università degli Studi di Milano-Bicocca
Co-Tutor:	Dott. Valerio Mascagna
	Università degli Studi dell'Insubria
PhD Coordinator:	Prof. Massimo Caccia
	Università degli Studi dell'Insubria

Contents

Introduction

In particle physics, the study of neutrinos and their properties is a field of leading importance. One of the most interesting results is that neutrinos have a mass, albeit very small, in contrast with the predictions of the Standard Model, which theorized the neutrinos to be massless. This discovery, obtained from researches performed in the second half of the 20th century, represented the first deviation from the Standard Model, an indication that the world of the infinitely small has still lots to uncover. Moreover, neutrinos are also incredibly abundant particles in our Universe and further research on their properties could help to explain the asymmetry between matter and anti-matter.
To understand their role in this and other phenomena, such as the supernovae explosions, it is important to have a good knowledge of their interaction with the other particles of the Standard Model. This is where problems arise: not only the neutrinos have very small masses, but they only interact weakly via the weak force. The understanding of the way in which neutrinos interact with matter is directly linked to the knowledge of their cross section. Currently, the sensitivity on the cross section at energies $\sim$ GeV is limited to $O(10\%)$. The main factor of uncertainty is the knowledge of the initial neutrino flux; in conventional neutrino facilities, no direct measurement is possible and the flux has to be inferred from hadron production data and simulations.
The ENUBET Collaboration aims at demonstrating that a precision of the order of $O(1\%)$ on the absolute cross section is achievable by performing a direct measurement of the neutrino flux inside an instrumented decay tunnel. In the K_{e3} decay mode of K^+ ($K^+ \rightarrow \pi^0\ e^+\ \nu_e$) a positron is emitted alongside an electron neutrino. If the decay tunnel is short enough ($\sim$ 50 m) the K_{e3} is the only source of positrons. By counting the positrons it is possible to have a direct estimate of the electron neutrino flux inside the tunnel. The separation of the signal of the positrons from the background of pions is achieved instrumenting the decay tunnel with longitudinally segmented fast calorimeters. Shashlik calorimeters are sampling calorimeters in which the tiles of absorbing and scintillating material are crossed perpendicularly by the readout WaveLength Shifting fibers. This type of detector is cost effective, can be adapted to the geometry of the decay tunnel and is a well established technology. However, the fiber bundling at the end of the calorimeter strongly limits the granularity of the longitudinal sampling. The longitudinal segmentation is achieved by combining the

shashlik calorimeters with a compact readout based on SiPMs, embedded in the calorimeter bulk.
This thesis describes the experimental activity of the Collaboration during the period from July 2016 to October 2017 with a focus on my contribution to the data taking and analysis on different tagger prototypes.
In the first chapter a few elements of neutrino physics are given, along with the current knowledge of the neutrino cross sections in the different energy ranges.
The second chapter is dedicated to the neutrino beams. The first half of the chapter describes the technology of conventional neutrino beams, including how a neutrino beam is obtained, starting from the primary protons, the seconday pions and the tertiary muon neutrinos, and a summary of the flux monitoring techniques for primary and secondary particles. In the second half of the chapter the focus is on the ENUBET facility. The project involves the development of both the beamline and the instrumented decay tunnel. Starting from a conventional technology, the ENUBET beamline will focus kaons, in order to obtain a beam of electron neutrinos. A description of the decay tunnel and the techniques of particle identification used to separate the positrons from the background of tertiary pions is given.
The third chapter provides an overview of the modular technology chosen for the tagger and reports the results of the feasibility test performed in August 2015.
The fourth chapter is the heart of this thesis and describes in detail my contribution to the ENUBET project. In a 15 month period, an intense activity of prototyping has taken place. The goal for 2016 was to validate the use of the modular technology described in chapter three for the ENUBET project. In 2017, the collaboration worked to check the survival of the SiPMs to the radiation expected in the decay tunnel and to explore new materials in order to simplify and reduce the costs of the detector assembly. The chapter starts with a description of how the beam tests were performed. All the prototypes were tested at the CERN PS-T9 beamline and both the experimental setup and the data acquisition were kept mostly unchanged from one test to another. The data analysis steps common to all the prototypes are also described. The details of each prototype design and the results in terms of linearity and energy resolution are presented.
In the conclusive chapter, the prototype phase results are summarized and the modifications with respect to the original design are presented together with the future steps of the project.

Chapter 1

Neutrinos

Neutrinos are particles with small masses, several orders of magnitude smaller than all other fermions, but non-zero, and interact with matter only via the weak force. They also interact rarely: for example, there is a probability of $\sim 10^{-18}$ that a neutrino produced by a nuclear reactor with energy $E_\nu \sim$1 MeV interacts in a solid 1 m thick detector [1], corresponding to a cross section $\sigma \sim 10^{-44}\text{cm}^2$. In addition to be elusive, they are also incredibly abundant. Cosmological neutrinos have an average density of $n_\nu \simeq 336$ cm^{-3}, probably larger inside our galaxy due to the gravitational clustering effect. Nuclear reactions inside the Sun produce so many neutrinos that every second, a square centimeter of our body is crossed by 60 billions of them [1].
An in-depth study of their nature could uncover physics beyond the Standard Model and answer some cosmological questions, such as the predominance of matter over antimatter.
This chapter will provide a brief introduction to neutrino physics (for a complete treatment, see [1] and [2]), and the physics case of the ENUBET project.

1.1 A brief historical overview

Being so elusive and "ghost like", it does not come as a surprise that the first time the neutrinos made the world aware of their presence was in the form of an enigma [2]. In the 1920s the study of the radioactive beta decay highlighted that something was missing in the understanding of the process.
In a radioactive β-decay,

$$ {}^{A}_{Z}X \rightarrow {}^{A}_{Z+1}X' + e^- + \text{nothing else visible} \tag{1.1} $$

an electron is emitted with an expected energy equal to the difference of the parent and daughter nuclear mass, Q. The observed electron spectrum, however, is continuous with an end-point at Q, in what looks like a violation of the law of energy conservation (Fig. 1.1).

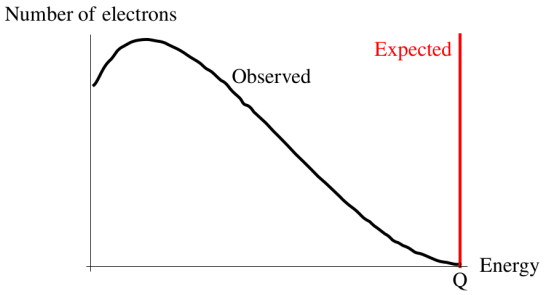

Figure 1.1: Electron spectrum of β-decay [2].

In 1930 Wolfgang Pauli proposed that in a radioactive β-decay a light, neutral particle was emitted along with the electron. Initially named "neutron", name later used for the particle of mass similar to the proton and no charge that resides inside the nucleus of atoms discovered by James Chadwick in 1932, it acquired its final name "neutrino" thanks to Enrico Fermi, one of the first to support Pauli's hypothesis [3]. Fermi also constructed his β-decay theory, depicted in Fig. 1.2, starting from this very hypothesis.

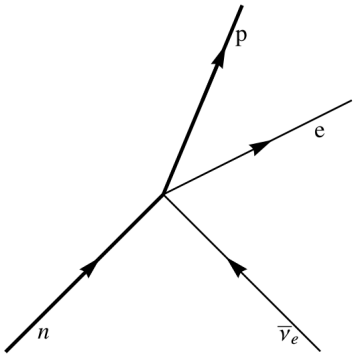

Figure 1.2: Fermi four-fermion coupling responsible for β-decay [2].

In this interaction, neutrinos are also implied to scatter off matter via the inverse beta process, $\overline{\nu}p \rightarrow ne^+$. The cross section for this decay, as estimated by Bethe and Peierls [4], is:

$$\sigma_{\overline{\nu}} \leq 10^{-44}\text{cm}^2, E_{\overline{\nu}} \simeq 2 \text{ MeV} \tag{1.2}$$

so small that processes of this kind were at first deemed as impossible to observe. However, Pontecorvo estimated that it was possible to get a few events per day in a ton-mass scale detector and a neutrino flux of $10^{11}\nu$ cm^{-2} s^{-1} [5]. By constructing detectors at a few tens of meters from standard nuclear reactors, Reines and Cowen, in 1956, managed to have the right neutrino flux and were able to detect them via the inverse beta decay [6, 7]. This experiment led to the discovery of anti-neutrinos. The detector used by Reines and Cowen

was a tank filled with a mixture of liquid scintillator and cadmium. PhotoMultiplier Tubes (PMT) were placed on the tank walls to read the scintillating light (Fig. 1.3).

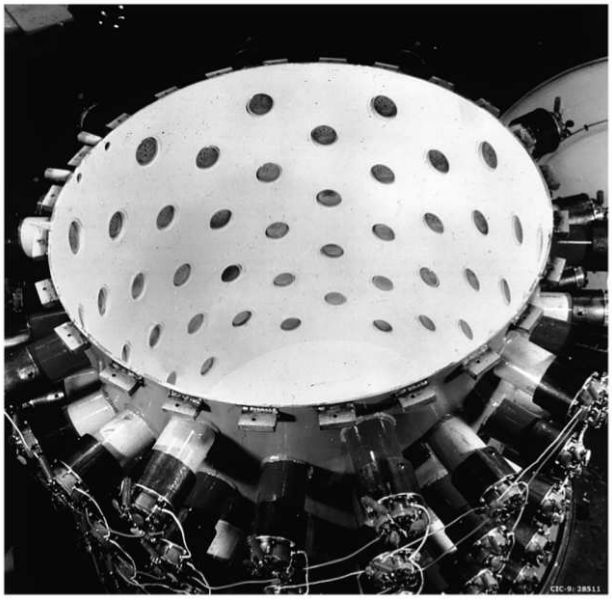

Figure 1.3: The scintillation detector for the 1953 neutrino detection experiment at Hanford [8].

The presence of antineutrinos produced by the nuclear reactor was detected by searching for the double signature of the inverse beta decay. The interaction between the antineutrino with a proton of the scintillator produced a positron and a neutron (Fig. 1.4). The positron annihilated with an electron, emitting two gamma rays in opposite directions and causing the scintillator to produce a flash of visible light, collected by the PMTs. The neutron travelled in the mixture until it was captured by a cadmium nucleus, which released 9 MeV in gamma rays, again detected by the PMTs as visible light produced by the scintillators a few microseconds after the first one (Fig. 1.5).

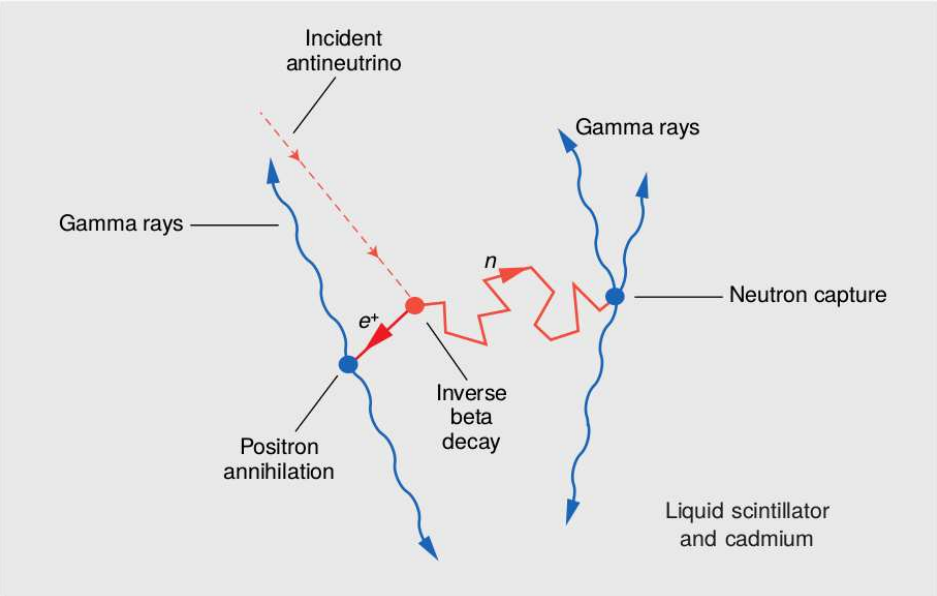

Figure 1.4: An incident antineutrino (red dashed line) interacts with a proton through the weak force. The antineutrino turns into a positron (e^+), and the proton turns into a neutron (n) [9].

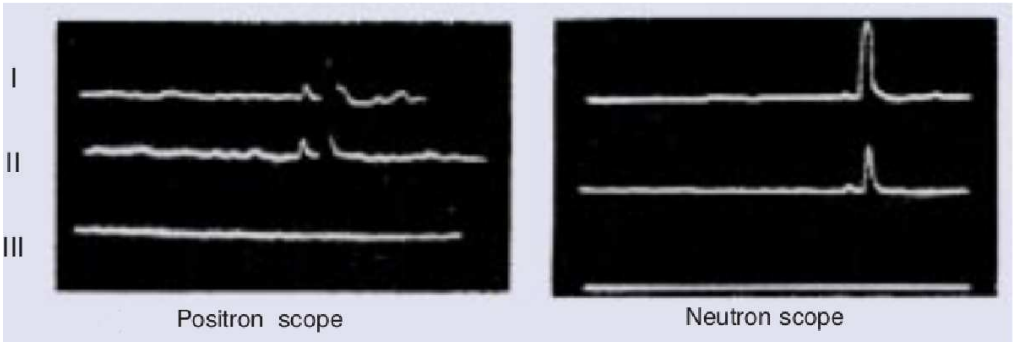

Figure 1.5: Oscilloscope traces from the Savannah river experiments. In these experiments three detectors were employed (labelled I, II, III). The delayed-coincidence signal appears in detectors I and II. Positron scope: the pulse signals in detectors I and II were 0.30 MeV and 0.35 MeV respectively. The pulses reached the positron circuit in prompt coincidence (less than 0.2 μs apart). Neutron scope: the pulse energies in detectors I and II were 5.8 MeV and 3.3 MeV respectively. These signals arrived in prompt coincidence and 2.5 μs delayed from the positron ones [9].

1.2 Neutrino flavours

Along with the electron neutrino and its corresponding antiparticle, the Standard Model includes two other neutrino flavours with their antiparticles, the muon and the tau neutrinos. All the neutrinos are named after their corresponding charged leptons. Neutrinos can couple with a Z_0 boson (neutral current, NC, interactions), which changes their quadrimomentum but does not change their identity, or with a $W^{\pm}$ boson (charged current, CC, interactions), which mediates the neutrino absorption and emission by or with one of the charged leptons, $e^{\pm}$, $\mu^{\pm}$, $\tau^{\pm}$. The flavour of a neutrino is defined by the charged lepton connected to the same charged vertex:

$$W^+ \to l^+ + \nu_l \tag{1.3}$$

$$W^- \to l^- + \overline{\nu}_l \tag{1.4}$$

where $l = e,\ \mu,\ \tau$.

Muon neutrinos The muon was discovered in the 1930s [10] in the cosmic rays and was later understood to be a heavier version of the electron. For muons, the analogous decay of the β-decay is the pion decay:

$$\pi^- \to \mu^- + \overline{\nu}_\mu \tag{1.5}$$

The undetected particle in this decay was different from the one in the β-decay. This was assessed experimentally in 1962 by L. Lederman, M. Schwarz and J. Steinberger [11], with the first accelerator neutrino beam (Fig. 1.6). The primary 15 GeV/c proton beam impinged on a beryllium target producing pion secondaries and their decay was the source of the neutrino beam.
The goal of the experiment was to study two different interactions with nucleons:

$$\nu_\mu + N \to \mu^- + X \tag{1.6}$$

$$\nu_\mu + N \to e^- + X \tag{1.7}$$

The only reaction observed was the first one (Eq. 1.6), indicating that ν_μ and ν_e are different particles.

Tau neutrinos A third charged lepton, τ^-, was discovered in 1975 at Stanford and ν_τ is the associated neutrino. ν_τ and $\overline{\nu}_\tau$ are expected to be produced in $\tau^{\pm}$ decays:

$$\tau^- \to \nu_\tau + W^- \tag{1.8}$$

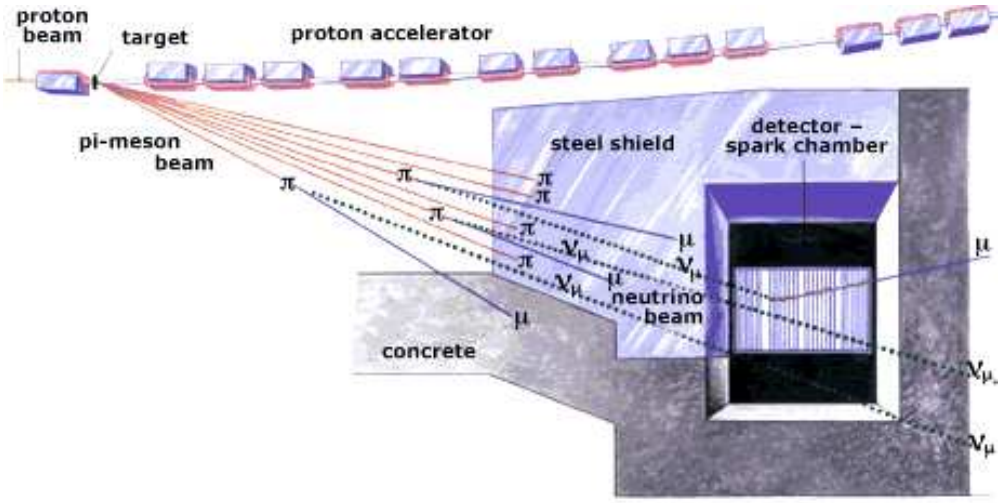

Figure 1.6: Part of the circular accelerator in Brookhaven, in which the protons were accelerated. The π secondaries, produced in the target, decayed into μ and ν_μ. All particles were shielded except the neutrinos. A very small fraction of the neutrinos then reacted in the detector and gave rise to muons, detected by the spark chamber [12].

$$\tau^- \to \nu_\tau + e^- + \overline{\nu}_e \tag{1.9}$$

$$\tau^- \to \nu_\tau + \mu^- + \overline{\nu}_\mu \tag{1.10}$$

For the three neutrino flavours, upper limits of the masses have been measured via kinematic effects on the end-point (Fig. 1.7) of the lepton energy spectrum in weak decays [2]:

- the most stringent limit, the one for the electron neutrino, has been obtained from the β-decay of tritium and the best estimate is given by the combination of the results of the Mainz and Troitsk experiments [13]:

$$m_{\nu_e} < 2 \text{ eV} (95\% \text{ CL}) \tag{1.11}$$

- the limit on the ν_μ [14] is:

$$m_{\nu_\mu} < 170 \text{ keV} (90\% \text{ CL}) \tag{1.12}$$

  obtained from the end-point spectrum of the $\pi^+ \to \mu^+ \nu_\mu$ decay;

- for the ν_τ the mass limit was obtained at LEP [15]:

$$m_{\nu_\tau} < 18.2 \text{ MeV} (95\% \text{ CL}) \tag{1.13}$$

  from the $\tau \to 5\pi\nu_\tau$ decay.

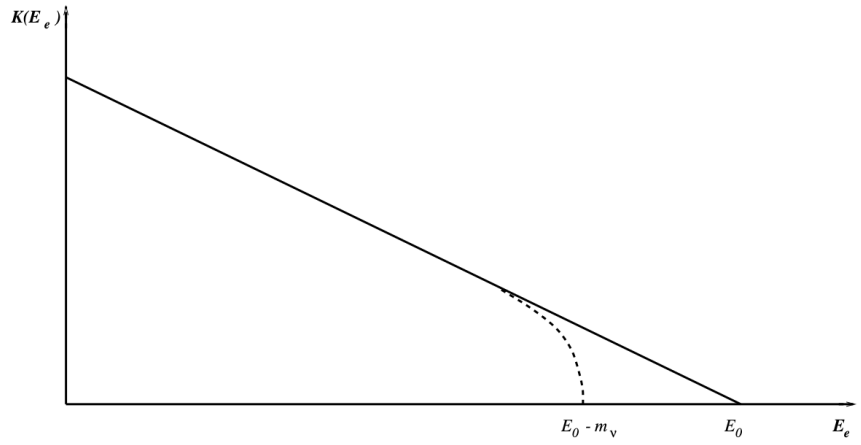

Figure 1.7: Effect of a neutrino mass in the end-point of the lepton energy spectrum in a β-decay [2].

1.3 Dirac or Majorana particles

Quarks and charged leptons are called "Dirac" particles because they are not their own anti-particle. A "Majorana" particle, on the other hand, is also its own anti-particle. Neutrinos have not yet been categorized into "Dirac" or "Majorana" particles. Experimentally, neutrinos emitted in a β-decay ($\overline{\nu}_e$) are not captured in reactions caused by ν_e. For example, after a neutron decay

$$n \rightarrow p + e^- + \overline{\nu}_e \tag{1.14}$$

the reaction

$$\overline{\nu}_e + {}^{37}\mathrm{Cl} \rightarrow {}^{37}\mathrm{Ar} + e^- \tag{1.15}$$

is not observed, while $\nu_e + {}^{37}\mathrm{Cl} \rightarrow {}^{37}\mathrm{Ar} + e^-$ is observed in nature. This does not rule out the "Majorana" hypothesis, because the reaction in Eq. 1.15 might have not been observed yet due to a strong dynamical suppression ($\sim (m_\nu/E)^2$). Neutrinoless double beta decay would be an interesting reaction to distinguish between Dirac and Majorana neutrinos [16]:

$$(Z,A) \rightarrow (Z+2,A) + 2e^- + 2\overline{\nu}_e (2\nu\beta\beta) \tag{1.16}$$

Double beta decays (Eq. 1.16) can occur when the single beta decay is kinematically forbidden. For example, a single beta decay cannot occur in a nucleus of ^{76}Ge, $Z = 32$, and end into the $Z = 33$ state, because the resulting nucleus, ^{76}As, has a mass 0.4 MeV larger. However, a double beta decay into the state $Z = 34$ produces a ^{76}Se nucleus, that is 3.05 MeV lighter. A neutrino-less double beta decay (Eq. 1.17) would occur if the neutrino is a massive Majorana particle:

$$(Z,A) \rightarrow (Z+2,A) + 2e^{-}(0\nu\beta\beta) \tag{1.17}$$

1.4 Oscillations

Neutrino oscillations were first theorized by Bruno Pontecorvo [1]. The phenomenon of neutrino oscillations describes the probability for a neutrino created with a given flavor to be in the same state later in time. This is a phenomenon given by quantum mechanics. The weak-eigenstates, ν_e, ν_μ, ν_τ, produced in charged-current weak interactions, do not have a well defined mass, but a linear superposition of three states ν_1, ν_2, and ν_3 with their masses m_1, m_2, and m_3. In formula:

$$|\nu_\alpha\rangle = \sum_j U^*_{\alpha j} |\nu_j\rangle \tag{1.18}$$

where the greek indices indicate the flavor and the latin ones are for the mass eigenstates; U is the Pontecorvo-Maki-Nakagawa-Sakata (PMNS) matrix. The U matrix is unitary from the fact that the three flavor (and mass) eigenstates are orthogonal to each other. Flavors are a periodical function of time and flavor oscillation means that, for a ν_e produced at point A, a measurement close to A will produce a e^-, but a measurement at a point B, more distant, will produce a μ^- or a τ^-. To become non-zero, the probability of oscillation necessitates long distances to occur. The reason is that neutrino masses are close to each other, so a longer time is needed to have the required phase differences between different components; in addition, neutrinos travel at speeds close to the speed of light.

1.4.1 Two flavour case

In the case of the mixing of only two neutrino flavors (ν_e and ν_μ), there are two mass eigenstates (ν_1 and ν_2) and two mass eigenvalues (m_1, m_2) and Eq. 1.18 becomes:

$$\begin{bmatrix} |\nu_e\rangle \\ |\nu_\mu\rangle \end{bmatrix} = \begin{bmatrix} c & s \\ -s & c \end{bmatrix} \begin{bmatrix} |\nu_1\rangle \\ |\nu_2\rangle \end{bmatrix} \tag{1.19}$$

where $c = \cos\theta$, $s = \sin\theta$, with θ the mixing angle. A neutrino created at time $t = 0$ with momentum p has an initial state:

$$|\nu(t=0)\rangle = |\nu_e\rangle = c|\nu_1\rangle + s|\nu_2\rangle \tag{1.20}$$

The two mass components m_1 and m_2 have energies E_1 and E_2:

$$E_i = \sqrt{p^2 + m_i^2} \simeq p + \frac{m_i^2}{2p} \simeq E + \frac{m_i^2}{2E} \tag{1.21}$$

The state of the neutrino, after a time $t \neq 0$, is:

$$|\nu(t)\rangle = ce^{-iE_1 t}|\nu_1\rangle + se^{-iE_2 t}|\nu_2\rangle \tag{1.22}$$

The two components have a phase difference, resulting in a non-trivial flavor evolution of the neutrino. The probability that the neutrino is found at a later time with the muon flavor is:

$$\begin{aligned} P(\nu_e \to \nu_\mu; t) &= |\langle \nu_\mu | \nu(t) \rangle|^2 \\ &= |\{-s\langle \nu_1| + c\langle \nu_2|\}|\nu(t)\rangle|^2 \\ &= c^2 s^2 |e^{-iE_2 t} - e^{-iE_1 t}|^2 \\ &= 2c^2 s^2 \{1 - \cos[(E_2 - E_1)t]\} \\ &= \sin^2 2\theta \sin^2 [\frac{\Delta m^2}{4E} t] \end{aligned} \tag{1.23}$$

where $\Delta m^2 = m_2^2 - m_1^2$. If the neutrinos are relativistic it is possible to approximate $L \simeq t$. Equation 1.23 can be rewritten as:

$$P(\nu_e \to \nu_\mu; L) = \sin^2 2\theta \sin^2 [1.27 \Delta m^2 \frac{L}{E}] \tag{1.24}$$

in which L is in meters and E is in MeV (or, respectively, km and GeV).

1.4.2 CP and T violating effects

In the three flavor case, the U mixing matrix is parametrized as follows: 3 mixing angles, one CP violating phase and 2 additional "Majorana phases" if the neutrinos are Majorana particles. The two Majorana phases have no influence on the flavor evolution, so the matrix U is written as:

$$\begin{aligned} U &= \begin{pmatrix} 1 & 0 & 0 \\ 0 & c_{23} & s_{23} \\ 0 & -s_{23} & c_{23} \end{pmatrix} \begin{pmatrix} c_{13} & 0 & s_{13}e^{-i\delta} \\ 0 & 1 & 0 \\ -s_{13}e^{i\delta} & 0 & c_{13} \end{pmatrix} \begin{pmatrix} c_{12} & s_{12} & 0 \\ -s_{12} & c_{12} & 0 \\ 0 & 0 & 1 \end{pmatrix} \\ &= \begin{pmatrix} c_{12}c_{13} & s_{12}c_{13} & s_{13}e^{-i\delta} \\ -s_{12}c_{23} - c_{12}s_{13}s_{23}e^{i\delta} & c_{12}c_{23} - s_{12}s_{13}s_{23}e^{i\delta} & c_{13}s_{23} \\ s_{12}s_{23} - c_{12}s_{13}c_{23}e^{i\delta} & -c_{12}s_{23} - s_{12}s_{13}c_{23}e^{i\delta} & c_{13}c_{23} \end{pmatrix} \end{aligned} \tag{1.25}$$

where $\theta_{12}, \theta_{13}, \theta_{23}$ are the mixing angles, $c_{jk} = \cos\theta_{jk}$, $s_{jk} = \sin\theta_{jk}$ and δ is the CP violating phase. The neutrino oscillation probability can violate the CP or T symmetry, that is:

$$P(\nu_\alpha \to \nu_\beta) \neq P(\overline{\nu}_\alpha \to \overline{\nu}_\beta) \tag{1.26}$$

$$P(\nu_\alpha \to \nu_\beta) \neq P(\nu_\beta \to \nu_\alpha) \tag{1.27}$$

For comparison, the *CPT* theorem imposes (in vacuum) the condition:

$$P(\nu_\alpha \to \nu_\beta) = P(\overline{\nu}_\beta \to \overline{\nu}_\alpha) \tag{1.28}$$

The general (3 flavor) oscillation probability is written as:

$$\begin{aligned} P(\nu_\alpha \to \nu_\beta) &= |\sum_j U_{\beta j} U^*_{\alpha j} e^{-im_j^2 \frac{L}{2E\nu}}|^2 \\ &= \sum_{j=1,3} |U_{\beta j}|^4 |U_{\alpha j}|^4 \\ &+ \sum_{j<k} 2\mathrm{Re}[U_{\beta j} U^*_{\beta k} U^*_{\alpha j} U_{\alpha k}] \cos\left(\frac{\Delta m^2_{jk} L}{2E}\right) \\ &+ \sum_{j<k} 2\mathrm{Im}[U_{\beta j} U^*_{\beta k} U^*_{\alpha j} U_{\alpha k}] \sin\left(\frac{\Delta m^2_{jk} L}{2E}\right) \end{aligned} \tag{1.29}$$

in which $\Delta m^2_{jk} = m^2_k - m^2_j$. A CP transformation is achieved by substituting the neutrinos with anti-neutrinos in the oscillation probability equation. In this case the U matrix is substituted with its complex conjugate U^* in Eq. 1.29. In the resulting equation, the "sin" terms change sign while the "cos" terms remain invariant. The CP symmetry is violated if the mixing matrix has a non vanishing imaginary part, so if $\delta \neq 0, \pi$. The time reversed channel in this case is simply the transition $\nu_\beta \to \nu_\alpha$ and the oscillation probability for this case is obtained by changing the indices $\alpha \leftrightarrow \beta$ in Eq. 1.29. This changes the sign of only the "sin" terms, leaving the "cos" ones invaried. As in the previous case, the T reversal simmetry is violated if U has a non vanishing imaginary part, or, equivalently, if $\delta \neq 0, \pi$.

1.5 Cross section across the energies

In the 20th century, the discovery that the neutrinos are not massless was probably the first indication that the Standard Model was not a complete description of the particle realm and that there is physics beyond it. Now, in the 21st century, the study of neutrinos and their properties is a strong and active area of research. One particularly interesting hypothesis that is being investigated is the role that neutrinos might have played in the observed asymmetry between matter and antimatter in our Universe. To undestand this, it is important to study how neutrinos interact with the other particles of the Standard Model, that is, to have a solid knowledge of the cross sections at different energy ranges [17].

1.5.1 Threshold-less processes: $E_\nu \sim 0-1$ MeV

Threshold-less processes are those involving a neutrino that has zero or almost zero momentum. The possible interactions are coherent scattering and neutrino capture. Neutrino-nucleus interactions were theorized by Freedman, Schramm and Tubbs [18] after the discovery of neutral currents. In a coherent scattering a neutrino interacts coherently with the nucleus with a neutral current exchange:

$$\nu + A_N^Z \rightarrow \nu + A_N^{*Z} \tag{1.30}$$

The cross section for this process grows as the square of the atomic number A^2. This reaction has a strong coherent enhancement, but despite that, it is extremely difficult to detect experimentally. One reason is that the energies of the emitted recoil product are extremely small and hence very complicated to observe. The COHERENT Collaboration [19] performed a measurement of the coherent elastic neutrino-nucleus scattering (CEνES) with a Sodium activated Cesium Iodide (CsI[Na]) crystals detector. With 134 ± 22 observed events at 6.7σ confidence level, the results were consistent with the SM prediction of 173 events, with the $\sim 28\%$ uncertainty dominated by the quenching factor of the CsI[Na].
Neutrino capture is a process similar to the one of the ordinary beta decay and it is sometimes named "enhanced" or "stimulated beta emission". As opposed to the ordinary beta decay, the neutrino is interacting with the target nucleus:

$$\nu_e + A_N^Z \rightarrow e^- + A_{N-1}^{Z+1} \tag{1.31}$$

producing the same observable final states as the ordinary beta decay. The difference between the two processes is that the neutrino capture is exothermic, requiring no energy to initiate the reaction. This low energy process is of great cosmological interest, as it is considered a way to detect cosmological neutrinos [20]. Theorized in 1962 by Weinberg [21], it has recently gained attention also thanks to the advancement of beta decay experiments, which have extended the reach on neutrino mass scales. Unlike the coherent scattering, this process has not been detected yet.

1.5.2 Low energy nuclear processes: $E_\nu \sim 1-100$ MeV

While neutrinos with threshold energies can interact with the nucleus as if it were a single, coherent structure, by increasing the energy the neutrino starts to see each nucleon individually and interact with it via the inverse beta decay:

$$\overline{\nu}_e + p \rightarrow e^+ + n \tag{1.32}$$

Unlike the previously described mechanisms, this one has been studied extensively in neutrino experiments. The inverse beta decay has been studied in detail both theoretically [4]

and experimentally [22]. Neutrinos produced from fission in nuclear reactors have been historically used to study this reaction. The typical range for the neutrino energy is from the threshold $E_\nu \geq 1.806$ MeV to 10 MeV, although slightly higher energies (10-20 MeV) are of great interest, as this reaction in this energy range is important to understand the supernova explosion mechanism. Theoretically, the inverse beta decay cross section has been predicted with uncertainties around $\pm 0.5\%$.
Neutrinos cross sections in this energy range are an important parameter in many different models, for example reactor neutrino analysis, supernova modelling and neutrino oscillation tests. It is worth remembering that the inverse beta decay was the reaction with which the neutrinos were first detected [7, 23], and, after 60 years, inverse beta decay and neutrino absorption are still the most exploited reactions for detecting reactor and solar neutrinos. However, the experimental data collected for the study of neutrino cross sections is still limited. Most of the studies of neutrino interactions with hydrogen (protons) are performed in reactors experiments; in this case neutrinos are the product of the fission of ^{235}U, ^{238}U, ^{239}Pu and ^{241}Pu. These experiments have been performed, for example, at ILL-Grenoble, [24, 25], Gösgen [26], ROVNO [27] and Krasnoyarsk [28]. In addition to these, it is worth to cite Bugey [29, 30] on its own, as it is the experiment which gave the most precise determination of the cross section. The major source of uncertainty was, in most cases, the determination of the neutrino flux. In Table 1.1 the experimental cross sections are compared with the theoretical predictions.
Experiments have been performed using deuterium too. The most important example is the Sudbury Neutrino Observatory [32], in which heavy water is used as the main target to study charged and neutral current interaction of neutrinos from ^8B produced in the solar core. At the Clinton P. Anderson Meson Physics Facility (LAMPF) the measurement of the reaction $\nu_e d \to e^- pp$ [33] gave for the cross section $\langle \sigma_\nu \rangle = (0.52 \pm 0.18) \times 10^{-40}\text{cm}^2$, which is in good agreement with the theoretical predictions. Table 1.2 summarizes the cross sections on deuterium from short baseline (< 100 m) reactor experiments.

1.5.3 Intermediate energy cross section: $E_\nu \sim 0.1 - 20$ GeV/c

Going up in energies, different mechanisms appear for the description of neutrino scattering. They can be divided into three main categories:

- elastic and quasi-elastic scattering: in this scattering neutrinos interact with a nucleon freeing one nucleon (or multiple nucleons) from the target. In the case of charged-current scattering the process is called "quasi-elastic scattering", while if neutral-current is involved it is known as "elastic scattering";

- resonance production: the interaction with a neutrino can cause a nucleon to reach a resonance state (Δ, N^*), which decays to a variety of mesonic final states;

Experiment	Fuel composition				Distance	$\sigma_{exp}/\sigma_{theo.}$
	^{235}U	^{239}Pu	^{239}U	^{241}Pu		
ILL [24, 25]	93%	-	-	-	9 m	$0.800(0.832) \pm 0.028 \pm 0.071$
Bugey [30] 94	53.8%	32.8%	7.8%	5.6%	15 m	$0.987(0.943) \pm 0.014 \pm 0.027$
Bugey [29] 95	53.8%	32.8%	7.8%	5.6%	15 m	$0.988(0.943) \pm 0.037 \pm 0.044$
Bugey [29] 95	53.8%	32.8%	7.8%	5.6%	40 m	$0.994(0.948) \pm 0.010 \pm 0.045$
Bugey [29] 95	53.8%	32.8%	7.8%	5.6%	95 m	$0.915(0.873) \pm 0.10 \pm 0.041$
Gösgen [26] I	61.9%	27.2%	6.7%	4.2%	37.9 m	$1.018(0.971) \pm 0.017 \pm 0.06$
Gösgen [26] II	58.4%	29.8%	6.8%	5.0%	45.9 m	$1.045(0.997) \pm 0.019 \pm 0.06$
Gösgen [26] III	54.3%	32.9%	7.0%	5.8%	64.7 m	$0.975(0.930) \pm 0.033 \pm 0.06$
ROVNO [27]	61.4%	27.5%	3.1%	7.4%	18 m	$0.985(0.940) \pm 0.028 \pm 0.027$
Krasnoyarsk [28] I	99%	-	-	-	33 m	$1.013(0.944) \pm 0.051$
Krasnoyarsk [28] II	99%	-	-	-	57 m	$0.989(0.954) \pm 0.041$
Krasnoyarsk [28] III	99%	-	-	-	33 m	$1.013(0.960) \pm 0.20$

Table 1.1: Measured inverse beta decay cross sections from short baseline (< 100 m) reactor experiments. Theoretical predictions include original estimates, while in parenthesis the recalculated ones from [31] are reported.

Experiment	Measurement	$\sigma_{fission}$ (10^{-44} cm^2/fission)	$\sigma_{exp}/\sigma_{theo.}$
Savannah River [34]	$\overline{\nu}_e$CC	1.5 ± 0.4	0.7 ± 0.2
ROVNO [35]	$\overline{\nu}_e$CC	1.17 ± 0.16	1.08 ± 0.19
Krasnoyarsk [36]	$\overline{\nu}_e$CC	1.05 ± 0.12	0.98 ± 0.18
Bugey [37]	$\overline{\nu}_e$CC	0.95 ± 0.20	0.97 ± 0.20
Savannah River [34]	$\overline{\nu}_e$NC	3.8 ± 0.9	0.8 ± 0.2
ROVNO [35]	$\overline{\nu}_e$NC	2.71 ± 0.47	0.92 ± 0.18
Krasnoyarsk [36]	$\overline{\nu}_e$NC	3.09 ± 0.30	0.95 ± 0.33
Bugey [37]	$\overline{\nu}_e$NC	3.15 ± 0.40	1.01 ± 0.13

Table 1.2: Measured charged current ($\overline{\nu}_e$CC) and neutral current ($\overline{\nu}_e$NC) neutrino cross sections on deuterium from short baseline (< 100 m) reactor experiments. The comparison with theory is taken from [36].

- deep inelastic scattering: with enough energy, a neutrino can interact with the individual quark constituents of the nucleon. When this happens, the interaction produces a hadronic shower.

Given the variety of possible processes, the output of a neutrino interaction includes different final states, that go from the emission of nucleons to the emission of pions, kaons and mesons (Fig. 1.8).

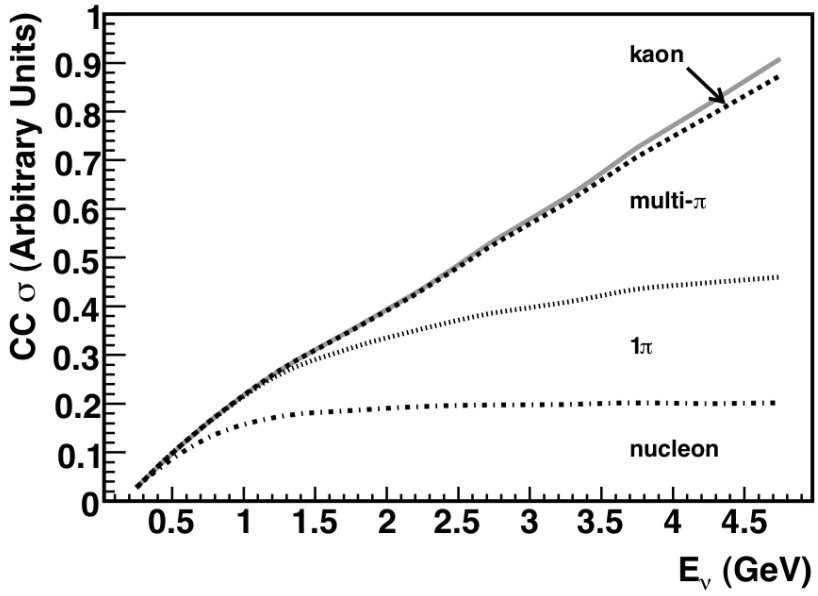

Figure 1.8: Predicted processes to the total CC inclusive scattering cross section at intermediate energies [17].

This energy regime is a sort of a transition regime between the quasi-elastic scattering and the deep inelastic scattering. Adequate descriptions of the three processes listed above have been formulated, but currently there is no uniform description on how they combine and the transition from one to another.

Figure 1.9 summarizes the existing measurements of CC neutrino and antineutrino cross sections in the intermediate energy range, accumulated with different experiments through the decades.

Data for the neutrino cross sections at these energies have been collected mostly in experiments that provided quite small data samples (from $\sim$ 10 to $\sim$ 1000 events) during the '70s and the '80s, using bubble chamber or spark chamber detectors. However, the discovery of neutrino oscillations and the advent of higher intensity neutrino beams renewed the interest in this energy range. New experiments such as ArgoNeuT, K2K, MiniBooNE, MINERνA, MINOS, NOMAD, SciBooNE, and T2K are aimed at studying this energy region in greater detail. The improved experimental measurements and theoretical calculations will play an

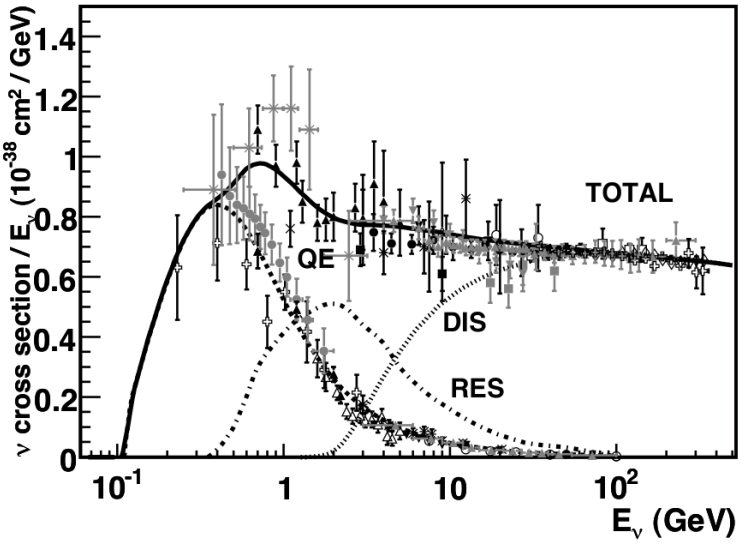

(a) Neutrino cross section

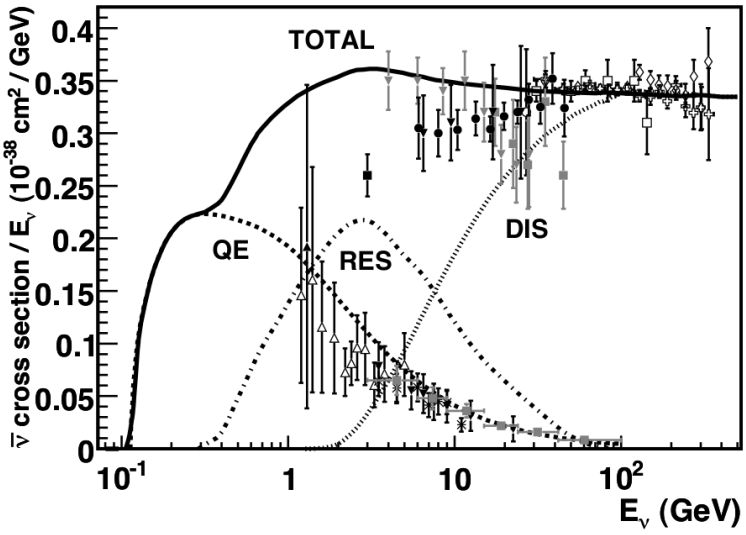

(b) Antineutrino cross section

Figure 1.9: Total neutrino and antineutrino per nucleon CC cross sections (for an isoscalar target) divided by neutrino energy and plotted as a function of the energy. These contributions include quasi-elastic scattering (dashed), resonance production (dot-dash) and deep inelastic scattering (dotted) [17].

important role in reducing the systematics for future neutrino oscillation experiments, but the updated cross section measurements will need to be backed by a precise knowledge of the incoming neutrino flux.

1.5.4 High energy cross section: $E_\nu \sim 20 - 500$ GeV/c

In this energy range, a neutrino can really interact with individual quarks inside a nucleon via the process called deep inelastic scattering (DIS). The CC cross section for neutrinos with these energies is shown in Fig. 1.10. Results from more recent experiments (NOMAD, NuTeV and MINOS) are compared to historical data. It is important to notice that in this region the CC cross section is measured with a precision of a few percent. The cross section has a linear dependence on the neutrino energy at these energies, which confirms the quark parton model predictions.

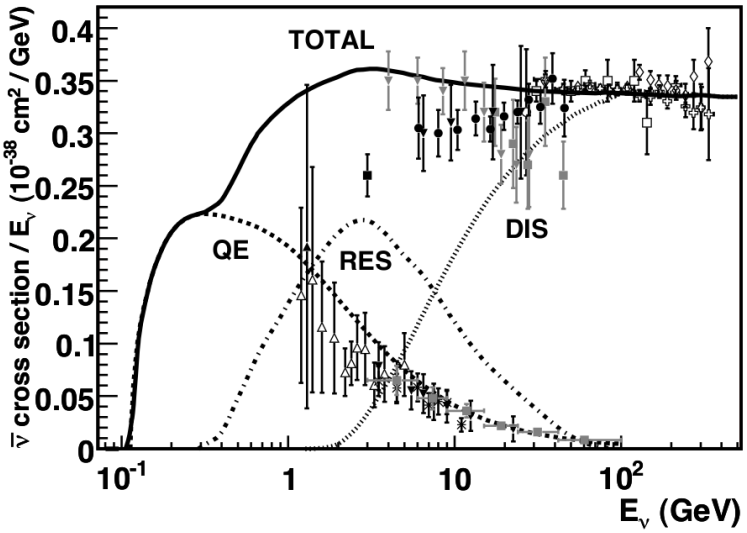

Figure 1.10: Measurements of the inclusive neutrino and antineutrino CC cross sections ($\nu_\mu N \to \mu^- X$ and $\overline{\nu}_\mu N \to \mu^+ X$) divided by the neutrino energy plotted as a function of the neutrino energy [17]. N is an isoscalar nucleon within the target. The dotted lines indicate the world-averaged cross sections, $\sigma_\nu/E_\nu = (0.677 \pm 0.014) \times 10^{-38}$ cm^2/GeV and $\sigma_{\overline{\nu}}/E_\nu = (0.334 \pm 0.008) \times 10^{-38}$ cm^2/GeV, for neutrinos and antineutrinos respectively [38].

1.5.5 Ultra high energy cross section: $E_\nu \sim 0.5$ TeV $- 1$ EeV

Being able to detect and study neutrinos with energies of the order of 10^{15} eV and higher could provide additional information on a variety of astrophysical mechanisms that have currently been observed only in the electromagnetic spectrum and via emission of hadrons. Thanks to the latest technological advancements, this energy range is currently being explored. The techniques used to detect these ultra high energy neutrinos include induced

events in large volumes of water (Baikal [39, 40], ANTARES [41], ice (AMANDA [42], IceCube [43], RICE [44], FORTE [45], ANITA [46]), the Earth's atmosphere (Pierre Auger [47], HiRes [48]) and the lunar regolith (GLUE [49]).
In particular, the IceCube Collaboration measuread the flux of neutrinos with energies above 1 TeV from different sources [50]: in Fig. 1.11, the blue plot indicates the flux due to muon neutrinos and antineutrinos from pion and kaon decay in cosmic ray interactions in the Earth's atmosphere and, since no events are registered from a prompt atmospheric neutrino flux from charm meson decays, a limit is shown in green. The salmon color area indicates the astrophysical neutrino flux from muon neutrino events originating in the northern hemisphere [51]. The neutrino cross section, determined from well reconstructed muon neutrino events and including both neutral and charged current interactions, is $1.30 \pm^{+0.21}_{-0.19}\,(\text{stat.}) \pm^{+0.39}_{-0.43}\,(\text{syst.})$ times the Standard Model predictions (Fig. 1.12).

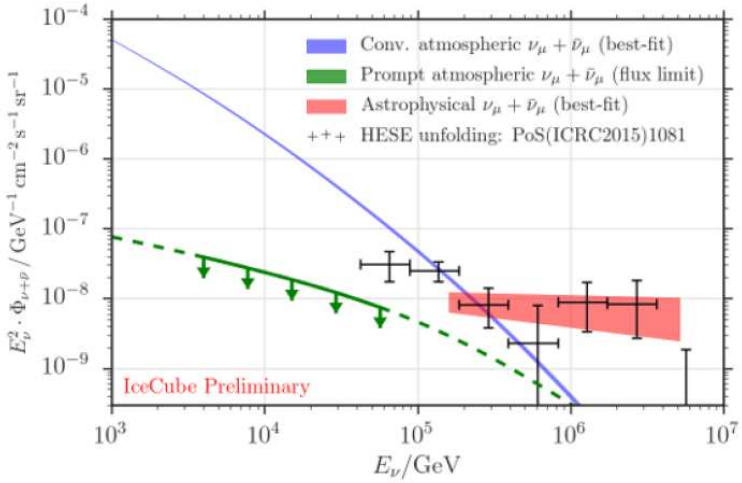

Figure 1.11: The measured IceCube neutrino flux [50].

Since more than 30 years, investments and efforts in accelerator neutrino physics have been focused on increasing the intensity of the neutrino beams (see Chapter 2). In the precision era of neutrino physics, efforts toward high intensity beams must be complemented by an ambitious programme of reduction of systematic uncertainties. Just after the discovery of θ_{13} (Section 1.4.2) it became clear that the physics reach of the two most ambitious facilities for the discovery of CP violation in neutrinos (DUNE in US and Hyper-Kamiokande in Japan) is put in jeopardy by the scarce data and limited precision of the experiments that measure neutrino interactions in matter [52]. Total and differential cross sections in the region of interest for DUNE and Hyper-Kamiokande (0.5-5 GeV) are still known with a precision of 10% or worse [53]. Theoretical models that describe the interactions of neutrinos show large discrepancies with data and uncertainties in the description of nuclear effects in

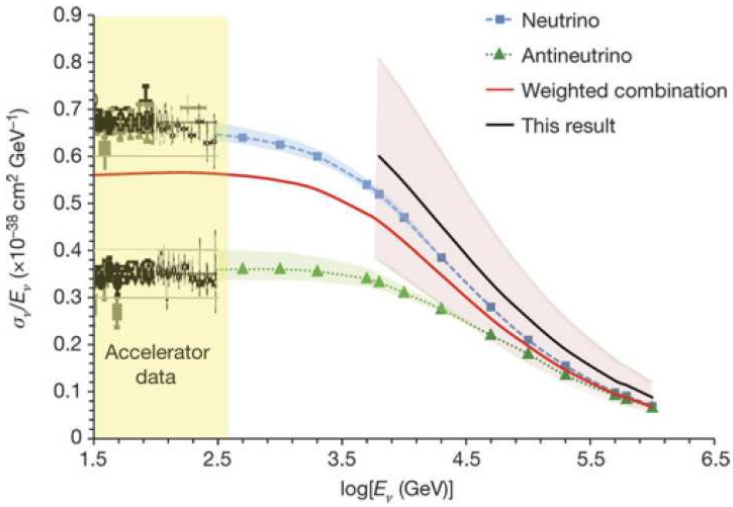

Figure 1.12: The neutrino cross section [50].

neutrino scattering play a leading role in the measurement of the oscillation parameters. A new generation of cross section experiments needs:

- Neutrino beams with a 1% precision in the knowledge of the flux at source since flux uncertainties are the leading systematic contributions to all cross section measurements at the few GeV scale;
- an intense and well controlled source of electron neutrinos since future oscillation experiments are mostly based on $\nu_\mu \rightarrow \nu_e$ oscillations and the ν_e cross section is measured directly with a precision worse than 20%;
- detectors capable of reconstructing with high precision the final state particles of ν_μ and ν_e charged current events to determine total and differential neutrino cross sections in liquid argon (of interest for DUNE) or water (of interest for HyperKamiokande).

A direct measurement of the ν cross sections is, hence, of great interest for the current (T2K, NOνA) and next (DUNE, HyperK) generations of oscillation experiments. These considerations motivated the development of "monitored neutrino beams" [54] and, in turn, the ENUBET proposal [57] for a facility where the only source of electron neutrino is the three body semileptonic decay of the kaons: $K^+ \rightarrow e^+ \pi^0 \nu_e$ (K_{e3}). In ENUBET, the electron neutrino flux is monitored directly via the observation of large-angle positrons in the decay tunnel. The ERC ENUBET ("Enhanced NeUtrino BEams from kaon Tagging") project intends to build a detector that identifies positrons in K_{e3} decays while operating in the harsh environment of a conventional neutrino beam decay tunnel. The project addresses all the accelerator challenges of monitored neutrino beams: the proton extraction scheme,

the focusing and transfer line, the instrumentation of the decay tunnel (this Thesis) and the assessment of the physics performance.
Figure 1.13 shows the impact of the ENUBET cross section measurement compared with the present measurement of the ν_e cross section.

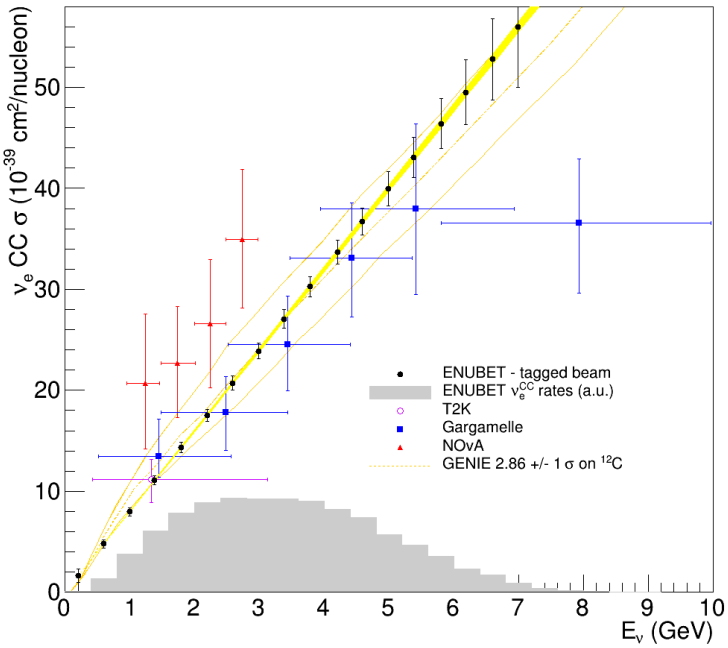

Figure 1.13: Expected precision on the ν_e cross section measurement of ENUBET (black dots) compared with present measurements (red and blue dots). The dotted red line is the current uncertainty on the theoretical calculations (GENIE neutrino generator) and the yellow area is the systematic error after ENUBET [57].

Chapter 2

Neutrino beams and the ENUBET project

Neutrinos, albeit difficult to detect, are very abundant particles in the Universe and may hold the answer to many unsolved physical and astrophysical questions. For example, the cosmic neutrino background is an echo of the Big Bang even older than the cosmic microwave background radiation; it has a number density of about 56 cm^{-3} and is made of neutrinos that decoupled from matter when the Universe was just one second old [58]. Another source of neutrinos is represented by the supernovae, in which neutrinos are likely to play a crucial role in the mechanism of the explosion [1]. These two sources, along with others like the Sun (which provides a remarkable ν_e flux to Earth of approximately 6×10^{10} $cm^{-2}s^{-1}$) and the secondary cosmic rays, are natural and "free of charge", but no control over them is possible.
To better study the neutrino properties controlled sources are needed, such as nuclear reactors and particle accelerators. The latter type of facility and in particular how neutrino beams are obtained is discussed in this chapter, starting from conventional neutrino beams to arrive to the ENUBET facility, which foresees an active decay tunnel for the direct measurement of the neutrino flux.

2.1 Conventional neutrino beams

In conventional neutrino beams a high-energy proton beam impinges upon a nuclear target, producing a beam of pion and kaon secondaries. The decays of the secondaries yield a ν_μ beam, with a ν_e contamination. This type of beam has already operated at Brookhaven, CERN, Fermilab, KEK, Los Alamos and Serpukhov, and new facilities at Fermilab, J-PARC and CERN are under development [59].

2.1.1 Accelerator Neutrino Beam Concept

The concept of an accelerator neutrino beam was conceived and proposed by both Schwartz [60] and Pontecorvo [61] independently. The experiment performed by Schwartz [62] in 1962 established the existence of the muon neutrino, and consequentely of two neutrino flavors. Their apparatus is shown in Fig. 2.1.

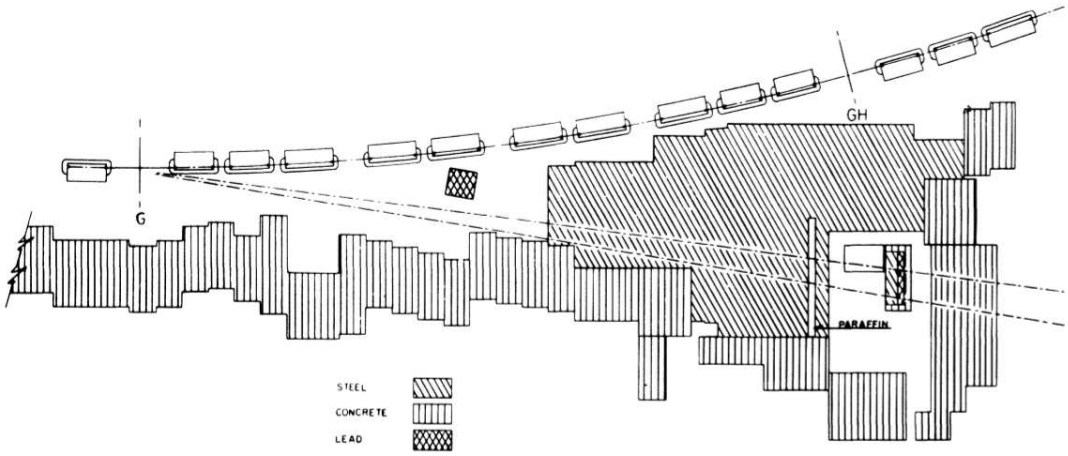

Figure 2.1: Plan view of the first accelerator neutrino experiment [62].

In this experiment, the pion and kaon secondaries left the target with a boost in the forward direction but with a beam divergence due to production cross sections:

$$d^2\sigma/dp_T dx_F \tag{2.1}$$

where p_T is the momentum of the secondary particle transverse to the proton beam axis and $x_F \approx p_L/p_{proton}$ is the ratio between the momentum of the secondary particle in the longitudinal direction with respect to the beam axis and the proton beam momentum. The secondaries drifted in free space for $\sim$21 m and decayed to neutrino tertiaries. A 13.5 m thick iron wall, often referred to as "beam stop" or "muon filter", shielded the experiment from all the particles apart from the neutrinos.

Muon neutrino beams are the most accessible to develop, because the production of ν_μ is favored in the decays of the secondaries ($\pi^\pm \to \mu\,\nu_\mu$ with a branching ratio (BR) $\sim$100%, $K^\pm \to \mu\,\nu_\mu$ BR=63.4% and $K_L \to \pi\,\mu\,\nu_\mu$ BR=27.2% [13]). Electron neutrino beams, on the other hand, are less straightforward to build; one hypothesis is to use the $\mu \to e\,\nu_e\,\nu_\mu$ decays, but the long muon lifetime makes this solution more complicated than exploitable. Another way is to produce ν_e beams from beam dump experiments, a technique already employed both for ν_e beams [63, 64] and ν_τ beams, from $D_s \to \tau\,\nu_\tau$ [65, 66]. In conventional neutrino beams, it is possible to infer the neutrino spectra from the secondary particles (π, K) spectra as they are related, along with the kinematics of their in flight decay.

In the experiment performed by Schwartz the proton beam was not extracted. The protons accelerated by the Alternating Gradient Synchrotron (AGS) at the Brookhaven National Laboratory (BNL) were deviated by a deflector in order to strike an internal Be target in a 3 m straight section of the accelerator. The secondaries exited the target with a 7.5° angle with respect to the proton direction [62].
The switch to neutrino experiments with dedicated extracted proton beams was first conceived at CERN [67, 68], for three main reasons:

- the extraction efficiency for a fast-extracted internal beam is nearly 100% [67], while for the internal target was about 70% according to [62] or 50% in [69];
- to better collect the pions leaving the target, the CERN team developed a lens system [70] that was too large to be located in or around the synchrotron;
- this lens system (van der Meer lens) is based on an electromagnet sourced by a pulsed current. It required short beam pulses (<1 msec) to avoid overheating from the pulsed current.

Given the rarity of neutrino interactions with matter, the more protons are delivered on the target of neutrino experiments, the better. The experiment performed by Schwartz in 1962 received 1.6×10^6 "pulses" with 1.9×10^{11} protons-per-pulse (ppp) on average [71]. In today experiments $10^{20} - 10^{21}$ protons are delivered onto the targets (protons-on-targets, POT). It is not just the number of primaries but also of the secondaries per proton that is important in neutrino experiments: it grows with the incident proton beam energy, so a good figure of merit is (POT $\times$ beam energy). Figure 2.2 shows the beam dose expressed as Joules per experiment, starting from the first accelerator neutrino experiment and ending with FNAL NuMI. The most recent and upcoming experiments, such as CNGS, J-PARC and NOνA are not shown, but are overall placed one order of magnitude above in accumulated dose.

2.1.2 Production of Hadrons in the Target

In a neutrino experiment the knowledge on the production of secondary particles (π^+, π^-, K^+, K^- and K_L) in the target is of utmost importance. The production yields ($d^2N/dpd\Omega$), as a function of both the momentum of the secondary particles and the exit angle from the target (Fig. 2.3), are useful to understand important features of the neutrino beam; the energy spectrum of the produced neutrinos is related to the momentum of the pions and kaons, while the secondary production angle is used to determine the direction of the neutrino beam or how well the secondary particles are captured by the focusing system.
Hadron production data are used to extrapolate models of secondary production, but the prediction of the neutrino flux starting from the production of secondaries is not an easy task

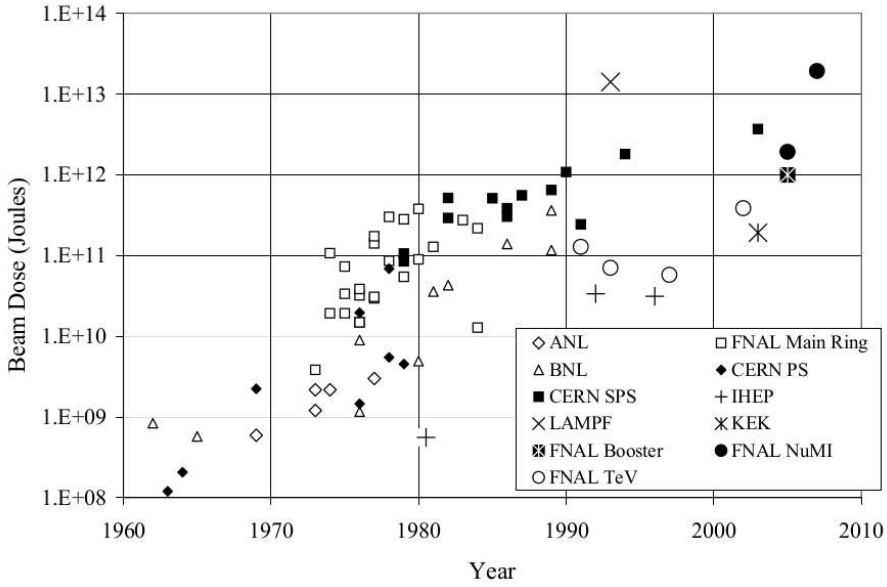

Figure 2.2: Beam dose expressed as total number of protons-on-target times the beam energy delivered in neutrino experiments at various laboratories, by date of publication. Experiments running concurrently in the same neutrino line are not plotted separately [59].

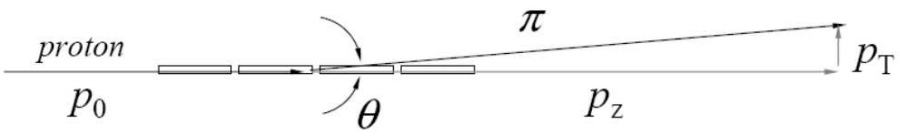

Figure 2.3: Pion secondary produced by a proton striking a segmented target: the momentum components are indicated [59].

and is one of the main sources of uncertainty. An example is given by the beam survey of the yield of secondaries performed by the Aragonne National Laboratory (ANL), in which the primary particles were 12.5 GeV/c protons impinging on thick targets of Al and Be [72]. The comparison with subsequent but more limited surveys [73, 74] reported a discrepancy on the neutrino flux of a factor 2 [75]. As suggested by Sanford and Wang [75], the results on $d^2N/dpd\Omega$ of the ANL experiment were scaled up in order to agree with the normalization of the newer experiments; this led to an extimation of a 30% error on the neutrino flux. The beam surveys were subsequentely re-performed [76], fixing the normalization problem and covering the full phase space [77], [78]; however, the authors of [77] had to defer the calculation of the ν flux to "a subsequent publication".
One of the aspects of hadron production predicted by Feynman [79] has been demonstrated with simulations with the Fluka-2005 [80] Monte Carlo code: the secondary pion momenta p_z scale with the primary proton beam momentum p_0 (quantities as defined in Fig. 2.3). Figure 2.4 shows the distributions of p_z and $x_F \approx p_z/p_0$ for π^+ produced by protons striking a graphite target. The x_F distributions are quite similar (Fig. 2.4 right), confirming the linear relation between p_z and p_0.

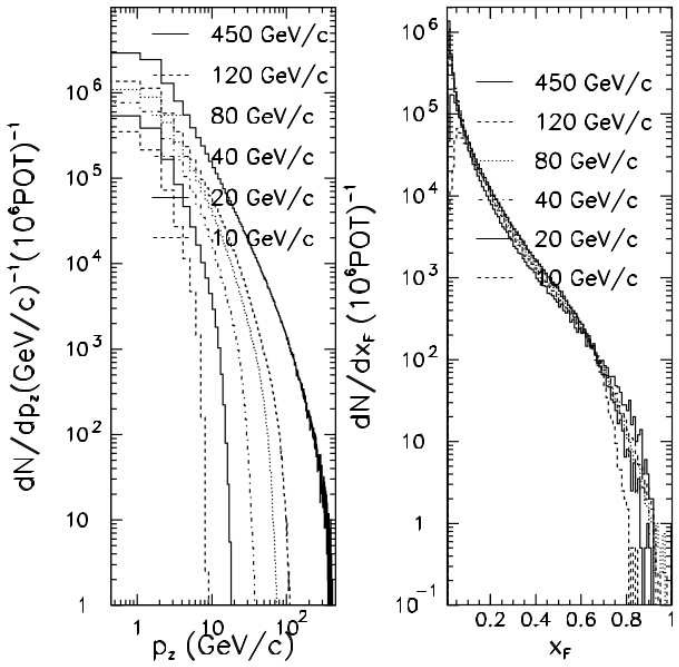

Figure 2.4: Fluka [80] calculations of (left) p_z and (right) x_F distributions of π^+ in p+C collisions at incident momenta of p_0 = 10, 20, 40, 80, 120, 450 GeV/c and p_z >0.5 GeV/c. A 94 cm long target, with a 6.4 $\times$ 15 mm^2 transverse size, is assumed. Taken from [81].

Another interesting feature is that the mean number of π^+, given by the integral of those curves, grows nearly linearly with p_0 as shown in Table 2.1.

p_0 (GeV/c)	$\langle n_\pi \rangle$	$\langle p_T \rangle$ (MeV/c)	K/π
10	0.68	389	0.061
20	1.29	379	0.078
40	2.19	372	0.087
80	3.50	370	0.091
120	4.60	369	0.093
450	10.8	368	0.098

Table 2.1: Fluka [80] predictions for π^+ production above p_z >0.5 GeV/c in a $6.4 \times 15 \times 94$ mm^3 graphite target per incident proton. $\langle n_\pi \rangle$ is the mean number of pions produced per incident proton, $\langle p_T \rangle$ is the mean transverse momentum for the pion, and K/π is the ratio of the corresponding yields for several incident proton momenta. In good approximation, $\langle n_\pi \rangle \propto (p_0)^{0.7}$.

On the other hand, the transverse pion momentum p_T should be independent of x_F, *i.e.*

$$d^2N/dp_T dx_F \approx f(x_F)g(p_T) \tag{2.2}$$

Fig. 2.5 shows that the shape of p_T does not scale much with different incident momenta p_0 or exiting pion momenta p_z.
This aspect is important because p_T controls the divergence of the secondary beam and consequentely the direction of the neutrino beam. Quantitatively, these scaling conclusions are correct, but when compared with the current experimental data discrepancies arise. The target geometries play a big role in the prediction of the neutrino spectrum [59]: secondary particles, especially in high energy proton beam experiments, have a probability of reinteraction in the target materials proportional to the pathlength travelled inside the target itself, resulting in tertiary hadron production. These interactions deplete the beam of high-energy particles and increase the yield of low-energy particles, as calculated with Fluka (Fig. 2.6).

2.1.3 Decay volumes

The decay volumes are the areas of the neutrino beam in which pions drift and decay. The length of the decay tube is set by taking into account the γ Lorentz factor of the particles, their mean lifetime, and the percentage of pions that is meant to decay. Considering a 5 GeV/c pion, $\gamma \approx 35$ and $\gamma\beta c\tau_\pi \approx 280$ m set the scale for the length of the decay tunnel if, for example, in a 2 GeV/c neutrino beam only 63% of the pions is expected to decay.
The radius of the decay pipe is also important [82], especially for low neutrino energy beams, as the pions may hit the decay volume walls before decaying due to the divergence of the beam.
Usually the decay tunnels are evacuated beampipes, because in air at atmospheric pressure

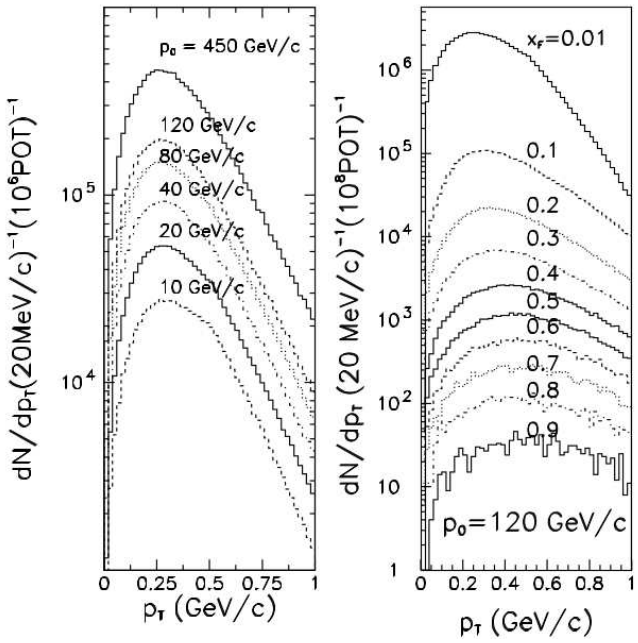

Figure 2.5: Fluka [80] calculations of (left) p_T spectra of π^+ produced in p+C collisions at several incident proton momenta p_0; (right) p_T spectra of π^+ produced in 120 GeV/c p+C collisions for several values of x_F. Taken from [81].

the same 280 m mean flight path corresponds to 0.9 X_0 (radiation length) [1] and 0.26 λ_{int}^{air} (nuclear interaction length) [2], meaning that a pion has a $\approx 26\%$ chance of being absorbed via a collision; if not absorbed, the pions will experience in any case multiple Coulomb scattering and typically deviate from their original path of 2.8 mrad. This angle is not negligible, especially if compared to the opening angle $1/\gamma \approx 14$ mrad between a muon and a 4 GeV/c neutrino given by the decay of a 10 GeV/c pion. If a decay tube is not evacuated, it is usually filled with He gas to reduce absorption and scattering, such as at KEK [84].
The muon filter stops the muons produced in the decay tunnel and prevents them to reach the neutrino detector. It also blocks the pions and kaons and its positioning defines the

[1] The radiation length X_0 is defined as:

$$X_0\ (\mathrm{g/cm^2}) \simeq \frac{716\ \mathrm{g\ cm^{-2}} A}{Z(Z+1)\ln(287/\sqrt{Z})} \tag{2.3}$$

in which Z and A are, respectively, the atomic number and the weight of the material. X_0 is linked to the rate at which the electrons, when interacting with a material, lose energy by bremsstrahlung. The average distance x that an electron needs to travel in a material to reduce its energy to $1/e$ of its original energy E_0 is [83]:

$$\langle E(x) \rangle = E_0 e^{\frac{x}{X_0}} \tag{2.4}$$

[2] The nuclear interaction length is the mean free path travelled by a hadronic particle in a given material [83].

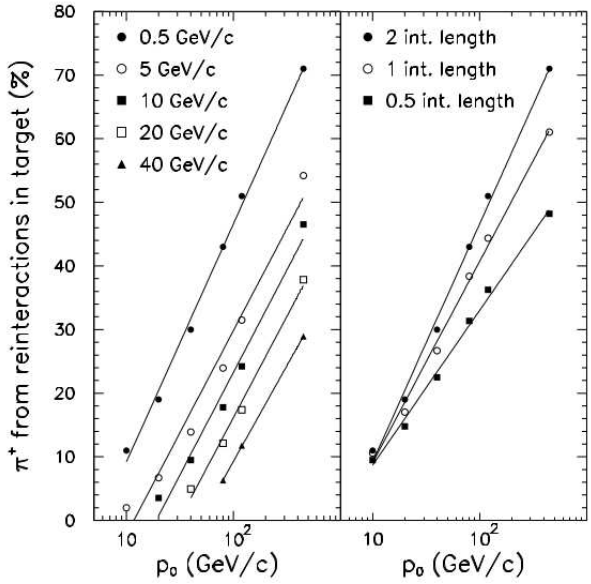

Figure 2.6: Fluka [80] calculations of the fraction of tertiary π^+ production from reinteractions in a graphite target of 6.4×15 mm^2 in transverse size as a function of the primary beam momentum p_0. (left) The reinteraction fraction is plotted for a 2.0 interaction length target for π^+ with p_z >0.5, 5.0, etc. GeV/c momentum threshold. (right) The reinteraction fraction is plotted for targets of 0.5, 1.0 and 2.0 interaction lengths. Taken from [81].

percentage of the mentioned particles that is allowed to decay. To give a few examples, the CERN PS neutrino beam had a 80 m decay volume [85], in which 25% of pions and 90% of kaons at 5 GeV/c could decay, while for NuMI [86] the percentages are 73% and 100% for $\sim$ 10 GeV/c pions and kaons respectively in a 725 m decay tunnel. The positioning of the muon filter is also dictated by cost-effectiveness, because building a decay tube long enough to allow most focused pions to decay is expensive. The size of the ν_e contamination depends on the decay tunnel length too, as much of it arises from $\pi \to \mu\,\nu_\mu \to (e\,\nu_\mu\,\nu_e)\nu_\mu$.

2.1.4 Flux monitoring

In a traditional neutrino beam, three particle fluxes are monitored: the flux of the primary particles (protons), of the secondary ones (pions and kaons), and of tertiary muons.
As far as the primary particles are concerned, for a neutrino experiment it is enough to monitor the proton beam just upstream of the target. The important parameters are: the total intensity of the beam striking the target, its position, divergence, entry angle and spot size. There are several methods to measure the proton flux on target, for example foil activation techniques, in which Au [87], Al [88], or polyethylene [89] foils are placed upstream of the target and their residual activity is measured. Segmented ionization chambers [84, 90–92], Aluminum Scanning Electron Microscopes (SEMs) [93], W wire SEMs [94], ZnS screens

[87, 88, 95] have been used to measure the proton beam profile.
The monitoring of the flux of the secondary (π, K) beam of a wide-band beam is quite unusual, because the instrumentation placed directly in the beam has to sustain high rates and there is the risk of affecting the neutrino flux. However, some examples do exist. For the CERN-PS neutrino beam, in 1967, the possibility to place a spectrometer and a Cherenkov counter system to measure π/K fluxes was taken into account. The system was meant to be placed downstream of their horns [96]. This measurement was destructive for the neutrino experiment, but it would have given an analysis of hadron production and focusing. When this system was tested [97], the δ-rays background present in the beam and produced in the spectrometer turned out to be a serious issue.
Ion beam chamber arrays placed in the secondary beam were used as beam quality monitors in the Fermilab NuMI experiment [98]. The NuMI chambers had to stand a rate of $\sim 2 \times 10^9$ particles/cm^2/spill and were exposed to a $\sim$ 2 GRad/yr dose. The huge fluxes of photons, electrons, positrons and neutrons prevented to use the chambers for a flux measurement. The detectors were placed right upstream of the beam absorber; the flux in that area was dominated by unreacted protons crossing the target and chambers were used to monitor the proton beam as well as to check the integrity of the target.
As far as the muon beam monitoring is concerned, there are two kinds of systems: flux measuring systems and diagnostic systems [59]. Monitoring the flux of tertiary muons is a way to have a measurement of the neutrino flux, since they both come from the same decay. However, this solution is not always feasible for all beamline geometries, either because of decay kinematics or the shielding, as it limits the fraction of muon flux visible to muon detectors. The first issue is that the muon detectors have to be placed downstream the muon filter: the result is that only muons above a given energy threshold get to the detectors, giving a partial measurement of the neutrino energy spectrum, as the lowest part is cut off. The second issue is the solid acceptance of the muon detectors, that can be really small and this is a problem especially at lower energies, where the products of pion decays are emitted at wider angles and may not intercept the muon detectors at the end of the volume.
The diagnostic systems can be similar to flux measuring systems, but have access to a smaller fraction of the muon spectrum. They operate during neutrino running and the radiation tolerance is a feature to be taken into account.
In the second neutrino experiment at BNL [99] the muon flux was measured, making it the first attempt to measure a neutrino flux using tertiary muons. The measurement was performed by placing emulsions in seven "probe holes" in the steel shielding at the end of the decay region. In each hole, four different emulsions were placed at different transverse distances from the beam axis. The error on the flux from these measurements was 20-30%, due also to the energy threshold. The obtained flux data are shown in Fig. 2.7.
As a follow up of these experiments, at CERN the neutrino spectrum was estimated using muon system measurements [101]. There were several challenges, including the fact that

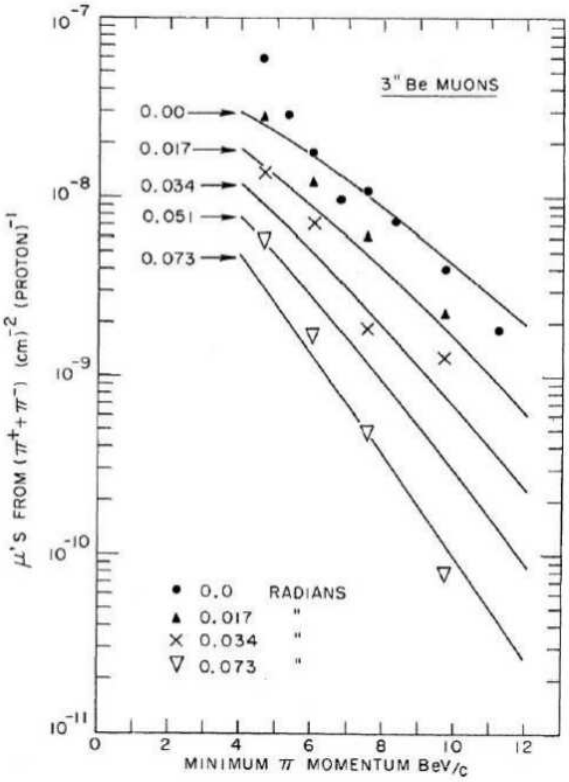

Figure 2.7: Emulsion measurements of muon fluxes in the steel shielding in the BNL neutrino experiment [99]. The points are fitted using the CKP model [100].

muons from K decays can be distinguished from those from π decays only at large lateral offsets from the beam axis, so the π/K ratio needs to be assumed from external "beam survey" data.

Muon monitoring employs different technologies, such as ionization chambers [84, 88, 101–104], solid state muon detectors [105–107], and plastic scintillator [75, 90, 101].

In addition to the uncertainty on the fraction of muons from K decay, conventional neutrino beams are also polluted by a small fraction of ν_e from kaon and muon decays [54]. The size of this contamination depends on three main factors: the energy of the primary proton beam, the momentum of the selected secondaries and the length of the decay tunnel. The origin of the ν_e contamination is linked to the energy of the neutrino beam; for high energy neutrino beams, like the CNGS one [108], the contamination arises from the K_{e3} ($K^+ \to e^+\nu_e\pi^0$) decays of the K^+, while in lower energy beams it is mostly due to the $\pi^+ \to \mu^+\nu^\mu \to e^+\nu_e\overline{\nu}_\mu\nu_\mu$ decays. The uncertainty on the size of this contamination, even with dedicated hadro-production data, pion monitoring at the target and muon monitoring at the beam dump, has never been reduced below $\sim 10\%$ [54].

2.2 ENUBET: a neutrino beam with a monitored decay region

The uncertainty on the fluxes in conventional neutrino beams limits the knowledge of the neutrino cross sections, as the rate of ν_μ is not directly monitored [54]. For this reason, the sensitivity on the absolute neutrino cross section is bound to $O(5-10\%)$ [109–111]. Moreover, the next generation oscillation experiments, both long-baseline [112–116] and dedicated [117–119] ones, will rely on the appearance of ν_e at the far detector, requiring a direct measurement of the ν_e cross sections. Further knowledge of ν_e interactions in the range of interest (0.5-4 GeV) will also be of use for future long-baseline neutrino experiments [54]. The ν_e cross section could be extrapolated from the ν_μs produced in pion decay-based beams, but additional uncertainties may be introduced [120]. Muon-based beams could be an answer to improve cross section measurements, but π/K based beams can still be exploited to improve flux systematics [121].
The Enhanced NeUtrino BEams from kaon Tagging project (ENUBET) (ERC-Consolidator Grant-2015, n° 681647 (PE2)) [54] follows the second option. The idea behind ENUBET is to aim for a pure and well controlled source of electron neutrinos and to monitor the neutrino flux directly inside the decay region by exploiting the three body decay of the K^+, the K_{e3}:

$$K_{e3} : K^+ \rightarrow \pi^0 \, e^+ \, \nu_e \tag{2.5}$$

By monitoring the positron flux with calorimetric techniques, it is possible to directly estimate the electron neutrino flux inside the decay tunnel. This observable is then directly linked to the rate of the ν_e at the far detector. The ENUBET project involves both the development of the beamline, which will collect and focus the K^+, and of the positron tagger (Fig. 2.8).

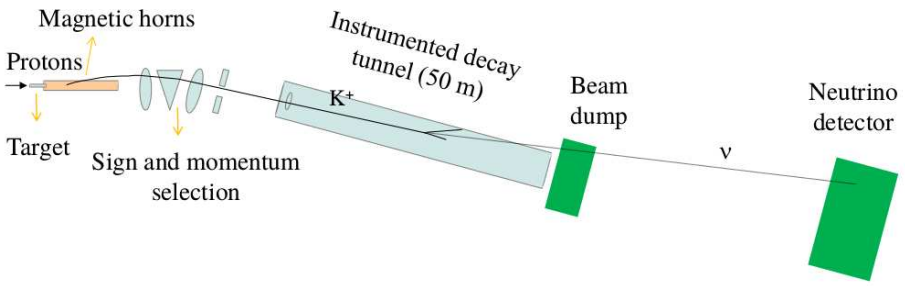

Figure 2.8: Layout of the facility (not to scale).

2.2.1 The beamline

The beamline is designed to enhance the ν_e components from K_{e3} and to heavily suppress the ν_e contaminations from muon decays. Starting from a conventional neutrino beam, it is possible to build a beamline dominated by the K_{e3} contamination, which becomes no longer a contamination but the wanted decay. By increasing the energy of the selected secondaries and by reducing the length of the decay tunnel, it is possible to enhance the ratio between the ν_e from K_{e3} and the ν_μ from pion decay (Fig. 2.9-black lines).

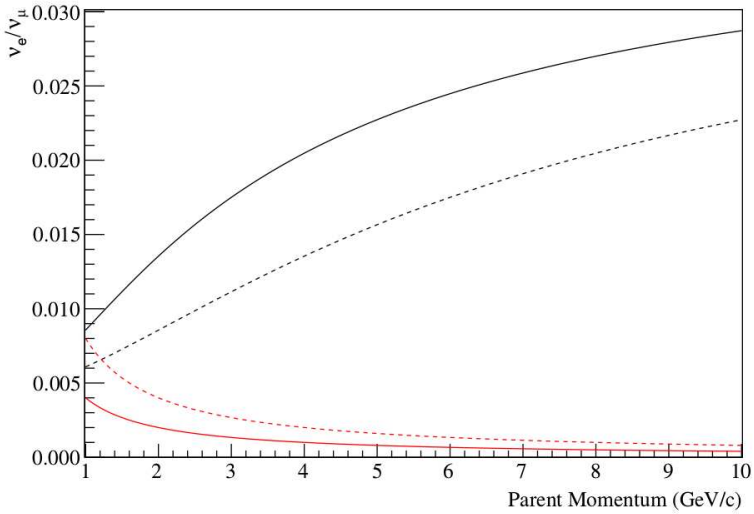

Figure 2.9: Black lines: approximate scaling of the ν_e/ν_μ fluxes as a function of the momentum of secondary particles. The continuous line corresponds to a 50 m decay tunnel, the dashed line to a 100 m tunnel. The red lines show the scaling of the ν_e/ν_μ from muon in flight decay (DIF).

This allows also to reduce the ν_e beam contamination from muon in flight decays (DIF) (Fig. 2.9-red lines) and makes the overall neutrino flux smaller. The ν_e/ν_μ ratio scales as:

$$R_{K/\pi} \cdot BR(K_{e3}) \cdot \frac{[1 - e^{-L/\gamma_K c\tau_K}]}{[1 - e^{-L/\gamma_\pi c\tau_\pi}]} \tag{2.6}$$

where:

- $R_{K/\pi}$ is the ratio between the K^+ and π^+ secondary particles, produced at the target;
- $BR(K_{e3})$ is the K_{e3} branching ratio, which amounts to $5.07 \pm 0.04\%$ [13];
- L is the decay tunnel length;
- τ_K and τ_π are the lifetimes of the K^+ and the π^+ respectively;
- γ_K and γ_π are the Lorentz factors of the K^+ and π^+.

Figure 2.9 shows the scaling of Eq. 2.6, assuming $R_{K/\pi} = 10\%$. In this beam the K_{e3} decays are the only source of positrons, along with the Dalitz from the $\pi_0 \to e^+e^-\gamma$ decay (BR $\simeq 1.2\%$).
The ENUBET beamline is based on conventional technology: the primary particles are protons impinging on a target and the produced secondaries are captured and sign selected down to the instrumented decay tunnel. The optimal average value for the secondary beam is 8.5 GeV/c, with a momentum bite of $\pm 20\%$. This is the optimal value, as smaller values decrease the π^+/e^+ separation efficiencies, and higher values bring the ν_e energies outside the region of interest (0.5-10 GeV). The local particle rates should be kept below $O(1)$ MHz/cm^2, in order to safely operate the tagger (in terms of pile-up, dose, etc.). For this reason, fast proton extractions (10 μs) would lead to a local rate challenging for the positron tagger, and hence must be kept above 1 ms. On the other hand, extractions longer than 10 ms are not ideal for the magnetic horns that perform the focusing, as they lead to an increase of the Joule heating [54]. The optimal choice for the extraction length is 2 ms, similar to the one employed at the CERN West Area Neutrino Facility (WANF [122]).

2.2.2 The decay tunnel

The decay tunnel itself is the detector that measures the positron rate (Fig. 2.10). It is a hollow, cylindrical calorimeter of 50 m length, built around an evacuated beampipe. The minimum possible inner radius for the tunnel is set at R_{in} = 40 cm, which results in a line of sight of 8 mrad between the entrance of the tunnel and the beam dump; this ensures that all the undecayed particles (π^+, K^+, p) and all the muons from the 2-body decay of the π^+ will reach the beam dump without crossing the calorimeter. Given R_{in}, the minimum outer radius is R_{out} = 57 cm: this thickness of the calorimeter ensures the confinement of almost all the particles originating from kaon decays.

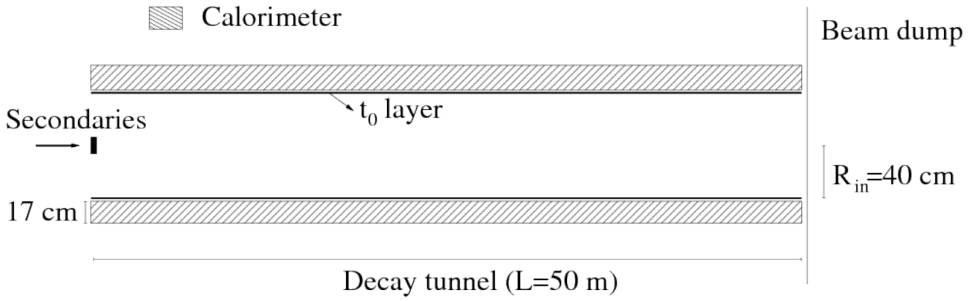

Figure 2.10: The instrumented decay tunnel (not to scale). The black rectangle on the left indicates the entrance window of the secondary particles in the transverse plane ($\pm$5 cm) [54].

In the decay tunnel, the mean positron emission angle is 88 mrad (Fig. 2.11), $\sim$20 times the emission angle for the μ^+ and $\sim$30 times the beam divergence.

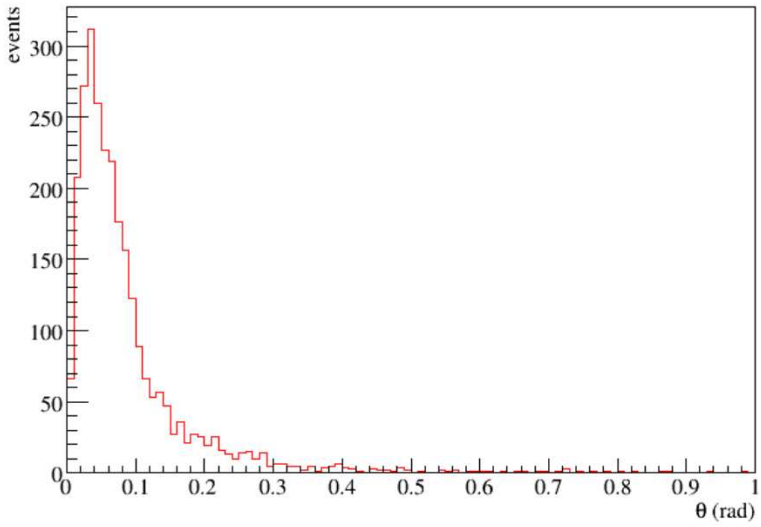

Figure 2.11: Polar angle distribution of positrons for 10^5 K^+. Small angle positrons, i.e. e^+ reaching the beam dump without crossing the calorimeter, are included [54].

The identification of the positrons is performed by the calorimeter built around the evacuated beampipe, by mapping the longitudinal shower development inside the detector. A "t_0 layer" acts as a pre-shower and is used to reject the photons; it also provides the time of arrival of the charged particles and vetoes neutral particles in the calorimeter.

2.2.3 Background and particle ID

The decay interesting for ENUBET, the K_{e3}, amounts only to $\sim 5\%$ of all the K^+ decays. The majority of the particles that cross the calorimeter are muons from the $K_{\mu 2}$ decays, $K^+ \to \mu^+ \nu_\mu$, BR $\sim 63\%$, and pions from the decay $K^+ \to \pi^+ \pi^0$, BR $\sim 21\%$ [13]. In order to assess the misidentification probability, a first simulation with GEANT4 [123, 124] was run, which comprehended the simulation of particle decays in the tunnel, the crossing of the t_0 layer and the calorimeter response to both charged and neutral particles. The calorimeter was simulated as a homogenous copper cylinder, with a radiation length of 1.44 cm, a nuclear interaction length of 15.3 cm and a Molière radius of 1.568 cm. In this simulation, the variables used for pion/positron separation were $R_1 \equiv E_1/E_{tot}$ and $R_2 \equiv E_2/E_{tot}$, in which E_{tot} is the energy in the whole calorimeter, E_1 is the energy sampled after 5 X_0 and E_2 is the energy sampled after 10 X_0 (see Chapter 3), both inside a cilinder of radius $2R_M$, to avoid uncertainties due to lateral leakage.
In this simulation, to identify a positron, the candidate particle was required to deposit an energy $E_{tot} \geq 300$ MeV inside the calorimeter and to produce an associated hit in the t_0 layer. An additional constraint was put on E_1 and E_2 requiring them to be larger than the one for a minimum ionizing particle, namely $R_1 > 0.2$ and $R_2 > 0.7$ (Fig. 2.12). With these

requirements, positrons from K_{e3} decays are selected with an efficiency of 69%.

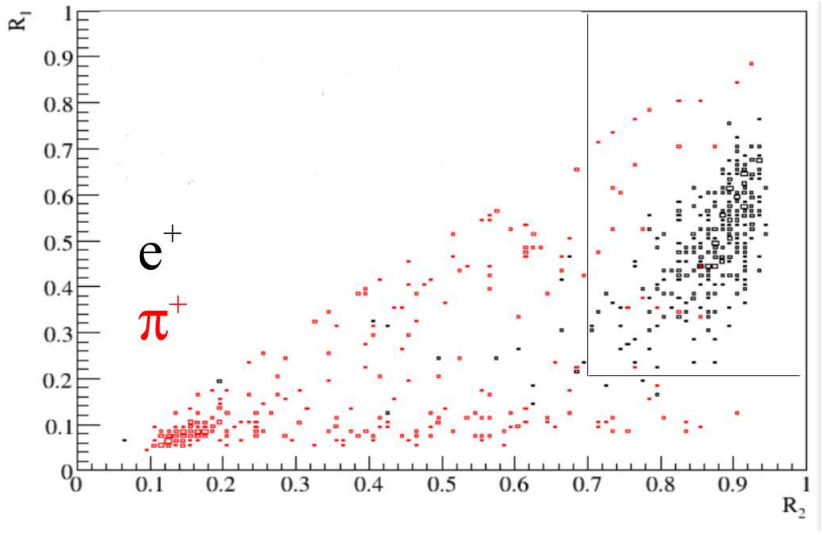

Figure 2.12: The energy deposit at R_1 versus the energy deposit at R_2. The e^+ events are indicated in black, while the π^+ ones are in red [125].

2.2.3.1 Muon/positron separation

In the simulation, the muon/positron separation was achieved with the calorimeter with excellent results. MIPs, such as muons and punch-through pions, cluster at small values of R_1 and R_2 and the misidentification rate is smaller than 10^{-3} (integrated on all muons produced by $K_{\mu 2}$, $K_{\mu 3}$ and the DIF of pions from the other decay modes). Hence backgound from muon misidentification is not an issue.

2.2.3.2 Pion/positron separararation

π^+ dominate the background as π^+/e^+ separation is less efficient. Pions cluster at small values of $R_{1,2}$, but the hadronic shower has an electromagnetic component that can mimic the shower generated by a positron, especially at low energies. The major source of background is the $K^+ \to \pi^+\pi^0$ ($K_{\pi 2}$) with BR $\sim 21\%$, as its contamination of the positron signal with misidentified pions amounts to 13%. The simulation included the overlaps between photons from π^0 decays and Dalitz π^0 decays, but they give negligible contributions. The misidentification probability $\varepsilon_{\pi^+ \to e^+}$ is 2.2%.
Another significant source of background is the $K^+ \to \pi^+\pi^+\pi^-$ decay mode, with BR $=$ 5.6%. Even if the BR is smaller than the one of $K_{\pi 2}$, the misidentification probability is larger due to the higher charge multiplicity (3.8%); the positron energy distribution is shown

in Fig. 2.13 along with the energy distribution of the π^+ background from the $K^+ \to \pi^+\pi^0$ decay.

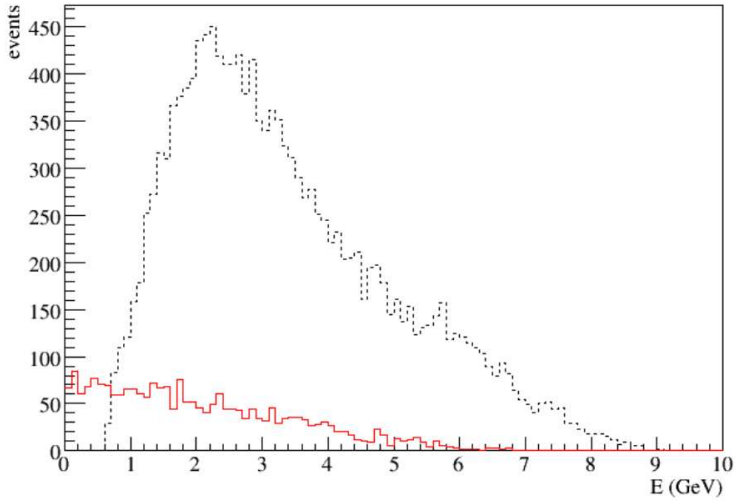

Figure 2.13: Red continuous line: energy distribution of positrons. Black dashed line: energy distribution of pions from the $K^+ \to \pi^+\pi^0$ decay. These events are from kaon decays hitting the calorimeter for 10^5 K^+ at the entrance of the decay tunnel [54].

2.2.3.3 Gamma/positron separation

Photons produced in the decay tunnel, from decays such as $K^+ \to \pi^+\pi^0$, will not give a hit in the t_0 layer associated with an energy deposit in the calorimeter, and won't be misidentified as positrons. On the other hand, if there is material at inner radii with respect to the t_0 layer, such as the beampipe, and photons convert by interacting with it, they constitute a source of background, because the ENUBET positron tagger does not exploit the time correlation among particles (π^+ and γs in this case). To give a few examples, if the beampipe is 1.5 mm thick and made of Be [126], the conversion rate is 3×10^{-3} and the contamination is less than 2%. If the material of the beampipe is 1 mm Al then the contamination grows to 6%. In this configuration, if the t_0 layer has a time resolution of $O(100)$ ps the background can be suppressed to a negligible level vetoing pions that originate in the same area of the candidate positron. Installing the t_0 inside the beampipe results in a negligible photon background; this configuration has been employed for the Large Angle Calorimeters of NA62 [127]. The basic unit for the t_0 layer is a doublet of plastic scintillator tiles with a dimension of 3×3 cm^2 and a thickness of 0.5 cm. Each tile is readout by a WLS fiber [124, 128] optically linked to a SiPM (Fig. 2.14).
Table 2.2 summarizes all the sources of background and the related misidentification probability.

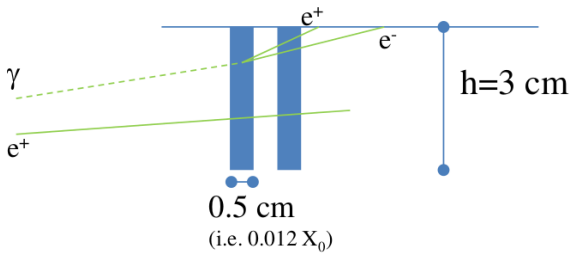

Figure 2.14: Scheme of the t_0 layer.

Source	BR	Misid	$\varepsilon_{X\to e^+}$	Contamination
$\pi^+ \to \mu^+\nu_\mu$	100%	$\mu \to e$ misid.	$< 0.1\%$	neglig. (outside acceptance)
$\mu^+ \to e^+\bar{\nu}_\mu\nu_\mu$	DIF	genuine e^+	$< 0.1\%$	neglig. (outside acceptance)
$K^+ \to \mu^+\nu_\mu$	63.5%	$\mu \to e$ misid.	$< 0.1\%$	negligible
$K^+ \to \pi^+\pi^0$	20.7%	$\pi \to e$ misid.	2.2%	13%
$K^+ \to \pi^+\pi^+\pi^0$	5.6%	$\pi \to e$ misid.	3.8%	5%
$K^+ \to \pi^0\mu^+\nu_\mu$	3.3%	$\mu \to e$ misid.	$< 0.1\%$	negligible
$K^+ \to \pi^+\pi^0\pi^0$	1.7%	$\pi \to e$ misid.	0.5%	negligible

Table 2.2: Sources of background and misidentification probability [54].

2.2.4 Rates expected in the tagger

A simulation of the tagger with a 2 ms extraction length and 10^{10} π^+ per spill showed that the maximum positron rate is 10 kHz/cm^2, dominated by the μ^+ generated from the $K_{\mu 2}$ decay ($K^+ \to \mu^+\nu_\mu$, BR $= 63.44 \pm 0.11\%$). The peak rate is 500 kHz/cm^2, corresponding to a rate of 5 MHz per channel if the calorimeter has a granularity of 10 cm^2. The simulated beam has a 3 mrad beam divergence that, along with the Lorentz boost of the decayed particles, results in low rates in the first 10 m of the tunnel and saturation from 10 to 50 m. This is shown in Fig. 2.15, where the number of particles is expressed in Hz/cm^2, the z indicates the length of the tunnel and each bin corresponds to a surface of $2\pi R_{in}\Delta z = 1.26$ m^2 [54].

2.3 The full simulation of the ENUBET beamline

The full simulation of the ENUBET beamline, from the first ENUBET proposal [54], has grown considerably during the years and is still under development. Most notably, the beamline was not simulated in detail and the detector response was simply obtained by

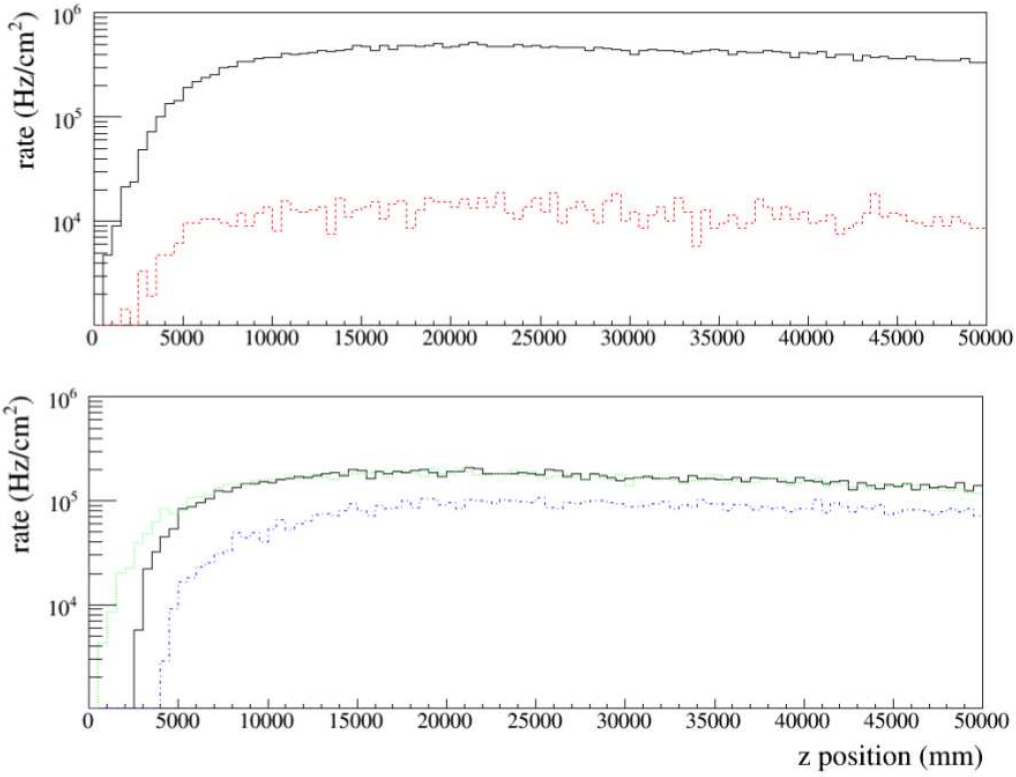

Figure 2.15: (top) The black continuous (red dashed) line shows the overall particle (positron) rates in the calorimeter as a function of the z position along the instrumented tunnel. (bottom) Muon (black continuous), photon (green dotted) and pion (blue dot-dashed line) rates in the calorimeter as a function of the z position. Rates are computed for a 2 ms extraction length and 10^{10} π^+ per spill [54].

the smearing of the energy deposit and taking into account the nominal resolution of the detectors. Recent simulations allowed to study the whole facility, using different softwares for different features and parts:

- FLUKA was employed to study the secondary particles (π and K) production from the interaction of the primary protons with targets of 1 m Berillium or graphite and also to compute the radiation dose on the detectors;
- the simulation of the components of the beamline was performed with TRANSPORT and G4BEAMLINE;
- GEANT4 was used to test the reconstruction algorithms and to simulate the particles in the decay tunnel.

This optimized simulation allowed to tune the instrumented decay tunnel parameters, such as the sampling term and the granularity (Chapter 3).
The hypothesized proton drivers for the ENUBET experiment are CERN, that allows proton energies up to $\sim$ 400 GeV, FNAL (120 GeV), and J-PARC (30 GeV). Figure 2.16 presents one of the two proposed focusing systems, the static one, in which a quadrupole triplet is placed before the bending magnet. The second option, not depicted, features a horn with a 2 ms pulse, 180 kA and 10 Hz during the flat top. The optimized dimensions for the decay tunnel are 1 m internal radius and 40 m length, with a low power hadron dump placed at the end; the proton dump position and size are still under optimization [55].

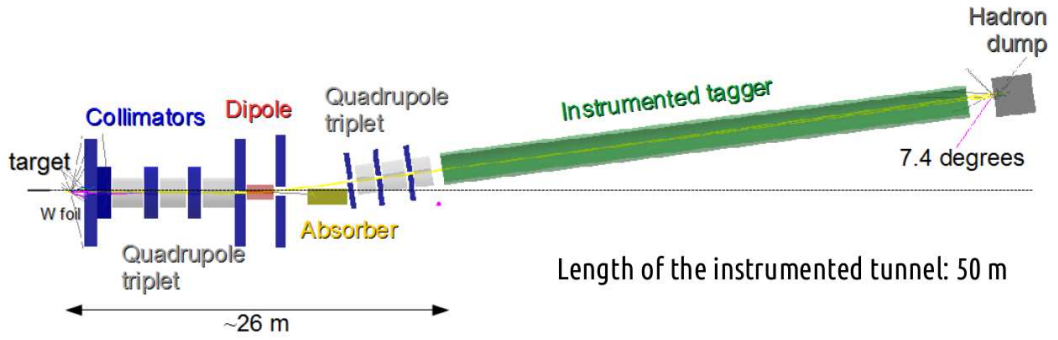

Figure 2.16: The ENUBET facility as designed in January 2019, with the static focusing system [55].

The particle reconstruction simulation was performed again considering a more definite detector structure, including a t_0 layer made of a doublet of plastic scintillator tiles (Chapter 3) for the electron/π_0 separation and 8 calorimeter layers (E0 to E7) [56]. The innermost layers, E0 and E1, are electromagnetic calorimeters, while the layers from E2 to E7 act as an energy tail catcher and the transverse section is divided in 76 cells. The event is selected in the following way:

- the cell of the E0 layer with the shortest registered time is taken as starting point;
- time-correlated cells are then considered, with the following constraint on Δt: [-2, 2] ns for the t_0 layer and E0, [-2, 3] ns for E1 and [-2, 15] ns for E2 to E7;
- an angular selection is also performed considering a region of ± 33 degrees.

After selecting the event, the particle identification is performed in two steps: first a e^+/π^+ separation based on a Neural Network, then a rejection of π_0s based on sequential cuts.

2.3.1 Neural Network for the e^+/π^+ separation

The variables used by the Neural Network are the following:

- maxfracE0, the energy of the most energetic cell in E0 divided by the total energy in all the layers (t_0 excluded);
- EL0, the energy of all the cells in E0 divided by the total energy in all the layers (t_0 excluded);
- EL1, the energy of all the cells in E1 divided by the total energy in all the layers (t_0 excluded);
- ERM, the energy of all the cells in a range of ± 1 with respect to the initial cell (for all the layers apart from t_0) divided by the total energy in all the layers (t_0 excluded). This corresponds roughly to the energy in the Molière radius.

Figure 2.17-left shows the correlation between the used variables, while Fig. 2.17-right presents the output of the Neural Network.
A cut at 0.6 (Fig. 2.18) results in a signal efficiency of 75% and a 5% background contamination. This value was chosen to keep the background at a level of 3% (a further decrease is achieved with π_0 rejection) and an energy cut of at least 15 MeV was also applied.

2.3.2 e^+/π^0 discrimination

This discrimination is perfomed mostly by the t_0 layer. Starting from the reference E0 cell, t_0 cells in the good time interval of [-2, 2] ns are selected. The first upstream t_0 doublet along the beamline is used as a starting point. The requirements for the t_0 layers are an energy deposit in the [0.65, 1.7] MeV range in each layer for the first 3 layers, and a number of missed t_0 doublets from the first to the E0 cell of 1 at maximum.

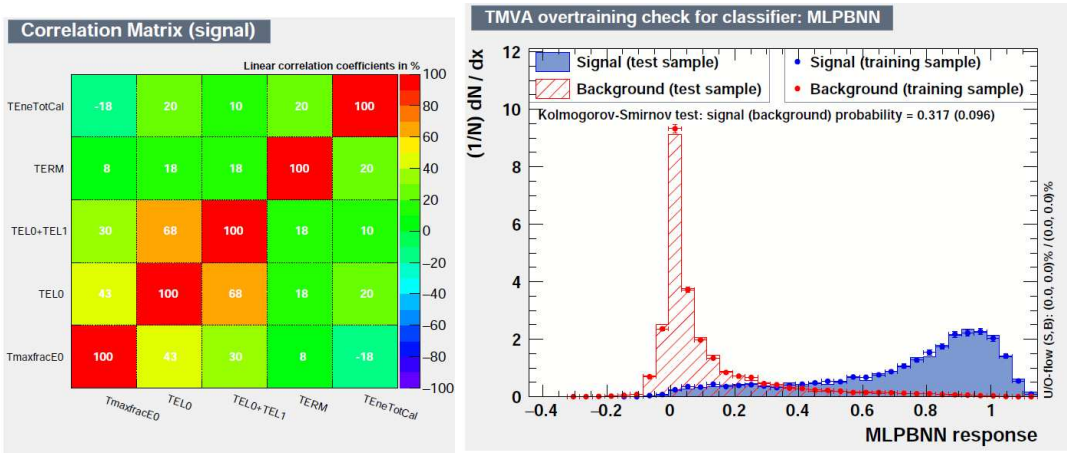

Figure 2.17: (left) Signal correlation matrix for Neural Network variables. (right) Output of the Neural Network [56].

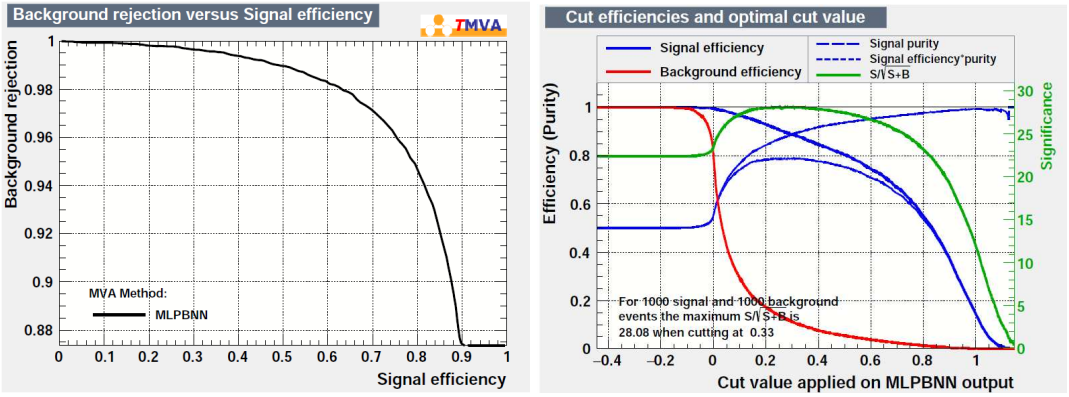

Figure 2.18: (left) Background rejection vs signal efficiency. (right) Efficiency as a function of the Neural Network cut [56].

Chapter 3

The ENUBET calorimeter and the feasibility test

In the ENUBET experiment, the separation of the electron signal from the charged pion background is performed in the decay tunnel. The two particles have a different shower development, so it is possible to identify positrons at the few-GeV energy scale with longitudinally segmented fast calorimeters. The technology of choice to instrument the decay tunnel is that of sampling calorimeters with plastic scintillators: it responds to the requirement of fastness (recovery time $\sim$ 10 ns) and it is cost-effective [129]. Moreover, it is relatively easy to segment sampling calorimeters both longitudinally and laterally, allowing for good space resolution and particle identification [83]. Shashlik calorimeters [130] are sampling calorimeters in which the tiles of absorbing and scintillating materials are perpendicularly crossed by the WaveLength Shifting (WLS) fibers used for the light collection and readout (Fig. 3.1).
They are characterized by ease of assembly and flexibility in terms of energy resolution, which is possible to tune by choosing the proper scintillator/absorber tile thickness and fiber frequency. A drawback on the use of shashlik technology for the ENUBET calorimeter is the way the fibers are bundled together and coupled with a photocathode at the end of the calorimeter [132], as it severely limits the possibility to longitudinally segment the detector. The proposed solution is to replace the conventional PhotoMultiplier Tube-based light readout with a more compact one based on Silicon PhotoMultipliers (SiPMs), embedded in the calorimeter structure [54], [129]. The SiPMs present themselves as a matrix of small, passively-quenched silicon avalanche photodiodes. They operate in Geiger mode and are read in parallel from a common output node. Each pixel has a digital response when hit by a photon (the produced current is the same for all pixels), but the whole SiPM provides an "analogical" information of the light that it detects, as the total output signal is proportional to the number of hit pixels (if operated below saturation conditions) [133], [134]. From the innermost to the outermost radius, the ENUBET decay tunnel is instrumented as follows:

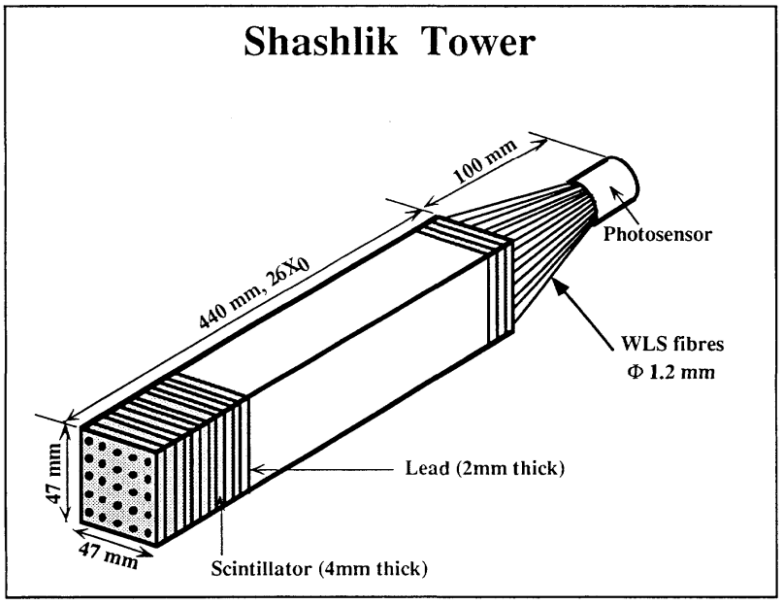

Figure 3.1: Mechanical design of a CMS Shashlik calorimeter prototype tower equipped with 25 aluminized WLS fibers [131].

- a t_0-layer for photon detection and rejection (Section 2.2.3.3);
- an electromagnetic calorimeter readout every $\sim 4\ X_0$;
- an energy tail catcher, or hadronic calorimeter, with a coarser granularity ($\sim 24 - 28\ X_0$).

A section of the tunnel is outlined in Fig. 3.2.
The electromagnetic calorimeter is built starting from a basic unit, the Ultra Compact Module (UCM), a small shashlik calorimeter that covers 4.3 X_0. In the considered energy range, the electromagnetic showers initiated by positrons are fully contained inside ~ 2 UCMs, while pion-induced ones are more extended, well into the energy tail catcher (Fig. 3.3).
The particle rate expected on the tagger is ≤ 500 kHz/cm^2, with non-zero probability of pileup. The rate plus the need to acquire the signal in triggerless mode require to use waveform digitizers and to extend the sampling of the whole waveform for ~ 2 ms. The final prototype that the ENUBET Collaboration is required to build is a 3 m $\times$ π calorimeter with an energy resolution of $\leq 20\%/\sqrt{E}$. Different materials have been characterized, in order to assess the technology, find solutions to ease the construction and improve the performances. This chapter gives a description of the UCM technology as well as a recap of the feasibility tests performed in August 2015, which validated the choice of this technique for the ENUBET goals.

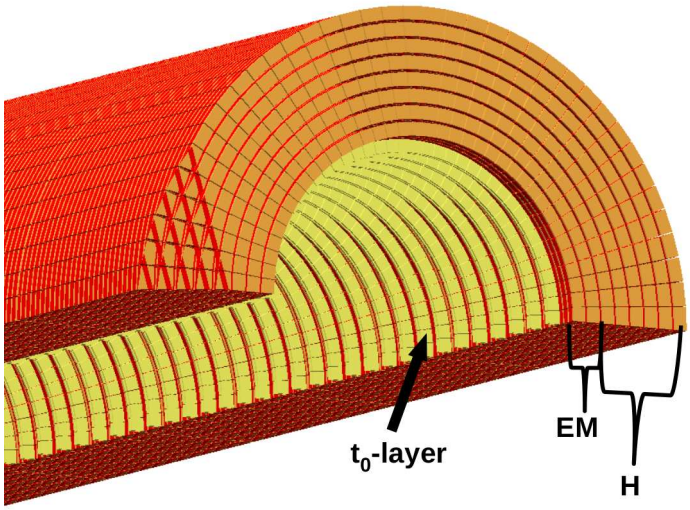

Figure 3.2: Decay tunnel outline. The electromagnetic (EM) calorimeter is surmounted by the energy tail catcher or "hadronic" calorimeter (H).

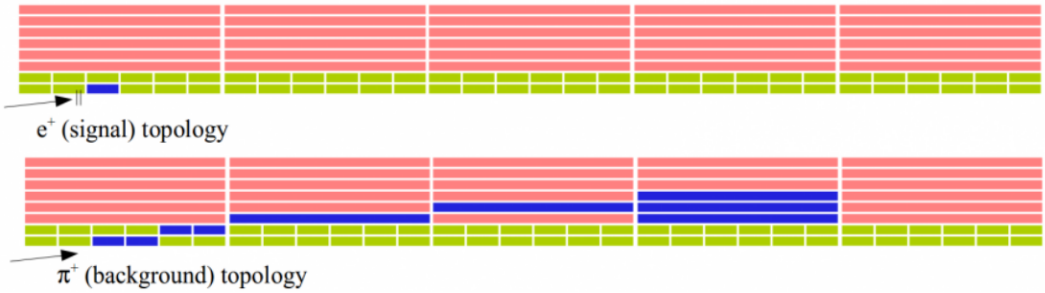

Figure 3.3: Visual representation of the particle shower development inside the decay tunnel. (top) Signal from a positron: it is identified by a hit in the t_0-layer (double vertical lines) and an energy deposit confined in the EM calorimeter (green blocks). (bottom) Signal from a charged pion: the energy deposit extends inside the energy tail catcher (red blocks).

3.1 The UCM technology

The building block of the electromagnetic sector of the ENUBET tagger is the Ultra Compact Module (UCM) (Fig. 3.4 and 3.5). It is a shashlik calorimeter with dimensions of $10 \times 3 \times 3$ cm^3 that covers 4.3 X_0. The longitudinal segmentation of ~ 4 X_0 allows to separate the electrons from the charged pions with a misidentification probability of $< 3\%$ [135].

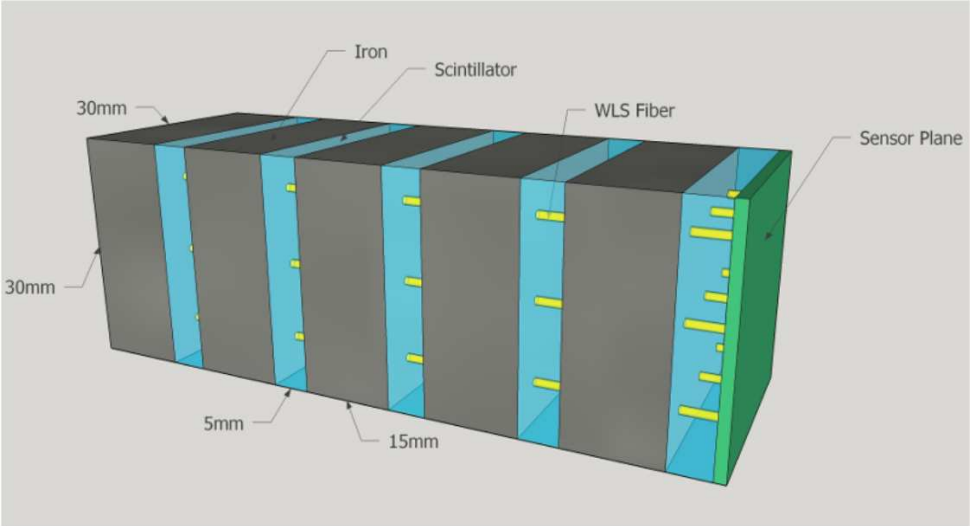

Figure 3.4: Schematics of the Ultra Compact Module.

The 10 tiles of absorbing (5) and scintillating (5) material are crossed by 9 fast (decay time < 3 ns) [129] WLS fibers (fiber density ~ 1 fiber/cm^2). Each of these fibers is coupled with a SiPM mounted on a custom PCB (Fig. 3.6). The 9 SiPMs are connected in parallel, non amplified and read out through a 470 pF decoupling capacitor. To read the sum of the current of the SiPMs, the PCB is equipped with a MCX connector and a push-pull coaxial connector (LEMO-00) for the bias [136]. The absorber for most prototypes is iron; it was preferred to lead for mechanical reasons, but also because it represents a more cost effective solution. As far as the scintillating material is concerned, different types of plastic scintillator have been tested (EJ-200, Uniplast, EJ-204...), along with two different types of WLS fibres (Y11 and BCF92), in order to evaluate the most efficient combination. The WLS fibers have a diameter of ~ 1 mm. The SiPMs have been provided by Fondazione Bruno Kessler and are based on the high density cell technology (HD-RGB) [137]. Different sizes of cells have been employed, but the sensitive area is the same (1×1 mm^2 for all the SiPMs used for the prototypes). A 3D printed mask is used to ensure the correct positioning of the fibers on the SiPMs (Fig. 3.6).

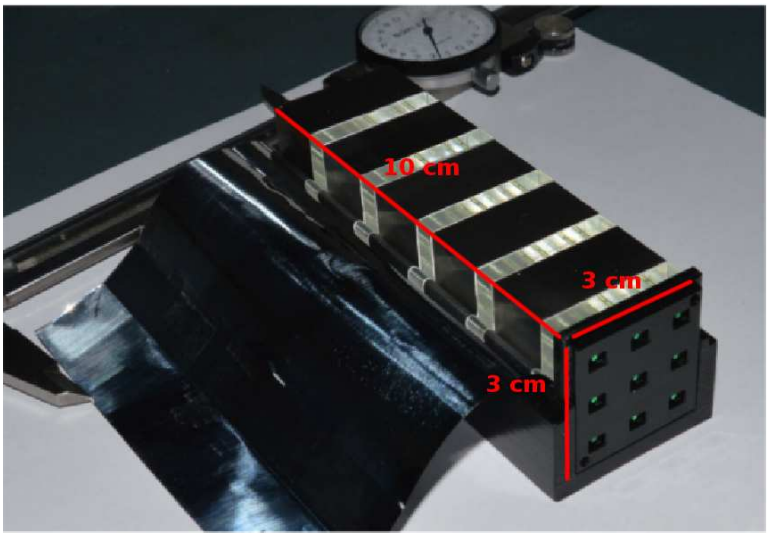

Figure 3.5: Ultra Compact Module; its dimensions are $3 \times 3 \times 10$ cm^3.

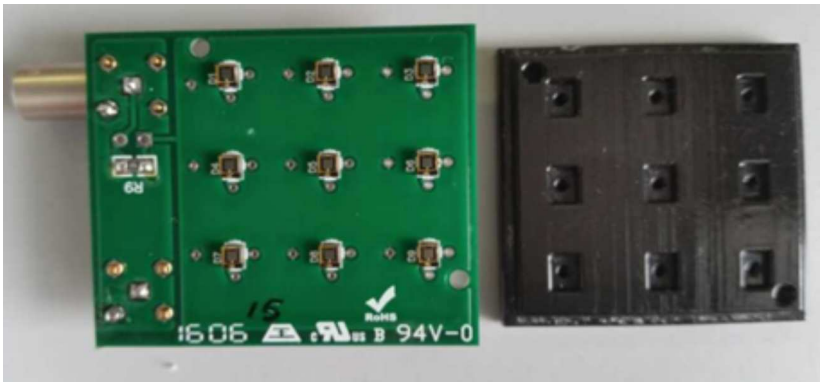

Figure 3.6: Printed Circuit Board and 3D printed plastic mask.

3.2 The feasibility proof

The first ENUBET prototype was in fact a feasibility proof developed by the INFN CSNV project called "SCENTT" [138]. The proof concerned the test of the possibility to longitudinally segment a shashlik calorimeter maintaining its linearity and energy resolution. The basic idea was to use a pre-existing shashlik calorimeter developed by the INFN FACTOR Collaboration (Fig. 3.7) and modify it in order to have a direct WLS fiber-SiPMs coupling in the longitudinal direction. This prototype was tested at the CERN PS-T9 beamline in August 2015 with negative particles in the 1-5 GeV energy range. The goal of the tests was to demonstrate that the performances in terms of energy resolution and linearity of the calorimeter were not compromised by the modified readout scheme compared with a standard light collection and readout system.

3.2.1 The test calorimeter

The modified shashlik calorimeter started from the one developed and tested by FACTOR in 2009 [139]. The calorimeter was made of two modules, each of them having 20 8×8 cm^2 tiles of 3.3 mm thick lead, interleaved with tiles of plastic scintillator of the same dimensions. The total length of each module covered $\sim 12\ X_0$ (Fig. 3.8).

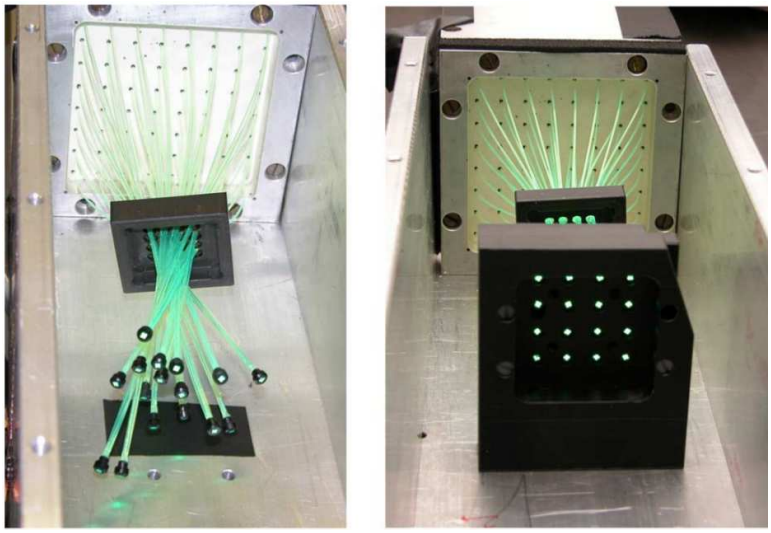

Figure 3.7: Picture of the FACTOR calorimeter fibers before the introduction of the SCENTT readout [139].

The number of SiPMs available for the test was not enough to equip both modules, so during the runs only one module at a time could be readout. A single module provided a longitudinal containment of a 1(5) GeV electromagnetic shower of 88% (83%). The modules were equipped with 64 0.8 mm diameter Kuraray-Y11 WLS fibers for the light collection. To evaluate the e/π discrimination capability, in the first module the fibers had

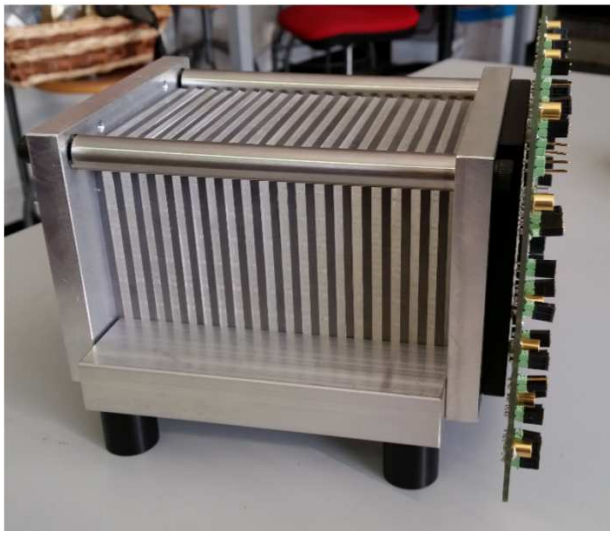

Figure 3.8: Picture of the first module of the calorimeter prototype [138].

two different lengths: half of them instrumented the whole $\sim 12\ X_0$ module, while the remaining half covered the module from ~ 6 to $\sim 12\ X_0$. The pattern of the short fibers, shown in Fig. 3.9, ensured that the sampling of the module was uniform in both halves. The second module, on the other hand, was equipped only with long fibers.
The readout board was instrumented with 64 SiPMs manufactured by Advansid [140], whose breakdown voltage V_{BD} was ~ 28 V, the active area was 1.13 mm^2 and the cell area $40 \times 40\ \mu$m^2. The SiPMs could be read independently or summed in groups of 4, for a total of 16 channels. The SiPMs were AC coupled to the output with 10 nF capacitors. A 3D printed mask held the PCB and aligned the SiPMs with the WLS fibers.

3.2.2 Results

The tests were performed at the CERN PS-T9 beamline with a mixed beam of negative particles (electrons, muons and pions) from 1 to 5 GeV/c. The experimental setup in the T9 area, from upstream to downstream, was the following (Fig. 3.10):

- one Cherenkov detector filled with CO_2 for particle ID;
- a 10×10 cm^2 plastic scintillator for the trigger;
- two pairs of Silicon Strip planes, in $x-y$ configuration, for the track reconstruction with a spatial resolution of $\sim 30\ \mu$m [141];
- a darkened metallic box containing the calorimeter modules.

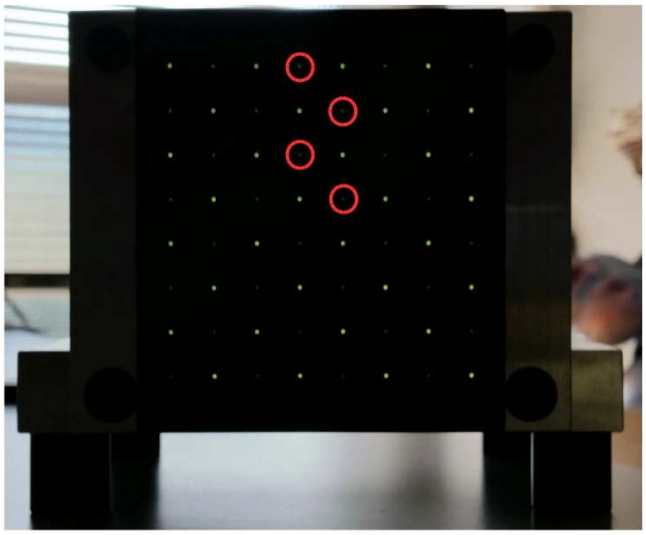

Figure 3.9: Closeup on the WLS fibers and the long/short pattern. The short fibers are highlighted with red circles [138].

The DAQ system was a standard VME system. The DAQ was controlled by a SBS Bit3 model 620 bridge optically linked to a Linux PC-system. The calorimeter readout was performed with both a charge integrating ADC (V792 QDC, CAEN) and two 8 channel 500 MS/s, 14-bit waveform digitizers (DT5730 and V1730, CAEN). The presented results were acquired using the DAQ system with the charge integrating readout. The particles for the analysis were selected in a fiducial area of 4×4 cm^2 on the upstream face of the calorimeter, centered on the axis of the calorimeter itself, by reconstructing the particle trajectory with the Silicon Strip Detectors (SSD). Another requirement was that the event was registered as a single track by the SSD system.

3.2.2.1 Linearity and resolution

Both the modules were tested with different overvoltages and with a tilt from the beam axis of 0 and 90 mrad. The 90 mrad tilt angle was set to simulate the average emission angle of positrons inside the decay tunnel [54], [142]. The different tested configurations are summarized in Table 3.1.
The module with short and long fibers (Long/Short) was mainly tested for e/π separation. This calorimeter was simulated with GEANT4 and the simulation compared with the data. The calorimeter, in all configurations, shows saturations effect around 4 GeV/c, with deviations from linearity of 2% at 4 GeV/c and 8% at 5 GeV/c (Fig. 3.11), larger than the ones in the simulation (Fig. 3.12); the reason is possibly due to the small number of cells (673) of the SiPMs.
The energy resolution, fitted with a $\sigma_E/E = S/\sqrt{E} \oplus C$ function (see Appendix A), is

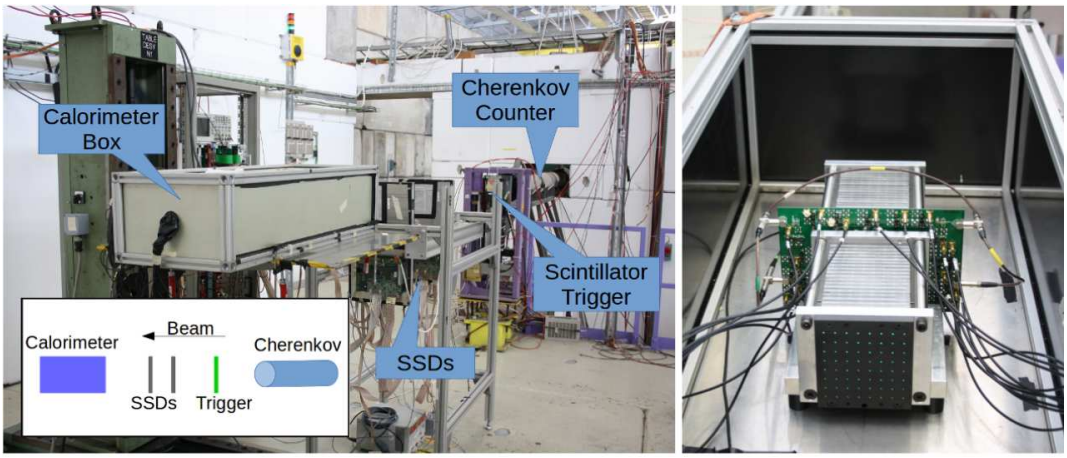

Figure 3.10: The experimental area (left) and the calorimeter in the darkened box (right) [138].

Configuration n.	Module type	SiPM overvoltage (V)	Tilt angle (mrad)
1	Long/Long	5	0
2	Long/Long	4	0
3	Long/Long	4	90
4	Long/Short	5	0
5	Long/Short	4	90

Table 3.1: Calorimeter configurations considered during the data taking.

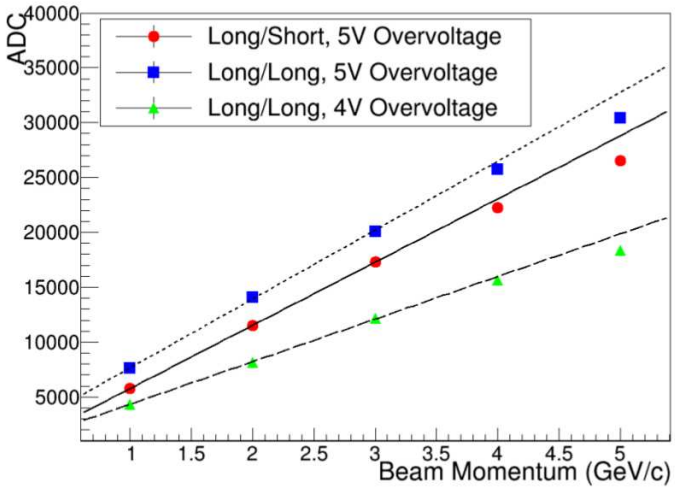

Figure 3.11: Energy linearity of the calorimeter from data in different readout configurations. The points have been fitted in the 1-3 GeV/c momentum range to highlight the deviation from linearity at 4 and 5 GeV/c [138].

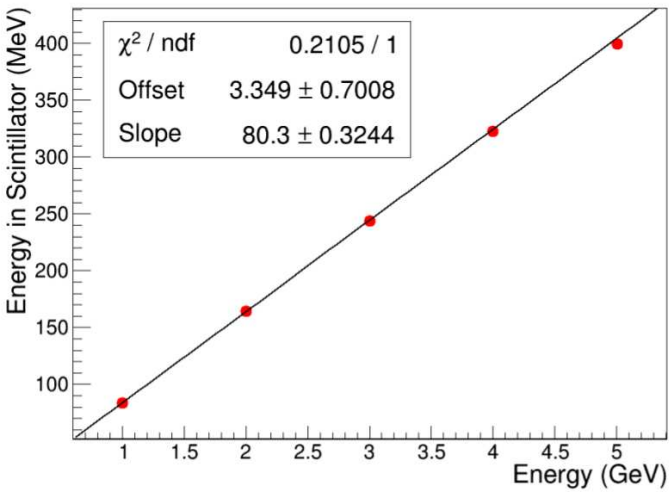

Figure 3.12: GEANT4 simulation of the energy linearity of the calorimeter [138].

comparable with the GEANT4 simulation (Fig. 3.13, 3.14) and with the one of shashlik calorimeters with similar features but operating with a standard fiber bundling scheme [143]; hence the novel readout scheme does not degrade the energy resolution performance. Moreover, a difference of 1 V overvoltage on the SiPMs does not affect the energy resolution. However, the Long/Short fiber configuration displays a deterioration in energy resolution, because of the non uniform sampling of the shower in the proximity of the maximum ($\sim 5\ X_0$ at 5 GeV/c).

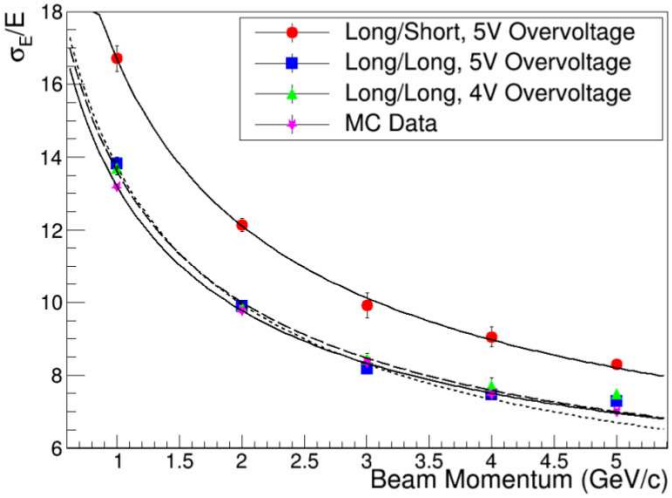

Figure 3.13: Energy resolution of the calorimeter from data and MC, 0 mrad tilt angle [138].

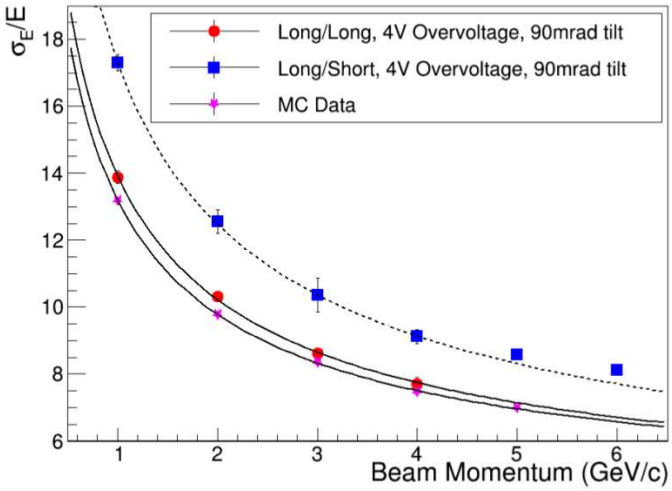

Figure 3.14: Energy resolution of the calorimeter from data and MC, 90 mrad tilt angle [138].

3.2.2.2 e/π separation

Since in ENUBET the hadronic and electromagnetic showers are meant to be distinguished by means of the longitudinal segmentation, the e/π separation was studied with the module instrumented with short and long fibers. The particles for this study were selected with the mentioned fiducial area and the Cherenkov counter was employed to select the electrons. Figure 3.15 shows the full spectrum collected in the calorimeter (black line) and the electron signal as selected with the Cherenkov counter (red line).
Figure 3.16 presents the signal collected by long fibers versus the signal from the short ones. From the plot it is possible to visually identify the region populated by the electrons. The two red lines are the combined energy cuts for the e/π separation. The cuts result in a purity of 95% for an electron efficiency of 98%, where the purity is defined as the ratio between the number of electrons tagged by the Cherenkov in the region above the thresholds and the total number of particles above the thresholds.

3.2.2.3 Nuclear Counter Effect (NCE)

With the photosensors placed directly on the beam, an effect to be taken into account is the Nuclear Counter Effect. It is the extra charge released by a particle hitting the photosensor, which is summed to the charge produced by the scintillation light. In order to estimate if and how much this extra charge contaminates the actual signal produced in the scintillator, a dedicated run at 5 GeV/c with no WLS fibers inserted in the calorimeter was performed. Electron events were selected with the Cherenkov counter, because, by producing showers, they maximize the probability of NCE events. Figure 3.17 shows the MIP events collected in a run with the WLS fibers inserted (blue dashed line), pedestal events (red dashed line) in

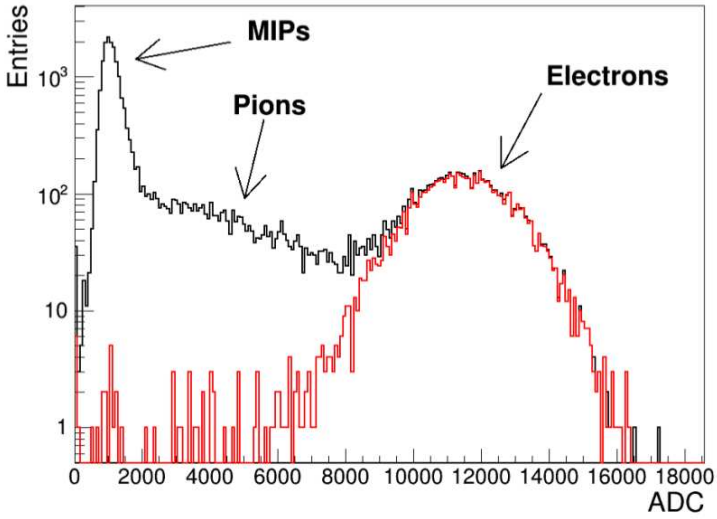

Figure 3.15: Full and Cherenkov-tagged spectrum of the calorimeter exposed to the 2 GeV beam [138].

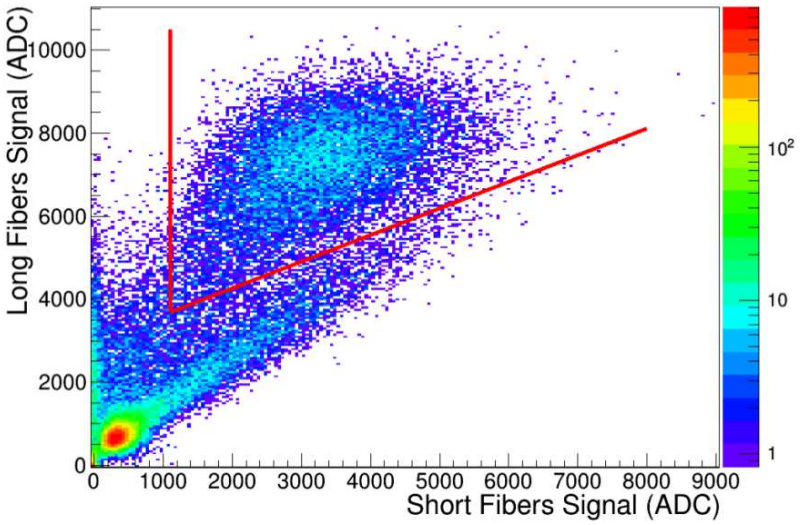

Figure 3.16: Signal collected by the long versus short fibers at 2 GeV/c. The red lines represent the energy cuts used for the electron identification [138].

the dedicated no fibers run, and the NCE events (black line). Pedestal events are those which do not produce signal inside the calorimeter (typically because they are particles registered by the trigger but that end up by not interacting with the calorimeter). The NCE peak is superimposed to the pedestal one and does not contribute to the nearby MIP region, hence this effect can be considered negligible.

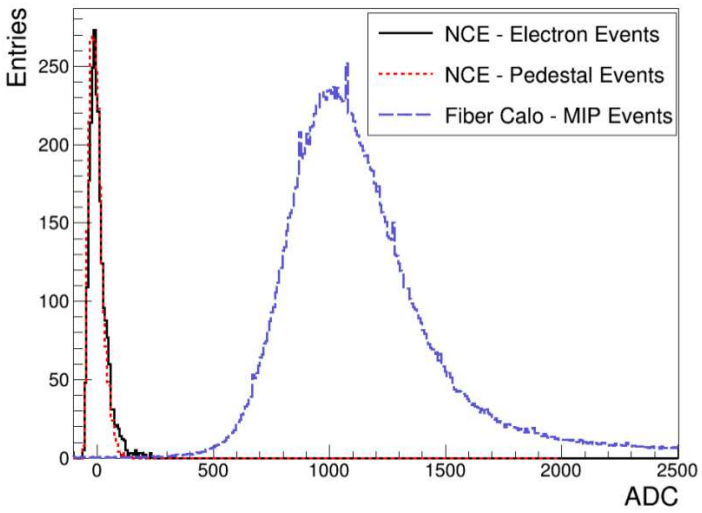

Figure 3.17: Comparison between the spectra recorded in the special "NCE" run without WLS fibers and a standard "Fiber Calo" run [138].

Chapter 4

Prototype development

Starting from the concept of the experiment, several steps are required to reach the objective of the 50 meters instrumented decay tunnel. In a period of 2 years an important prototype deveplopment campaign has been performed, to which I participated. The prototypes have been tested at the CERN PS-T9 beamline and exposed to a mixed beam of e^-, μ^-, π^-. The energy range of these particles was usually from 1 to 5 GeV, with some exceptions in which higher energies were explored (up to 6 GeV) as well as lower ones (0.5 GeV). The T9 beamline is located in the CERN East Area (Fig. 4.1), along with the T8, T10 and T11 lines. All the particles used in the East Area beamlines derive from the 24 GeV/c primary

Figure 4.1: Map of the CERN East Area [144].

beam from the PS. The provided cycles have a 2.4 s length with a flat top of about 400 ms in which the particles arrive in the experimental area [144].

After assessing in 2015 that shashlik calorimeters coupled with a compact readout based on SiPMs met the needs of the experiment, in 2016 the ENUBET Collaboration studied the modular technology of the UCM. In particular, a $\sim 30\,X_0$ calorimeter with an energy resolution of $<20\%/\sqrt{E}$ was assembled. 2017 saw the collaboration tackling several issues, first and foremost the SiPM survival to radiation and various concerns regarding construction simplification and costs containment, as well as the possibility to obtain faster signals. The results of the main prototypes tested from July 2016 to October 2017 are reported in the following sections in terms of linearity and energy resolution. The data presented in this chapter were analysed with ROOT [145].

4.1 The experimental setup

The experimental setup was more or less standard for all the beam tests, with little variations. A general description is given in order to better understand the steps of the data analysis common to all the prototypes characterization. Considering the beamline from upstream to downstream, the setup was composed of:

- two Cherenkov counters filled with CO_2 for particle identification, described in Appendix B;
- a 10×10 cm^2 plastic scintillator for the trigger;
- two pairs of 9.5×9.5 cm^2 silicon strip detectors (SSDs) for the particle track reconstruction (Fig. 4.2), described in [141];
- the calorimeter;
- ~ 20 cm of iron, to stop the pions that did not interact with the calorimeter;
- one or more plastic scintillators employed as muon catchers, to be used along with the Cherenkov counters for the particle ID.

The calorimeter was placed into a light tight box on a movable platform (DESY table). The vertical and horizontal positioning of the platform plane was controlled with a panel located outside the experimental area.
The setup for the beam test of November 2016 is reported in Fig. 4.3 and 4.4 as an example.

4.1.1 The Data Acquisition (DAQ)

The DAQ system was located inside the experimental area; it was based on VME (Versa Modular Eurocard) electronics and it was optically linked to a Linux-PC computer located itself inside the experimental area. Another PC in the Control Room was used to set the

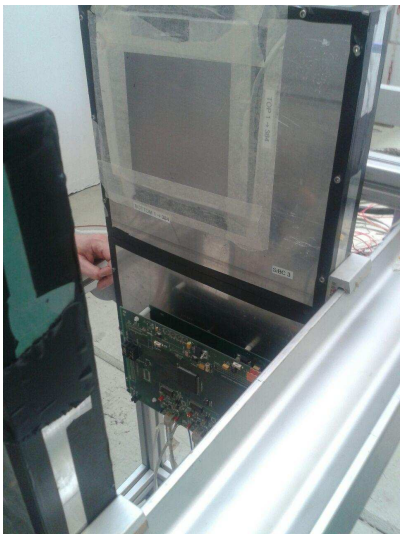

Figure 4.2: The SSDs used for track reconstruction in their aluminum boxes. The boxes are mounted on an aluminum structural frame, composed by a mixed set of Newport/Bosch elements.

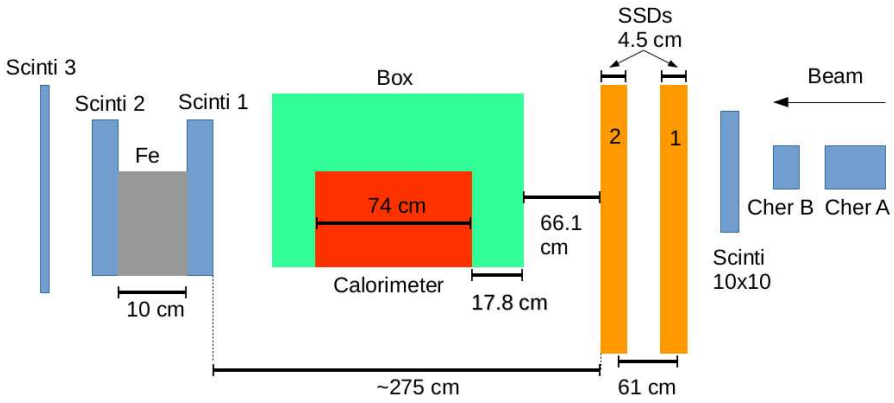

Figure 4.3: Layout of the experimental setup of November 2016 (not to scale). From upstream to downstream: two Cherenkov counters (Cher A and Cher B), a 10×10 cm^2 plastic scintillator, two pairs of silicon strip detectors (SSDs), the light tight box with the calorimeter inside, the first muon catcher (Scinti 1), 20 cm of iron and the two other muon catchers (Scinti 2, Scinti 3).

Figure 4.4: The experimental setup of November 2016. The muon catchers are not included in the photo.

slow control parameters, such as the HV values for the Cherenkov counters and the trigger scintillators. The two PCs were connected with a Gigabit Ethernet Link. A scheme of the DAQ is shown in Fig. 4.5.
To start the Data Acquisition two digital signals were required:

- a "spill" signal, provided by the accelerator. This signal was transformed in a $\sim$ 800 ms gate that was given as an input to the trigger board;
- a "particle trigger" which came either from the discriminated 10×10 cm^2 plastic scintillator signal, or from a coincidence of the same signal and the Cherenkov detectors ones.

Both these signals were shaped using a set of modules based on the NIM (Nuclear Instrumentation Module) standard. The trigger board evaluated the coincidence of these two signals and sent the trigger to the master VRB (VME readout board). The VRBs are the VME boards that read the silicon detectors: once received the trigger, they generate the hold signal to sample the strip pulse height, and start the readout sequence that transfers the data from the frontend electronics to the RAMs that store the events during the spill. The master VRB was designed to accept a "physical trigger" only if a spill signal was present and the SSDs were not "busy" for the readout operations. The acknowledgment of the SSDs status (busy or not) was also part of the VRB tasks, while as far as the coincidence condition was concerned, it was established by the VRB itself and the trigger board which handled the spill signal. The two boards communicated each other through the VME bus. When all the conditions were satisfied, a trigger signal was propagated to the other VME modules used to record the signals from the calorimeter, the Cherenkov detectors, the muon catcher(s) and

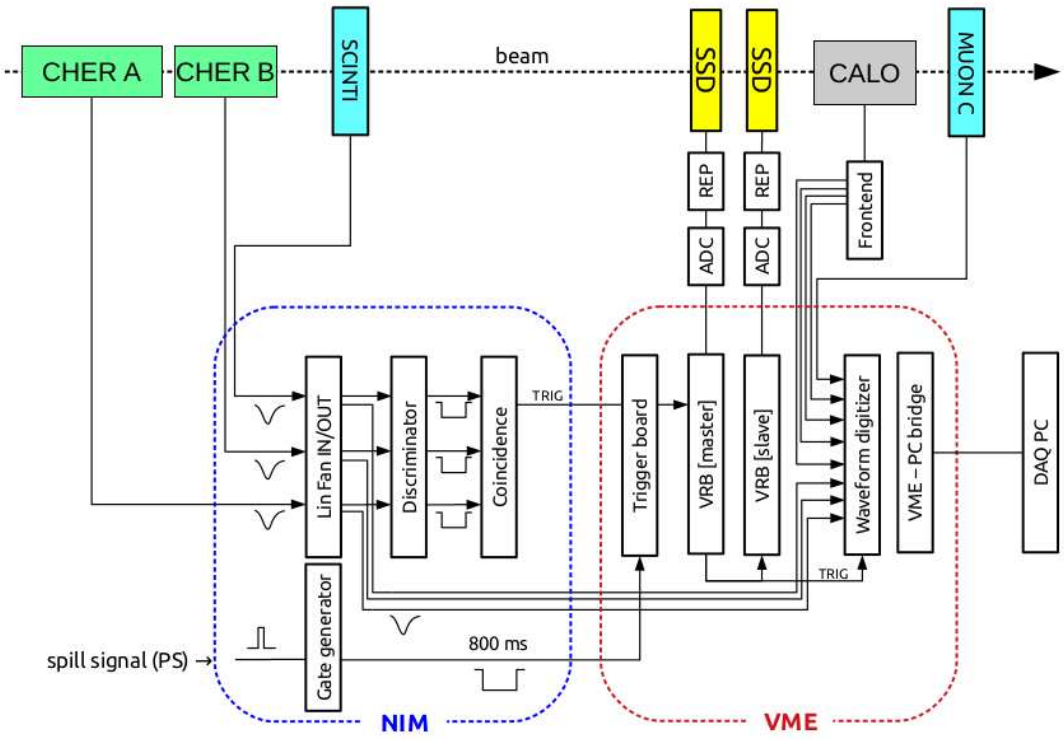

Figure 4.5: The scheme of the ENUBET Data Acquisition. The trigger is given by the coincidence of the signal from the upstream scintillator (SCINTI) and the spill signal from the PS. The trigger, as elaborated by the trigger board, is sent to the VRB [master] and, from there, to the other VME modules. The signal of the silicon detectors (SSD) is recorded by the VME readout boards (VRB), while the signals from the Cherenkov counter (CHER A, CHER B), the calorimeter (CALO), the muon catcher (MUON C) and the trigger scintillator (SCINTI) are recorded by the waveform digitizer.

the trigger scintillator too. At the end of the spill signal, the stored data were written to the DAQ PC. The used modules were either charge to digital (QDC) converter(s) or waveform digitizer(s). Custom waveform digitizers will be used to read the final detector because the acquisition inside the decay tunnel will be in triggerless mode, with the signal of the summed SiPMs sampled continuously during the beam extraction spill and later processed with a custom algorithm [138].
For the test performed on the prototypes, the waveform digitizers (Fig. 4.6) acquired analog waveforms and processed them through analog-to-digital converters (ADCs). While early digitizers were built on NIM or CAMAC (Computer Automated Measurement And Control), currently they operate with the VME standard. The number of bits used to represent the analog value gives the resolution of the digitizer, ideally giving 2N signal levels for an N-bit signal.

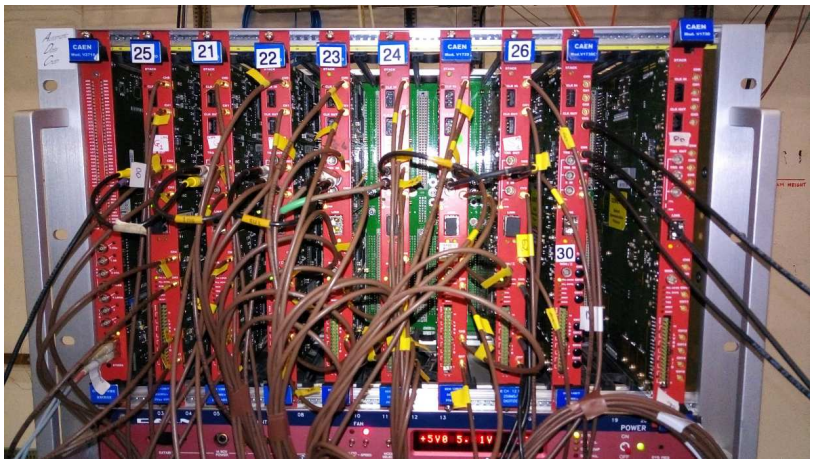

Figure 4.6: A set of digitizers used for the ENUBET beam test of November 2016.

To accurately reproduce a signal, the sample rate of the digitizers should be at least 3 or 4 times the frequency of the signal itself [146]. During the beam tests, the commercial waveform digitizer V1730 and V1720 by CAEN [147] were used. They have a sampling frequency of 500 MS/s and 250 MS/s, with an ADC depth of 14 bits and 12 bits, respectively. The input signal range was either 2 V or 0.5 V (in the V1730 case the input range can be changed). This choice allowed to acquire all the involved experimental signals (from the PMTs of the scintillators/Cherenkov detectors and the SIPMs of the calorimeter) with the same modules.
After the waveform digitizers received a trigger, the digital data from the ADCs were stored in a buffer memory whose depth determined the length of the signal that can be stored before being transferred. For the beam test the DAQ was set to save data for about 1 μs, that is 512 samples in the V1730 case (which samples the signal every 2 ns) and 256 samples in the V1720 one (1 sample every 4 ns).

When the spill signal terminated, all the data were written on the hard drive. Depending on the size of the data, the time needed to write the data varied from 2 to 10 s. The operation was performed in the inter-spill period which, depending on the cycle that was provided to the experimental hall, was about $\sim 14-20$ s.
On the trigger scintillator about 1.5×10^4 particles per spill on average were registered, but the number of particles accepted by the DAQ dropped to 100-500, depending on the number of detectors in the setup. This was due to two factors: the "busy" signal of the data acquisition and the particle distribution inside the spill. The "busy" signal generates a dead time that was given by:

- an incompressible time needed to operate the silicon detectors. It was given by the sum of the initialization time of the VRBs, ~ 200 μs, and the shift of the information of the 384 strips of each silicon layer from the 3 readout ASICs (connected to 128 strips each) to the VRBs. With the clock set at 2.5 MHz, this time was $\simeq 150$ μs;
- the ~ 1 ms readout time of the digitizers. The more the digitizers, the longer the dead time.

These times, along with the Poisson-like particle distribution inside the spill, gave the acquisition rate of the "raw" data.
A pre-processing routine was used to determine which part of the raw data was useful for the experiment and which was not. The data that the pre-processing discarded fell into two categories:

- pileup events. In the silicon detectors, the signals are shaped by the frontend electronics TA1 ASICs (by IDEAS[1]) in a few μs. If another particle hits the silicon plane in this time range, the detector would register them as a multi-hit. Given the number (4) and configuration of the silicon planes ($x-y$, $x-y$) tracks in multi hit events could not be reconstructed and hence are not useful for the analysis;
- missing hit. Typically the beamline optics is set to produce a focused beam. This allowed to hit a larger area of the calorimeter (tens of square cm) keeping the incoming beam size within the trigger scintillator size (10×10 cm^2). But when this beam configuration was used, some particles did not cross the sensitive region of the silicon strip planes, making it impossible to track them.

With these requirements, the amount of rejected data ranged usually between 20 and 50%.

4.2 Channel equalization

When a calorimeter is composed of more than one UCM, it is necessary to equalize the signal of all the channels in order to be able to sum them together and obtain the energy

[1] Integrated Detector Electronics AS [148]

released by a particle in the whole calorimeter. The signal differences from one UCM to another are due to several factors, from the slightly different breakdown voltage of the SiPMs to the coupling between the SiPMs themselves and the optical fibers. MIPs are used to equalize the signals from each channel; as they release an amount of energy that is defined per unit thickness in a given material, they are a good reference because if they travel the same path length their energy deposit in each UCM should be the same. The useful particles were those that crossed the UCM from front to back and did not exit from the sides, as this second possibility leads to a smaller and also unknown energy release in the UCM. The particles used for the channel equalization are selected in a fiducial area of 1×1 cm^2 around the center of the front face of the UCM. This selection, along with choosing for the equalization the run with the highest available energy, minimizes the chances to select MIPs that exit the UCM from the sides because of Coulomb scattering.
The SSDs are used to project the particle tracks down to the upstream face of the calorimeter. In Fig. 4.7 on the left, the black points are the x, y positions of the particles when they reach $z = z_{calorimeter\,front}$ and the superimposed red dots are the same particles with the requirement that they deposited most or all their energy in the calorimeter. This last requirement corresponds to setting an energy cut at $\sim$ 200 ADC counts in Fig. 4.9, which is the spectrum obtained by summing the non-equalized contribution of all the UCMs, thus excluding the events in the pedestal. The efficiency of the calorimeter (Fig. 4.7) is the ratio between the number of particles above threshold and the ones reconstructed by the SSDs.

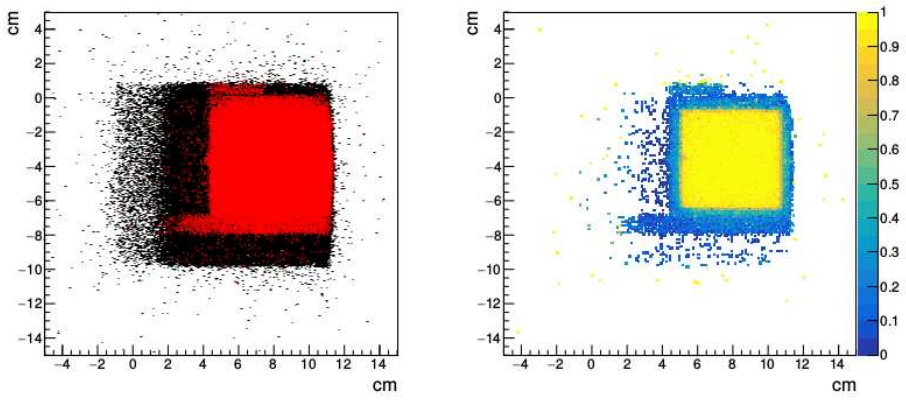

Figure 4.7: Calorimeter position reconstructed with the silicon strip detectors.

The efficiency map provides a precise position of the calorimeter as seen from the beam. The location of each UCM can be retrieved using the same procedure but performing the energy cut on the signal of a single UCM (Fig. 4.8), or can be inferred from Fig. 4.7 if the geometry of the calorimeter and readout order of the UCMs are known. After locating the UCMs it is possible to select for each of them the previously defined fiducial area. An example of the resulting signal is plotted in Fig. 4.10. The MIP peak is then fitted with a

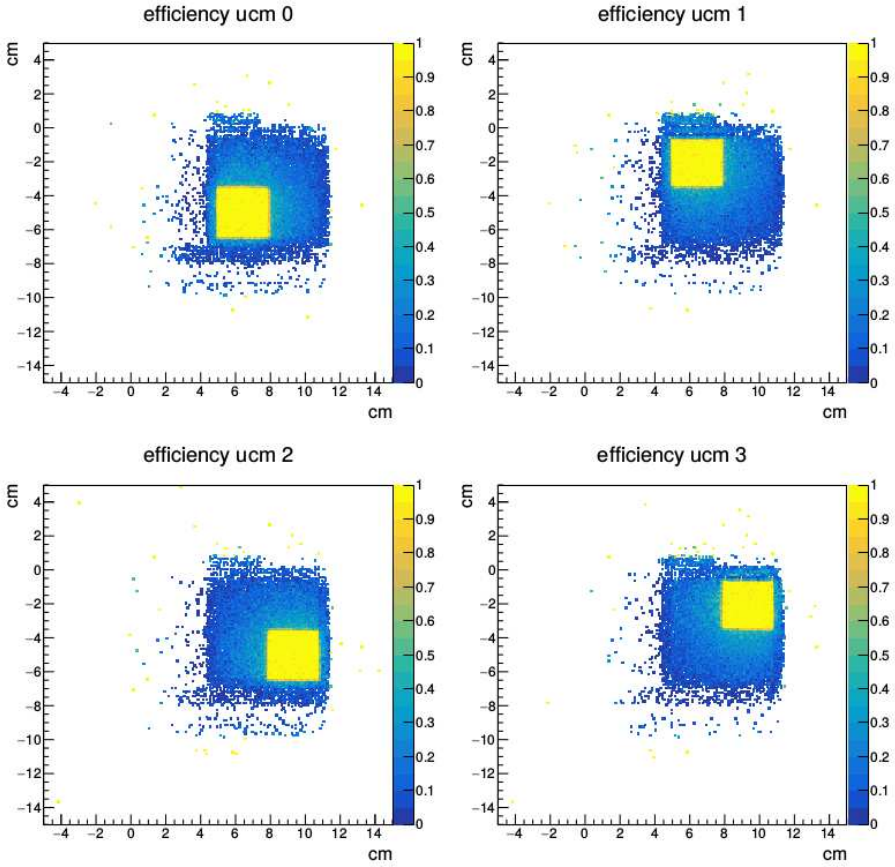

Figure 4.8: UCM position reconstructed with the silicon strip detectors.

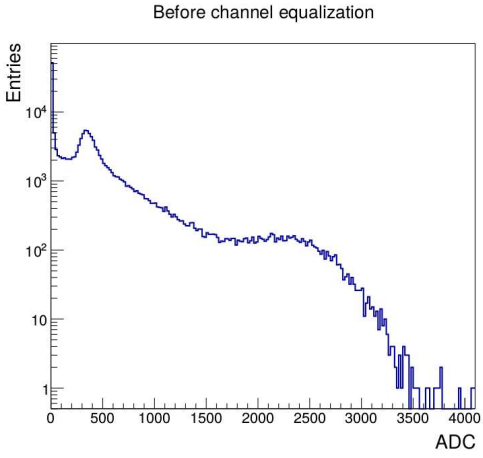

Figure 4.9: Energy deposit in the calorimeter before channel equalization.

Landau function [2].

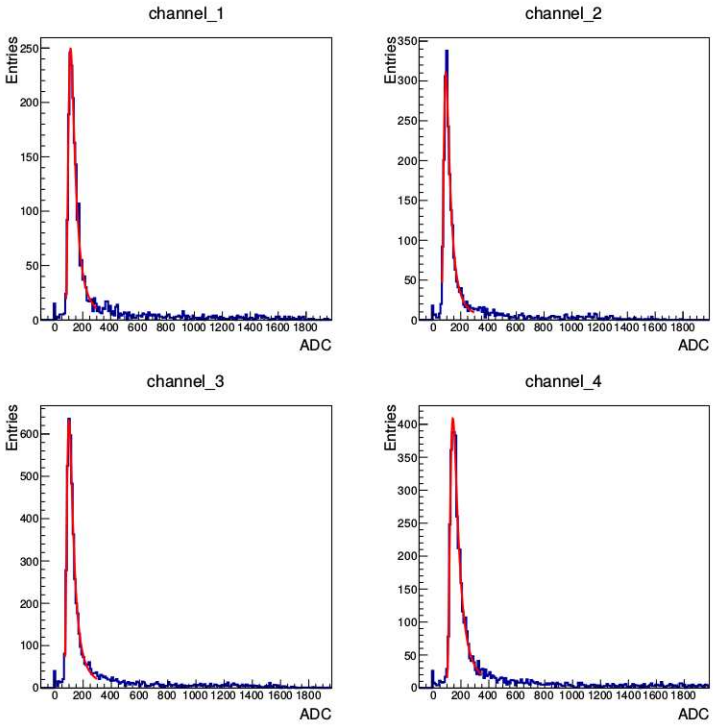

Figure 4.10: MIP peak fitted with a Landau function for the first four channels.

The MPVs (Most Probable Values) in general differ from one module to the other, for the already stated reasons. One module is arbitrarily taken as reference and the energy response of the others is equalized to the reference:

$$ADC_{i_{eq}} = \frac{MPV_{ref}}{MPV_i} \cdot ADC_i \tag{4.1}$$

where MPV_{ref} is the position in ADC counts of the MIP peak in the reference module, MPV_i is the MIP peak position in ADC counts of the $i-$th channel (associated to the $i-$th module), ADC_i is the unequalized energy deposit in ADC counts in the $i-$th module and $ADC_{i_{eq}}$ is the equalized energy deposit in ADC counts in the $i-$th module. After the equalization, all the channels have the same energy response in ADC counts and it is possible to sum their signal to obtain the energy spectrum of the whole calorimeter (Fig. 4.11).

[2] Probability distribution named after Lev Landau. It describes the fluctuations of energy loss by ionization in a thin layer of matter. It is similar to a Gaussian distribution with a longer tail at higher energies, populated by the rarer individual collisions that transfer larger amounts of energy. The Landau function used to fit the MIP peak is the predefined function of ROOT [145], defined in [149].

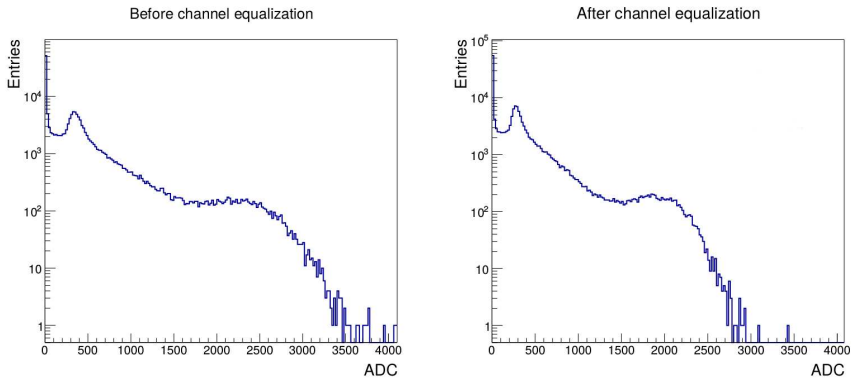

Figure 4.11: Comparison between (left) energy deposit in the calorimeter before the channel equalization and (right) energy deposit in the calorimeter after the channel equalization.

4.3 Data analysis

To characterize a calorimeter it is important to determine its performance in terms of linearity and energy resolution. The first step was to identify the electron peak. The fiducial area has to be defined, this time to make sure that the electromagnetic shower generated by an electron interacting with the calorimeter is contained as best as possible in the calorimeter itself. The fiducial area varies with the calorimeter geometry and transversal dimension, but as a general rule for the ENUBET calorimeters, it has to be located at least 0.85 Molière radii from the sides of the calorimeter itself [150], which was usually a compromise between shower confinement and statistics.
The two beam Cherenkov counters installed in the CERN PS-T9 beamline, described in Appendix B, were used for particle identification. In one of them the gas pressure was kept below the threshold for Cherenkov light emission by muons, thus allowing to select only the electrons. The second one was pressurized to detect both electrons and muons, but excluding the pions. By imposing the double condition of signal above threshold for this Cherenkov counter and below threshold for the electron only one, it is possible to select the muons. The electrons useful for the analysis were hence selected by combining the requirement of particles impinging in the fiducial area and tagged as "electrons" by the Cherenkov counters. Figure 4.12 shows the spectrum obtained considering the sum of the equalized signals from the UCMs (blue line), the same spectrum restricted to the selection of particles impinging in the fiducial area (red line) and the signal from the electrons in the fiducial area (green line). Depending on the transversal dimensions of the prototype calorimeter, the electron peak could show a slight asymmetry at lower energies due to incomplete lateral shower confinement. The electron peaks were then fitted with a Gaussian function or, to

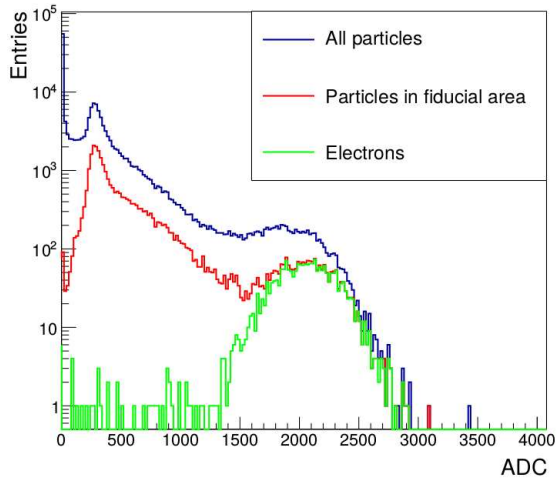

Figure 4.12: The electron peak, selected with the fiducial area cut and the Cherenkov tagging, is plotted in green.

have a better fit of the tail at low energies, a Crystal Ball [3] [151], a Gaussian with an exponential tail on the left.
The following sections are dedicated to the description of the tests performed and the results obtained for each prototype of shashlik calorimeter from July 2016 to October 2017. For every calorimeter the absorbing material was iron, while for the scintillating one different options were tested:

- a 12 UCMs calorimeter, with the EJ-200 plastic scintillator as the active material;
- a "supermodule", made of an electromagnetic calorimeter composed of 56 UCMs and an energy tail catcher, with EJ-200 plastic scintillator;
- a 12 UCMs calorimeter with the polysiloxane used as the active material;
- a 12 UCMs calorimeter with Uniplast tiles;
- a 12 UCMs calorimeter with the EJ-204 plastic scintillator.

[3] Named after the Crystal Ball Collaboration, it is a probability density function used to model various lossy processes in HEP. It is a Gaussian with an exponential tail at lower energies

$$f(x;\alpha,n,\bar{x},\sigma) = N\cdot\begin{cases}\exp(\frac{-(x-\bar{x})^2}{2\sigma^2}) & \text{for } \frac{x-\bar{x}}{\sigma^2} > -\alpha \\ A\cdot(B-\frac{x-\bar{x}}{\sigma})^{-n} & \text{for } \frac{x-\bar{x}}{\sigma^2} \leq -\alpha\end{cases} \tag{4.2}$$

$A = (\frac{n}{|\alpha|})^n \cdot \exp(-\frac{|\alpha|^2}{2}), B = \frac{n}{|\alpha|} - |\alpha|$
N is the normalization factor.

4.4 12 UCM calorimeter - July 2016

In July 2016 the first twelve module calorimeter [152] [153] was tested.

4.4.1 The prototype

The UCMs were arranged on an array of 2×2 modules on 3 layers (Fig. 4.13 and 4.14). The full length of the calorimeter covered 12.8 X_0 and granted a containment of $\sim 90\%$ ($\sim 80\%$) of the electromagnetic shower at 1 (5) GeV/c. The transverse size (6×6 cm^2) contained 92% of the shower at 5 GeV/c.

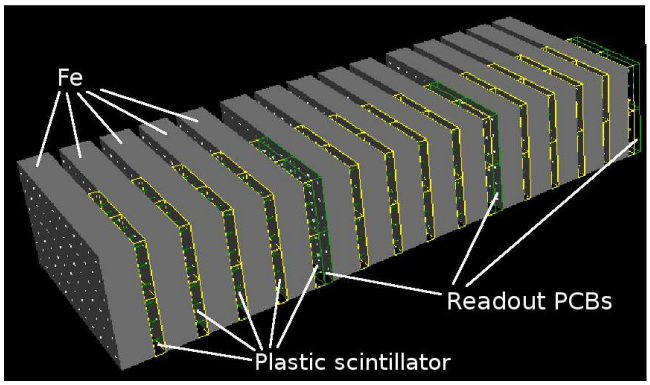

Figure 4.13: Schematics of the 12 UCM calorimeter tested in July 2016. The absorbing iron slabs are represented as full gray blocks, the scintillator tiles are the transparent ones with the yellow border and the PCBs are the green transparent tiles with the green border.

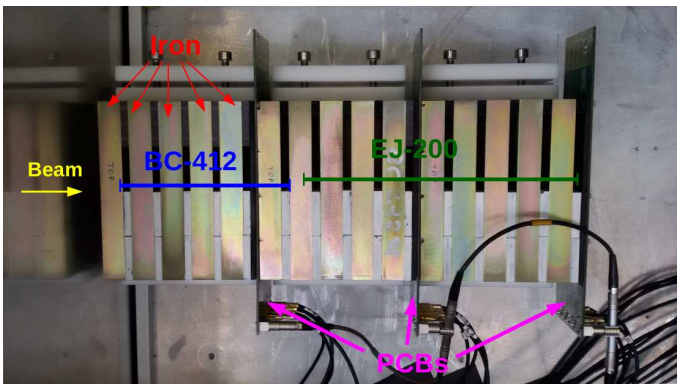

Figure 4.14: The 12 UCM calorimeter. Only half of the transversal size of the 6×12 cm^2 iron tiles was instrumented with plastic scintillators (white coated). The readout MCX cables and the LEMO for the bias attached to the 3 PCBs are visible at the bottom of the picture. The placement of the two different plastic scintillators is indicated.

Each UCM was made of 1.5 cm thick iron tiles coated with zinc, to prevent oxidation, alter-

nated with plastic scintillator tiles. On a total of 15 layers of plastic scintillator, nine used EJ-200, with a tile thickness of 5.5 mm, while for the remaining 6 BC-412 was used, with a tile thickness of 4.6 mm. All the scintillator tiles were painted with a diffusive TiO_2-based coating, the EJ-510, to increase the light collection efficiency. To allow the WLS fibres to cross the tiles, nine holes with a diameter of 1.2 ± 0.1 mm for each tile were drilled after painting with a CNC machine. The WLS fibers used for light collection were 1 mm diameter Y11 by Kuraray. The SiPMs had a 1×1 mm^2 active area and cell size of 20×20 μm^2, a breakdown voltage of 28 V and the overvoltage applied during operation was 3 and 5 V.
The signals from the calorimeter were recorded by a charge to digital converter, CAEN [147] V792, and with a digitizer, CAEN V1730, to test the waveform reconstruction algorithms [153]. The results obtained with the digitizer runs, reported in the following sections, were compatible with the measurements performed with the QDC.

4.4.2 Linearity and resolution

Figure 4.15 shows the linearity of the calorimeter with two different SiPM overvoltages. The linear fit was performed with the points from 1 to 4 GeV/c as the calorimeter energy response deviates from linearity at 5 GeV/c at the level of $\sim 3\%$. This deviation was observed for both applied biases and in both digitizer and QDC runs. The deviation is most likely caused by a partial longitudinal shower containment at higher energies.

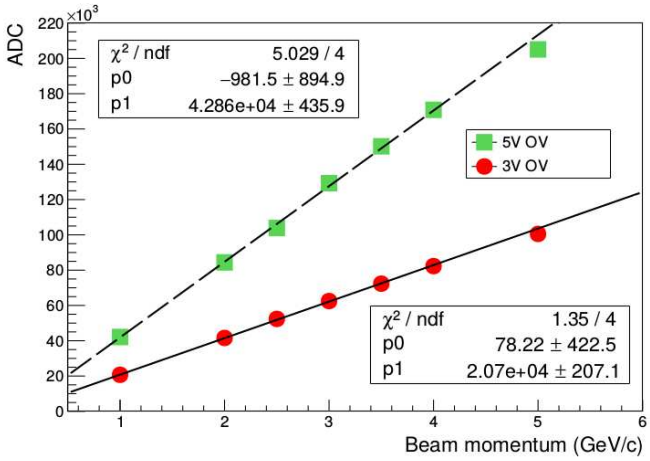

Figure 4.15: Linearity of the full calorimeter with a 31 V and 33 V bias for the SiPMs. Error bars are included but are too small to be seen.

The energy resolution σ/E (Fig. 4.16 and 4.17) was expected to be dominated by the sampling term (the 1.5 cm thickness of the iron tiles); it was fitted up to 4 GeV/c with the

following equation (described in appendix A):

$$\frac{\sigma_E}{E} = \frac{S}{\sqrt{E}} \oplus C \tag{4.3}$$

The result is in good agreement with the Monte Carlo simulation. The stochastic term, S in the equation, is $\sim$19%, within the requirements for the ENUBET calorimeter.

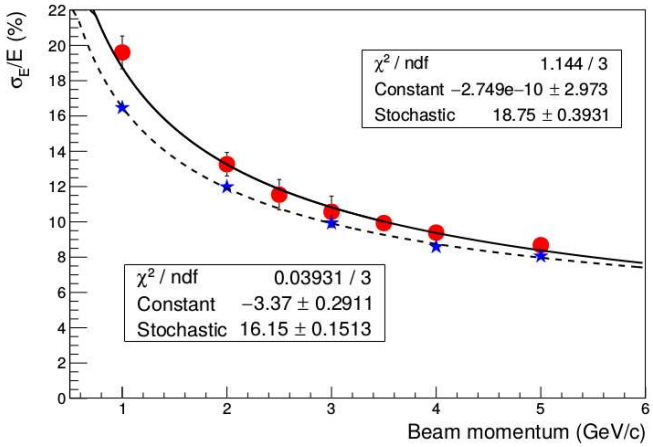

Figure 4.16: Energy resolution of the full calorimeter with a 31 V bias for the SiPMs (red dots) and the MC simulation (blue stars).

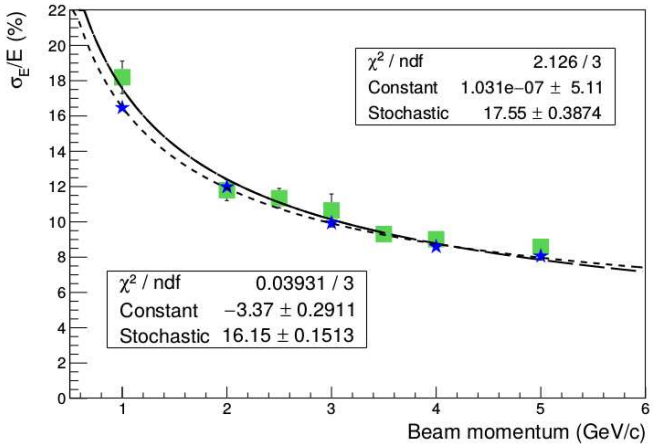

Figure 4.17: Energy resolution of the full calorimeter with a 33 V bias for the SiPMs (green squares) and the MC simulation (blue stars).

4.5 Supermodule - November 2016

In November 2016 a prototype that simulated a full section of the final tagger was tested. It featured a longitudinally segmented electromagnetic calorimeter, for which the UCM technology was employed, corresponding to the inner radii of the tunnel, topped by an energy tail catcher, with coarser granularity that would be placed in the tunnel at outer radii, to collect the tail of the hadronic showers (Fig. 4.18).

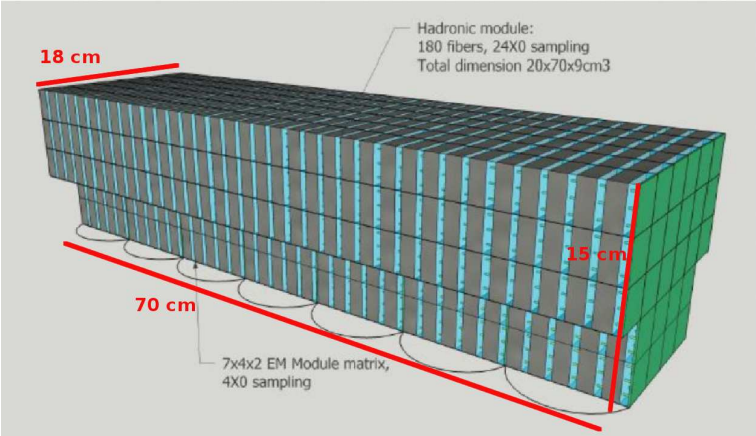

Figure 4.18: 3D picture of the supermodule. The electromagnetic (EM) calorimeter is topped by the energy tail catcher (hadronic module).

The prototype was characterized in terms of linearity, energy resolution and response to MIPs. Runs with the calorimeter tilted with an angle of 100 mrad with respect to the beam axis were also performed in order to simulate the average emission angle of positrons inside the decay tunnel.

4.5.1 The prototype

The prototype was made of two parts (Fig. 4.18, 4.19):

- an electromagnetic (EM) calorimeter made of 56 UCMs disposed on 7 layers, 2 $\times$ 4 UCMs each. The dimensions were $12 \times 6 \times 70$ cm^3. The absorber tiles were 6 $\times$ 12 cm^2 and the scintillating ones were UCM-size, 3 $\times$ 3 cm^2 (Fig. 4.20). The first five layers of the electromagnetic calorimeter were instrumented with 1 mm diameter Y11 multi-clad WLS fibres by Kuraray, while in the last two the signal was brought from the plastic scintillator to the SiPMs via 1 mm diameter BCF92 multi-clad WLS fibres by Saint Gobain (Fig. 4.19);

- an energy tail catcher (or “hadronic”, H, calorimeter), which was a shashlik calorimeter with a compact readout based on SiPMs, but was not made of UCMs and hence

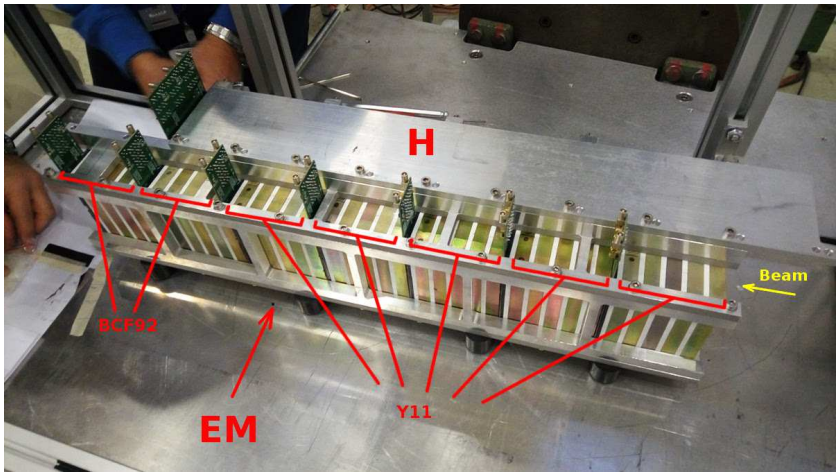

Figure 4.19: November 2016 prototype. The detector is laying on its side, rotated by 90°. The location of the different employed WLS fibers is indicated.

Figure 4.20: One layer of the electromagnetic calorimeter, made of 8 UCMs. The tiles of plastic scintillator are not a single piece, but each is composed of 8 UCM-size tiles (3×3 cm^2).

it had a coarser granularity. Its dimensions were $18 \times 9 \times 60$ cm^3. The energy tail catcher had no longitudinal segmentation as it was read at the end ($\sim 26\ X_0$) and, albeit being readout by 18 channels, each collecting the signal from the sum of nine SiPMs just like the UCMs, they were all connected to the same 9×18 cm^2 tiles of plastic scintillator (Fig. 4.21, 4.22 left). The fiber frequency was the same as the electromagnetic calorimeter. The energy tail catcher was half instrumented with Y11 and half with BCF92, whose positioning followed the pattern in Fig. 4.22 right.

Figure 4.21: The energy tail catcher. The tiles of plastic scintillator, differently from the tiles of the electromagnetic calorimeter, are a single piece (see Fig. 4.20).

Both detectors had 1.5 cm thick iron tiles coated with zinc as absorber material, and 0.5 cm thick EJ-200 tiles coated with diffusive TiO_2-based paint (EJ-510) as scintillator. All the fibers were read by 1 mm^2 SiPMs with $20 \times 20\ \mu$m^2 cell size developed by FBK [140], with breakdown voltage at 28 V; the applied overvoltage was 8 V for the SiPMs coupled with Y11 fibres, 9 V for those coupled with BCF92 fibers. The readout of the whole calorimeter was performed by 10 8 channel V1720 CAEN [147] waveform digitizers (12 bit, 250 MS), while the two Cherenkov counters, the trigger scintillator and the muon catchers were read with a 8 channel CAEN Desktop digitizer DT5730 (14 bit, 500 MS).

4.5.2 Channel equalization

The prototype for this beam test was composed of two different detectors. In order to equalize and sum the energy deposit in the whole calorimeter (electromagnetic (EM) segment plus the energy tail catcher (H)), more steps are needed:

- the first one is a custom channel equalization, for the EM and H calorimeter separately. To equalize the channels dedicated runs at 7 GeV/c were performed. The higher momentum beam was set to lessen the coulombian scattering of the MIPs,

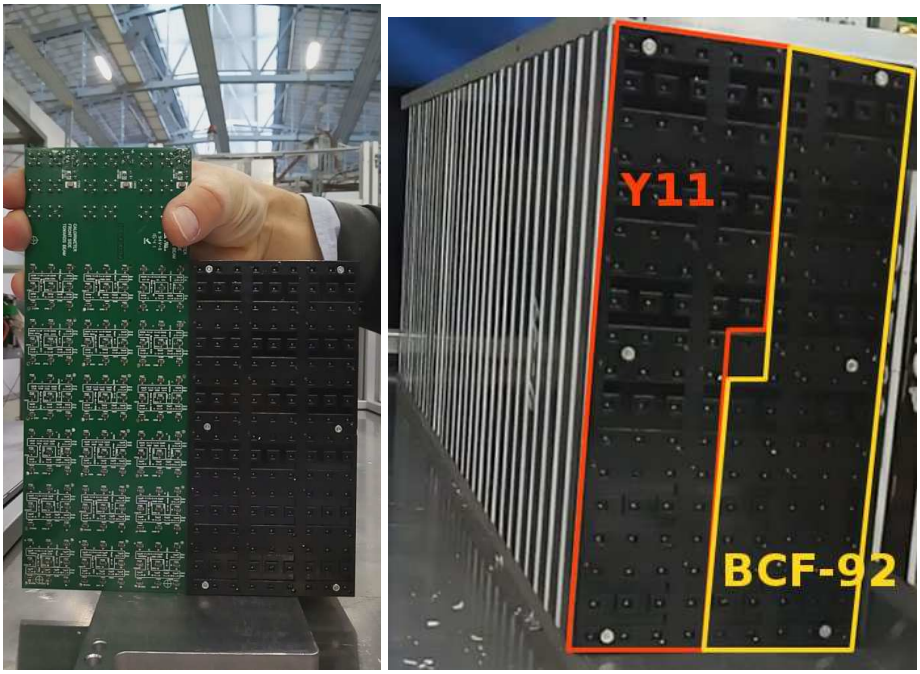

Figure 4.22: (left) The PCB and the 3D printed plastic mask of the energy tail catcher. (right) Location of Y11 and BCF-92 multi-clad WLS fibres inside the energy tail catcher.

given the length of the calorimeter, and to have a clear MIP peak in the more downstream layers. The size of the calorimeter exceeded the active area of the silicon strip detectors, so it took a total of 5 runs with 5 different DESY table settings in order to illuminate the full detector. The channels of the energy tail catcher were analysed like the UCMs, each one with its own fiducial area. Figure 4.23 presents the MPVs of the Landau fit for each channel versus the UCM readout number. The last layer of 8 UCMs has a signal $\sim$50% smaller than the layers 2 to 6. In particular, this difference occurs also between layer 7 and 6, which were equipped with the same WLS fibres, the BCF-92 ones. A reason for this might be due to how the fibers were cut and polished: no standard procedure or mask were used, so it is possible that the fibers of the seventh layer were cut all fairly equal to one another, but shorter than the fibers of the other modules, resulting in a not perfect fiber-SiPM contact;

- after equalizing the channels for each of the two detectors, the following step requires to equalize the signal of the two calorimeters. The two calorimeters have a different granularity, both longitudinally and transversally, so their channels cannot be compared. However, for the two calorimeters both the absorbing and scintillating tiles are machined from the same materials, with the same thickness and same coating, hence a MIP interacts in the same way. A GEANT4 simulation (Fig. 4.24) of the energy

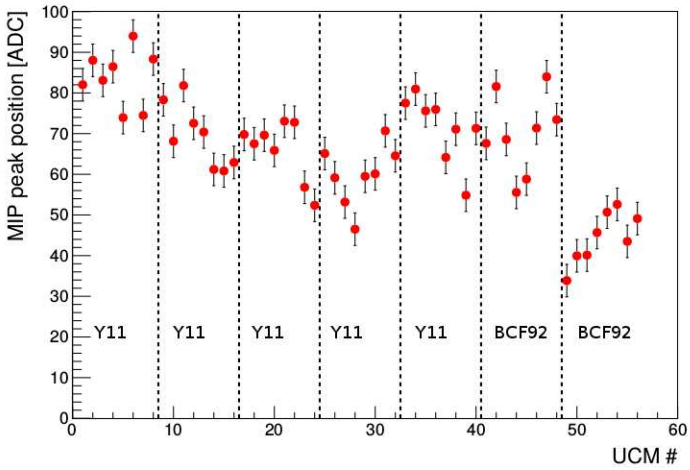

Figure 4.23: MPV in ADC counts vs UCM number. The WLS fibres for each layer are indicated.

tail catcher was performed with a 7 GeV/c point-like muon beam, impinging on the detector 1 mm on the side of the center in order to avoid the hole of the central WLS fibre. The simulated energy deposit in the 30 scintillator tiles of the energy catcher was 32.67 MeV. The same amount of energy is deposited by a MIP in the first six layers of the electromagnetic calorimeter;

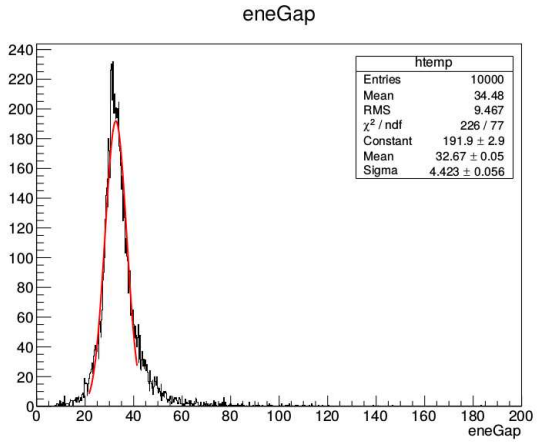

Figure 4.24: Simulated energy deposit in the energy tail catcher in MeV. The momentum of the point-like beam is 7 GeV/c and the particles are impinging 1 mm off the center of the calorimeter.

- at this point it is possible to convert the ADC counts to MeV:

$$MeV_{i_{eq}} = \frac{MIP_{MeV_{Scinti}}}{MIP_{ADC}} \cdot ADC_{i_{eq}} \tag{4.4}$$

where $MeV_{i_{eq}}$ is the energy deposit in MeV in the i-th channel, $MIP_{MeV_{Scinti}}$ is the energy deposit in 30 layers of plastic scintillator by a MIP as computed by the Monte Carlo simulation, MIP_{ADC} is the energy deposit in 30 layers of plastic scintillator by a MIP from data, and $ADC_{i_{eq}}$ is computed from equation 4.1. After this equalization the energy deposit in the two calorimeters can be summed (Fig. 4.25).

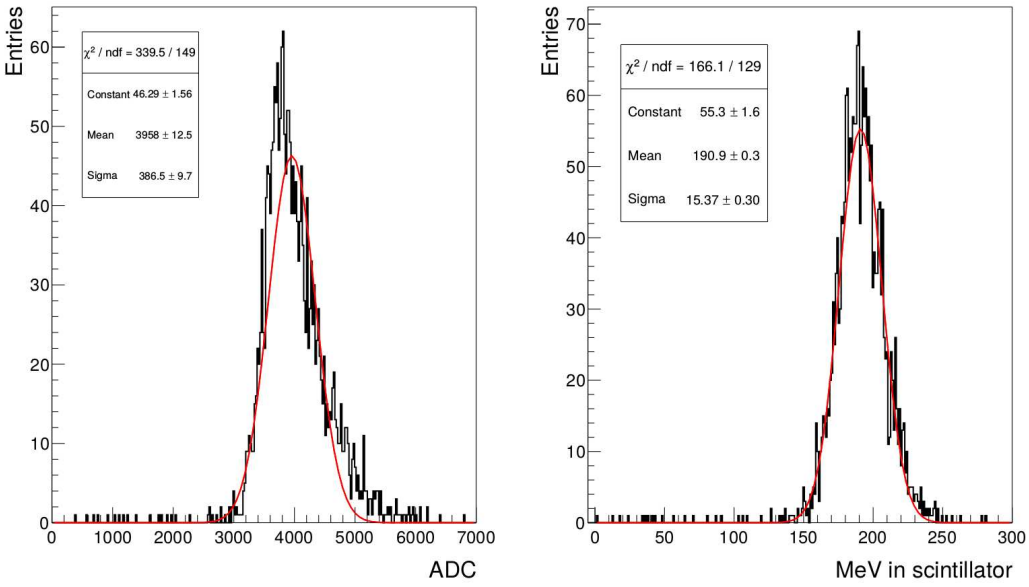

Figure 4.25: (left) Sum of the electron signal of the EM and H calorimeters prior to energy calibration. A tail at high energies due to the different response of the detectors is visibile. (right) Sum of the electron signal of the EM and H calorimeters after the energy calibration. The tail at high energies is absent. Both histograms were fitted with a Gaussian function.

4.5.3 Linearity and resolution

The resulting linearity and energy resolution for the full calorimeter (electromagnetic EM plus energy tail catcher H) at a 0 mrad tilt angle with respect to the beam axis are displayed in Fig. 4.26 and 4.27.

The energy resolution was comparable with the results of July 2016. The linearity was fitted up to 5 GeV/c and the deviation from linearity is $< 3\%$ for all the energies, due to the better electromagnetic shower containment given by the larger dimension of the calorimeter. An error of 1% on the x-axis was added, to account for the momentum bite of the beam [155].

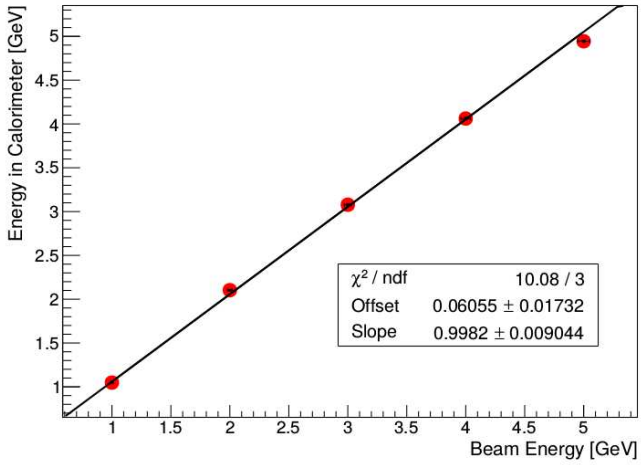

Figure 4.26: Linearity of the full calorimeter (EM+H) at a 0 mrad tilt.

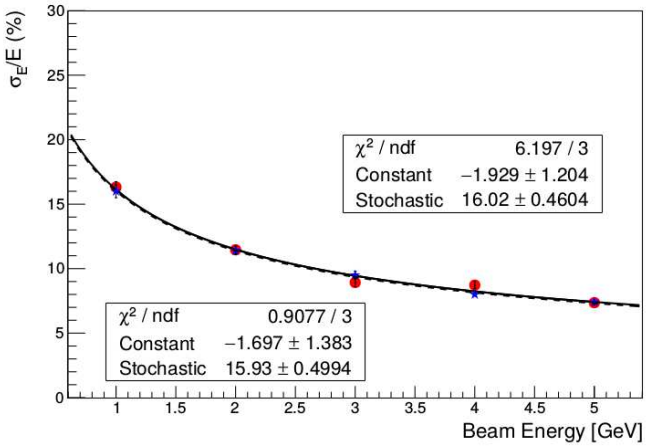

Figure 4.27: Energy resolution of the full calorimeter (EM+H) at a 0 mrad tilt (red dots) and the MC simulation (blue stars). The MC analysis is described in [154].

Runs with the calorimeter with a 100 mrad tilt angle with respect to the beam axis were also performed in order to simulate the average emission angle (88 mrad) of the positrons inside the decay tunnel. For these runs, the fiducial area (Fig. 4.28) was set to select particles that interacted with the calorimeter in a tunnel like situation, hitting the side of the electromagnetic calorimeter first and ending their travel in the energy tail catcher. Figure 4.29 and 4.30 present the linearity and energy resolution for the whole calorimeter at a 100 mrad tilt angle.

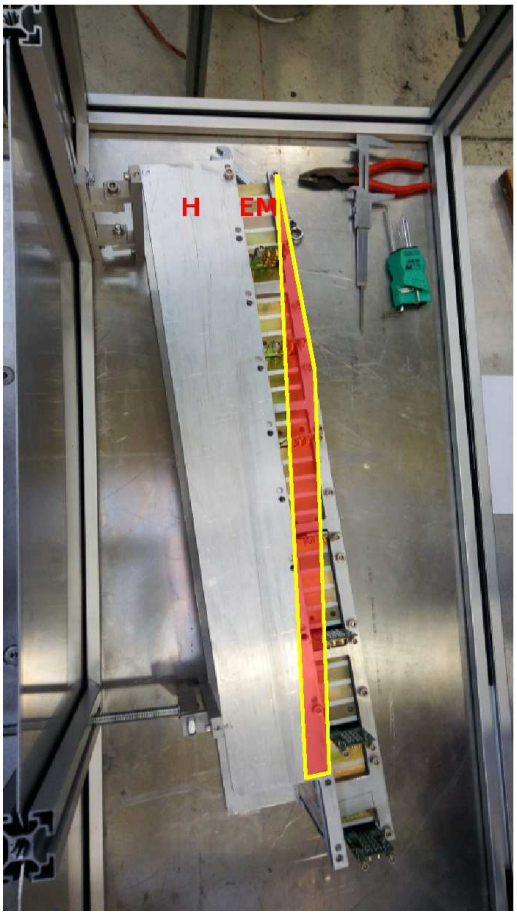

Figure 4.28: Fiducial area (in red with yellow border) for the runs at 100 mrad.

The results at a 100 mrad tilt were compatible with those at 0 mrad, meaning that the energy resolution was dominated by the sampling term and that the tilt did not undermine the performance of the detector.

4.5.4 Response stability for the single UCM

The data acquired with this calorimeter were also used to check the response stability of a single UCM in time. The longest runs where those at 5 GeV/c, because the electron frac-

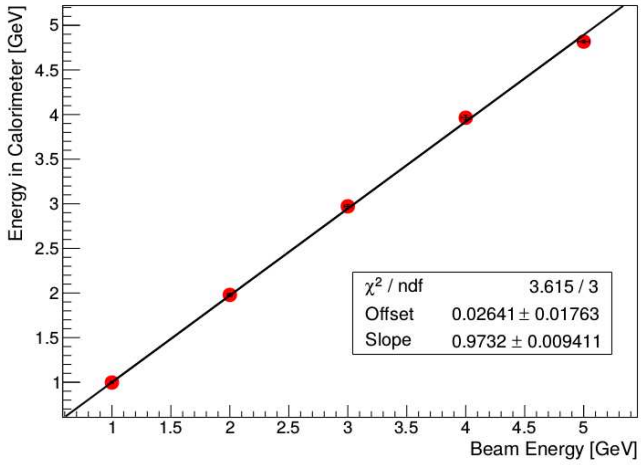

Figure 4.29: Linearity of the full calorimeter (EM+H) at a 100 mrad tilt.

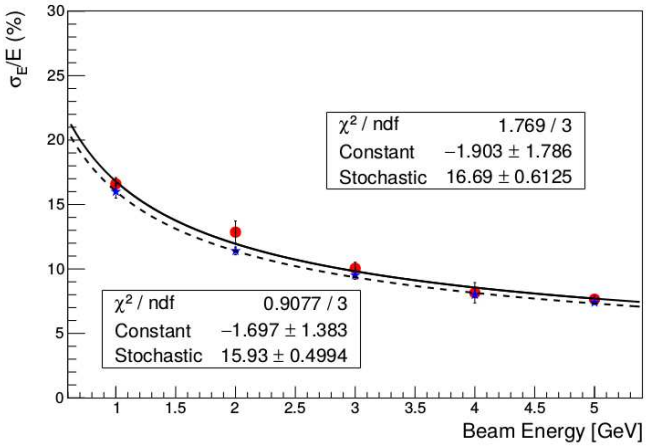

Figure 4.30: Energy resolution of the full calorimeter (EM+H) at a 100 mrad tilt (red dots) and the MC simulation (blue stars). The MC analysis is described in [154].

tion in the beam decreases with beam momentum, so more time is required to accumulate statistics. The selected run was taken during nighttime for approximately ten hours (from 22:53 9/11/2016 to 08:46 10/11/2016). The energy deposit in Fig. 4.31 in ADC counts is plotted versus the run time in seconds for the electromagnetic calorimeter (56 UCMs), whereas Fig. 4.32 shows the same for UCM # 28, taken as an example. The plot in Fig. 4.32 was then sliced every 10 bins on the time axis, allowing to observe the energy deposit in the UCM every 30 minutes. The projections on the y axis were then fitted with a Landau and the corresponding MPV was saved along with the fit error. The MPVs are plotted in Fig. 4.33, together with the linear fit. In the UCMs the response was found to be stable within the uncertainty of the position of the MIP-like peak and not correlated with changes in temperature.

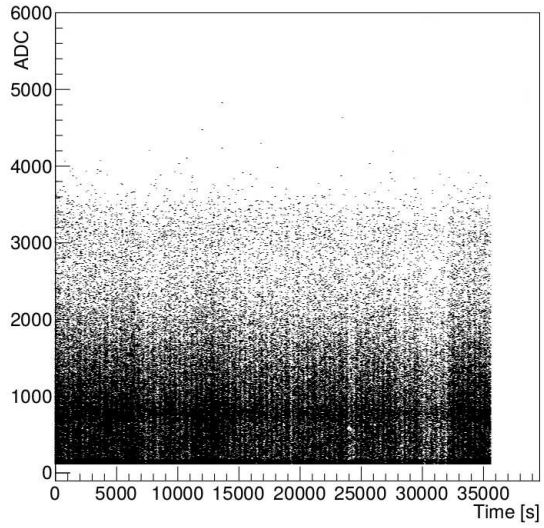

Figure 4.31: Energy deposit in the whole calorimeter vs time.

4.5.5 e/π separation

Using the energy deposit in the 7 layers of the electromagnetic calorimeter and in the energy tail catcher, a study of e^-/π^- separation was performed with a run at 3 GeV/c and the calorimeter tilted by 100 mrad from the beam axis. At first a particle (electron or pion) was identified with the Cherenkov counters. Then it was observed which percentage of the total energy deposited in the whole calorimeter was registered in each layer and part of the calorimeter itself for a given particle. With this information, energy cuts were identified and then applied to the layers of the electromagnetic calorimeter and to the energy tail catcher. The particle identification performance of these cuts was compared to the particle

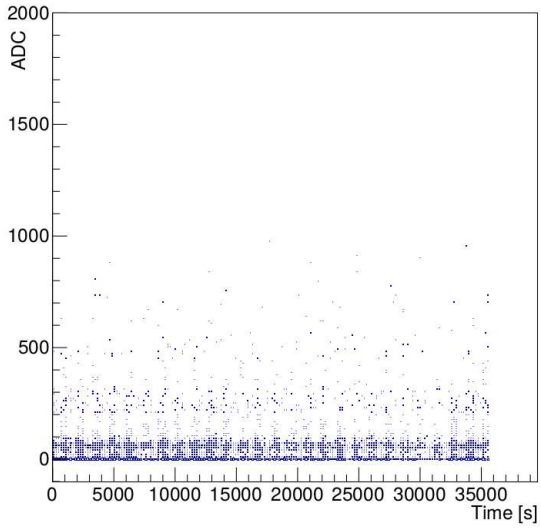

Figure 4.32: Energy deposit in the UCM # 28 vs time.

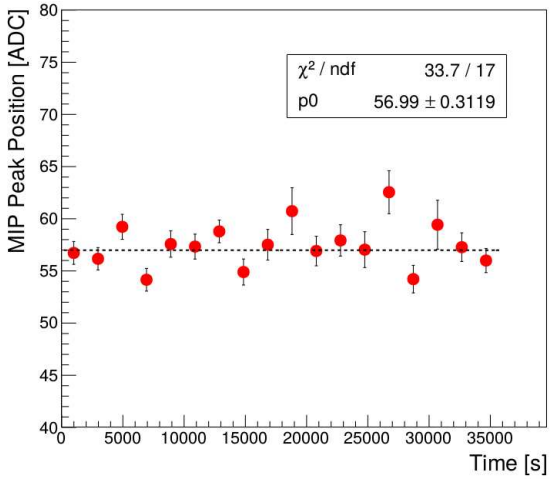

Figure 4.33: MPVs of the Landau fit of the 10 bins slices vs time. The particles are selected with a fiducial area of 1×1 cm^2. No indication of temperature or time induced patterns is observable.

	From Cher.	From segmentation	Segm. + Cher.	Efficiency	Purity
e^--like	332	234	214	70 %	91 %
π^--like	2547	1832	1624	72 %	89 %

Table 4.1: Efficiency and purity of the electron and pion peak reconstruction performed with energy cuts in the layers of the electromagnetic calorimeter and the energy tail catcher.

identification performed by the Cherenkov counters. Figure 4.34 shows the electron peak reconstructed by both the energy cuts and by the Cherenkov counters (both of them using particles in the fiducial area defined for the 100 mrad tilted runs), and Fig. 4.35 shows the same for the pion peak. Table 4.1 reports the values of efficiency and purity obtained for the particle ID performed with these energy cuts.

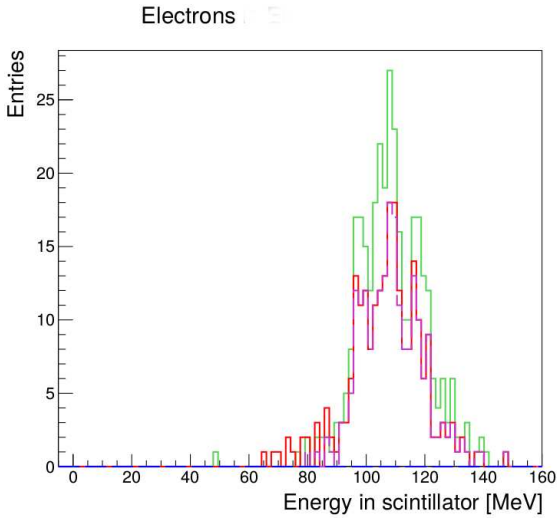

Figure 4.34: Electron peak reconstructed with the Cherenkov counters and/or the energy cuts. (green line) e^- peak from Cherenkov counters. (red line) e^- peak from energy cuts. (magenta line) e^- peak from energy cuts plus Cherenkov counters. (blue line) μ^- mistagged as e^- by the energy cuts.

In the ENUBET decay tunnel, the energy of the positrons produced by K_{e3} decays will not be monochromatic and nor will have the same impact angle on the detector (see Section 2.2), so the e/π separation is currently being investigated with simulation techniques.

4.5.6 2016 conclusions

In 2016 two prototypes of shashlik calorimeters with embedded readout based on SiPMs and with 4.3 X_0 longitudinal granularity were tested at the CERN PS-T9 beamline. The performances of the two prototypes were within the ENUBET requirements. In particular, the supermodule tested in November 2016 had an energy resolution of $\sim 17\%/\sqrt{E(\mathrm{GeV})}$

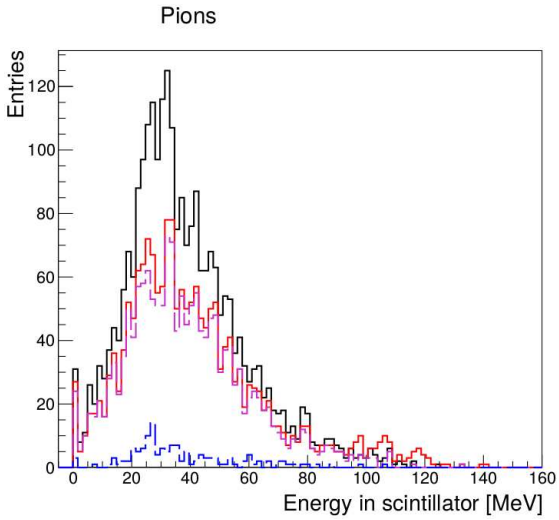

Figure 4.35: Pion peak reconstructed with the Cherenkov counters and/or the energy cuts. (black line) π^- peak from Cherenkov counters. (red line) π^- peak from energy cuts. (magenta line) π^- peak from energy cuts plus Cherenkov counters. (blue line) μ^- mistagged as π^- by the energy cuts.

and it was linear in the 1-5 GeV energy range, with deviations from linearity within 3%. In comparison with the standard 0 mrad tilt runs, the runs with the prototype tilted by 100 or 200 mrad from the beam axis did not introduce any significant change. The final indication was that the mechanical coupling between the fibers and the SiPMs needs to be improved, as it dominates the disuniformities in the response from one UCM to another. Equalizing the UCM signals with the MIP peaks allows to remove this effect and does not compromise the detector performance [150].

4.6 Irradiation tests

The design of the ENUBET calorimeter allows to longitudinally segment the detector, removes the dead areas introduced by conventional light extraction and is very compact; however it exposes the SiPMs to fast neutrons produced in hadronic showers. The survival of these photosensors in harsh radiation evironments is still an issue [156–160]. The simulated doses, both ionizing and non-ionizing, for the ENUBET decay tunnel as a function of distance from the beam axis are depicted in Fig. 4.36. The radius considered for the ENUBET tunnel in 2017 was set to 1 m, where a fluence of non-ionizing particles (scaled to 1 MeV equivalent neutrons) of $1.8 \times 10^{11}/\text{cm}^2$ is expected to accumulate during the lifetime of the experiment. Irradiation tests were performed on the SiPMs to evaluate their survival after being exposed to such doses. The ionizing dose, which would not exceed 0.06 kGy, is relevant for the choice of the plastic scintillator, but does not represent a threat for the

photosensors.

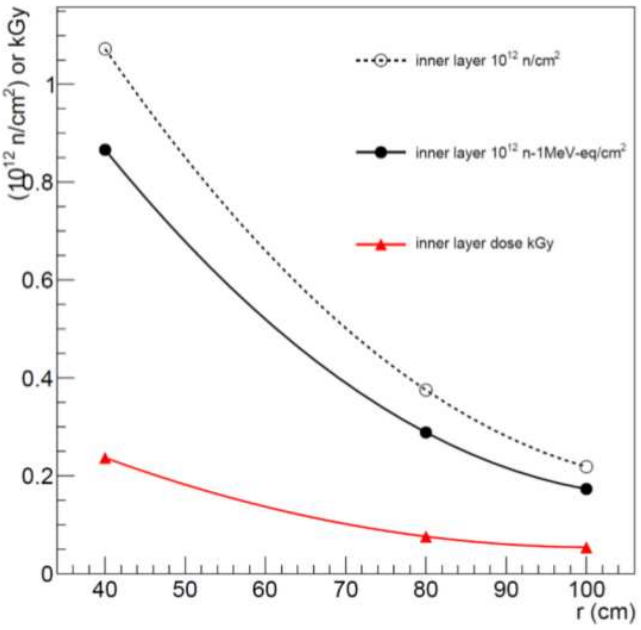

Figure 4.36: Ionizing and non-ionizing doses as a function of the distance between the axis of the ENUBET decay tunnel and the inner radius of the calorimeter [136].

4.6.1 Irradiation tests in Legnaro

The irradiation tests have been performed at INFN-LNL (Laboratori Nazionali di Legnaro), at the CN van der Graaff accelerator. The CN is a vertical accelerator, 7 m tall, installed in 1961 [161]. The CN maximum terminal working voltage, achieved at the high voltage terminal placed on top, is 7 MV, but the working point is set at 5.5 MV which uniformly decreases to 0 V at floor level (Fig. 4.37).

Protons and other light nuclei can be accelerated up to 5 μA currents. The neutrons necessary for the tests were produced with a beam of protons impinging on a Beryllium target, from the reactions Be(p,nx), in detail ^{9}Be(p,n)^{9}B, ^{9}Be(p,np)2α, ^{9}Be(p,np)^{8}Be and ^{9}Be(p,nα)^{5}Li. The experimental area, where the irradiated sample was located, is shielded by concrete walls followed by a shield of water, used as neutron moderator (Fig. 4.38).

The neutron flux in the forward direction, as evaluated from [162], has two peaks, at 0.5 and 3 MeV, for 5 MeV protons impinging on the target. The irradiated samples were three PCBs used for the readout of the ENUBET UCM, hosting 9 SiPMs with a cell size of 20, 15, 12 μm, plus an additional PCB hosting a single 1 mm^2 SiPM with 12 μm cell size. All the samples were irradiated with doses starting from 1.8×10^8 n/cm^2 up to 1.7×10^{11} n/cm^2.

Figure 4.37: The CN accelerator column is shown in this picture, where the 7 MV high voltage terminal dome may be seen at the top (picture courtesy by Andrea Alessio) [161].

Figure 4.38: (left) The irradiation test area at INFN-LNL before the installation of the samples. The Be target is visible in the center of the picture. (right) Experimental area and the setup to record the dark current and the waveform of the SiPMs between two irradiation sessions [136].

No bias was applied to the samples during the irradiation runs. Current scans as a function of the voltage bias (I-V curves) were performed in between each irradiation run, after both the irradiation area and the sample had reached room temperature. The current registered by the PCB hosting one 12 μm cell SiPM (Fig. 4.39) was a ninth of the current registered by the 9 SiPMs PCB with the same cell size, validating the normalization of the signal of the 9 20 μm SiPMs to one (Fig. 4.40). As expected, the SiPM with 12×12 μm^2 cell size displayed lower currents.

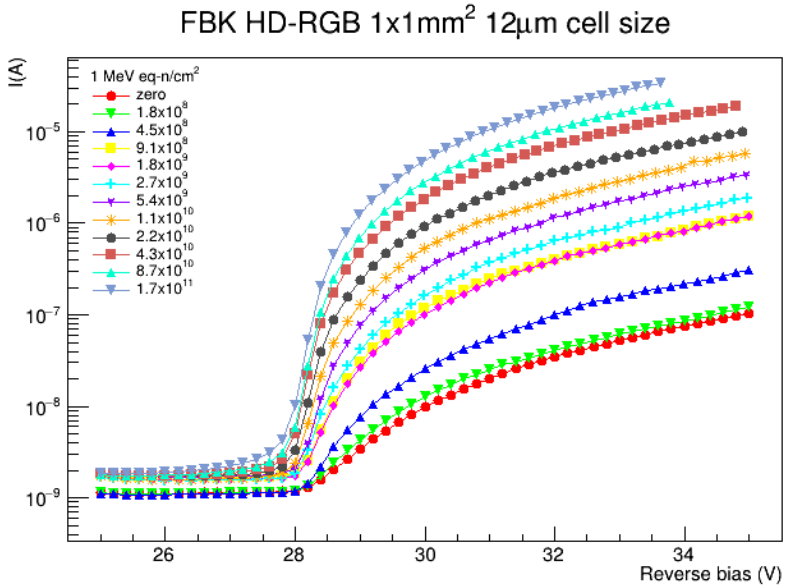

Figure 4.39: I-V curve of the single-SiPM PCB, 12 μm cell size [136].

4.6.2 Test of the irradiated boards with the ENUBET UCM at the CERN PS-T9 beamline

The irradiated boards were then tested at the CERN PS-T9 beamline in October 2017. The ENUBET UCMs were equipped with both irradiated and non irradiated PCBs and exposed to a mixed beam of negative particles (e^-, μ^-, π^-), in order to assess the response to electrons and MIPs. The tests were performed with the 15 μm PCB irradiated up to 1.2×10^{11} n/cm^2 and an identical non irradiated one. Two ENUBET UCM prototypes were used:

- a reference ENUBET UCM, assembled from 5 15 mm thick 3×3 cm^2 iron tiles and 5 EJ-200 5 mm thick scintillator tiles. The holes for the WLS fibers (Y11) were drilled with a CNC machine;

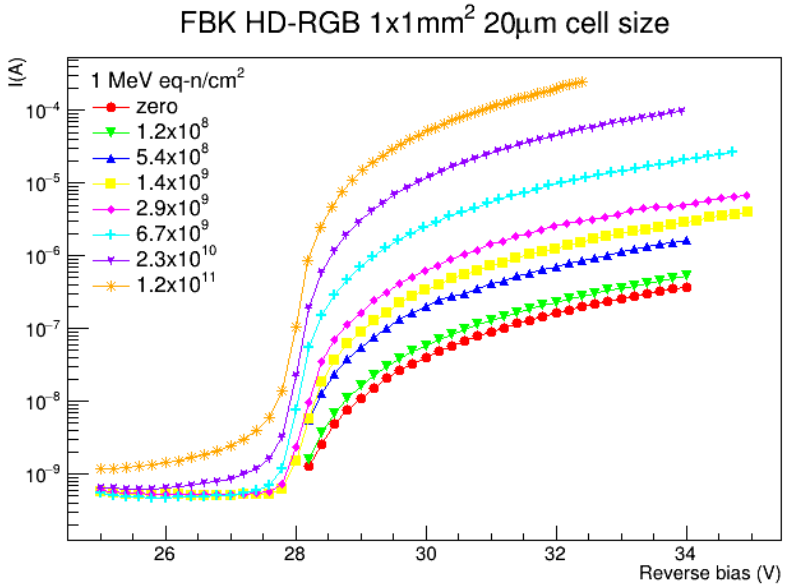

Figure 4.40: I-V curve of the 20 μm SiPM (current of a 9 SiPM PCB divided by 9) [136].

- a UCM with the same absorbing tiles as the reference one, but with scintillator tiles produced by Uniplast, Russia [163]. The scintillator slabs are built with a mold, holes for WLS fiber included, so there was no necessity to drill them. They were 4.5 mm thick and were placed in groups of 3 between the absorbing tiles, for a total thickness of 13.5 mm.

Figure 4.41 shows the state of the art of the UCM spectrum when using a non irradiated board. In the 5 mm scintillator UCM with the irradiated board the electron peak is still visible above the pedestal peak, while the MIP peak is swamped by the pedestal noise (Fig. 4.42). The primary goal of the ENUBET experiment is to collect the signals from the positrons and the MIP peak is not strictly needed. However, MIPs are useful for real-time signal equalization and monitoring, but also for the identification of muons from kaon decays and beam halo. By increasing the scintillator thickness in order to reach more than 80 photo electrons per UCM, the MIP peak can be recovered. In the case of plastic scintillator, $\sim$ 10 mm are enough to reach the desired signal. This is evident from the signal collected inside the 13.5 mm scintillator UCM equipped with an irradiated board, in which the MIP peak is separated from the pedestal one (Fig. 4.43).

4.6.3 Signal loss in irradiated SiPMs

The 13.5 mm thick scintillator UCM allowed to study how much of the signal amplitude was lost due to irradiation. Due to a damage on the epoxy layer of the irradiated SiPMs,

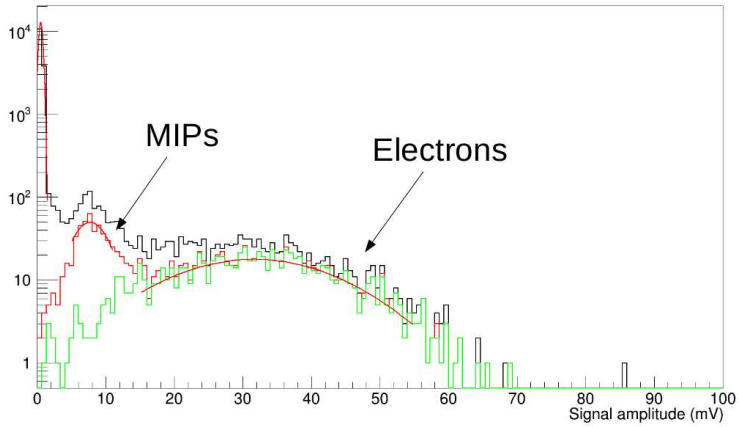

Figure 4.41: Signal from electrons and MIPs inside a UCM with 5 mm thick scintillator tiles, readout by a non-irradiated board [136].

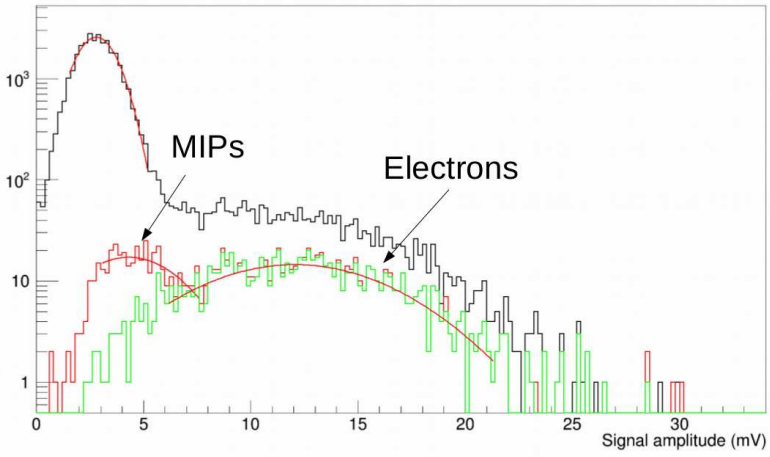

Figure 4.42: Signal from electrons and MIPs inside a UCM with 5 mm thick scintillator tiles, readout by an irradiated board [136].

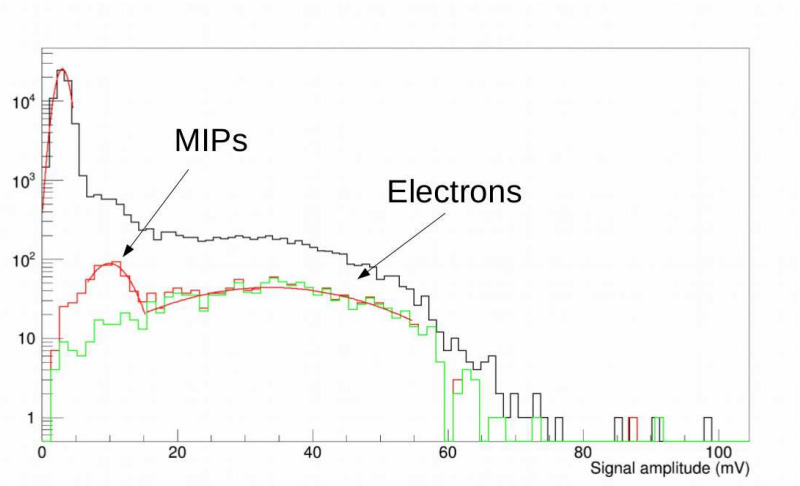

Figure 4.43: Signal from electrons and MIPs inside a UCM with 13.5 mm thick scintillator tiles, readout by an irradiated board [136].

the screws that kept the irradiated board in place were kept a bit loose, in order not to press down the SiPMs on the 3D mask and on the WLS fibers. Figure 4.44 shows the electron peak position as a function of the voltage applied to the SiPMs. The values at 37 V for 3 and 4 GeV/c beam momentum are missing due to saturation.
In Fig. 4.45 the same was done for the MIP peak. For this measurement only runs at 1 and 3 GeV/c beam momentum were available at all SiPM voltages. The reason is that for some runs a special "electron only" trigger was employed, by including in the trigger also the signal from the Cherenkov counter identifying the electrons. This was necessay to accumulate statistics for other detectors tested at the same time as this UCM.
The ratio between the signal of the irradiated board and the non irradiated one is the same for both electrons and MIPs, about 30% (Fig. 4.46), so the SiPMs do not display saturation due to the reduction of the number of the working pixels.
A second quick scan was performed after repositioning the irradiated board and tightening the screws that kept the PCB in place. This time the signal from the irradiated board was recorded to be about 40% of the non-irradiated one (Table 4.2).

4.7 Alternative materials

In 2017, along with the SiPM survival to irradiation, different materials for the shashlik calorimeter were also tested. Given the dimensions of the final calorimeter, one goal was to

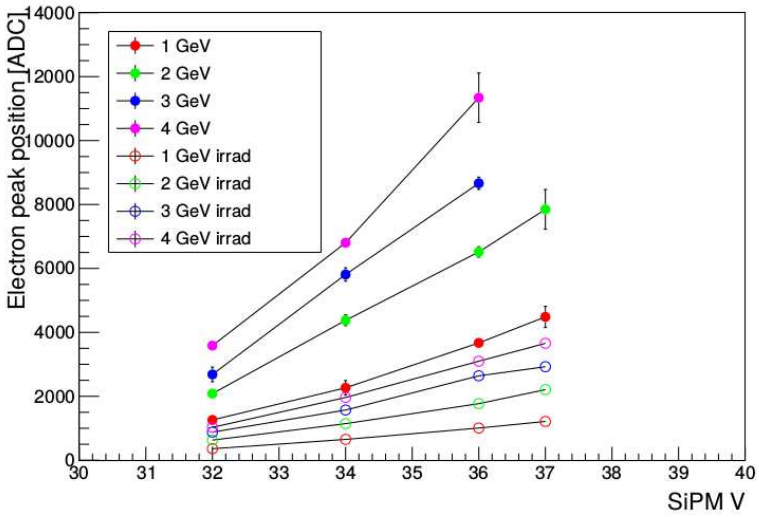

Figure 4.44: Electron peak position in the 13.5 mm thick scintillator UCM with the irradiated and non-irradiated board as a function of the bias of the SiPMs.

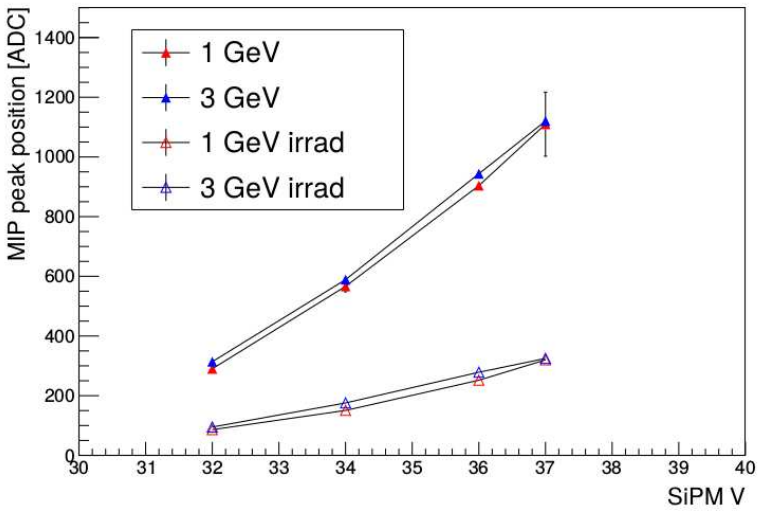

Figure 4.45: MIP peak position in the 13.5 mm thick scintillator UCM with the irradiated and non-irradiated board as a function of the bias of the SiPMs.

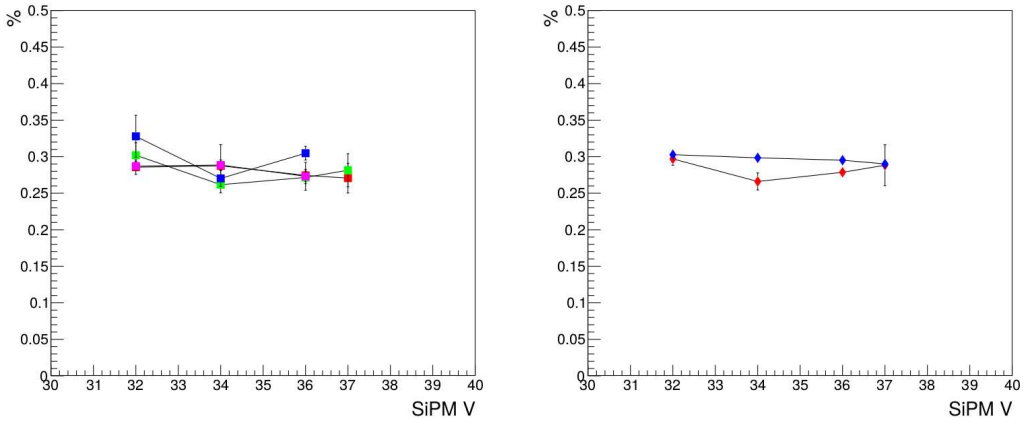

Figure 4.46: (left) Ratio between the electron signal acquired with the irradiated board and the signal acquired with the non-irradiated one. (right) Ratio between the MIP signal acquired with the irradiated board and the signal acquired with the non-irradiated one.

Energy [GeV]	e^- non-irrad	e^- irrad after repositioning	% irrad after rep / non-irrad
1	3671 ± 90	1472 ± 41	40%
2	6517 ± 163	2497 ± 64	38%
4	11341 ± 774	4004 ± 152	35%

Table 4.2: Electron peak position after the irradiated board repositioning.

increase the ease of construction. Moreover, given the particle rate inside the decay tunnel, another improvement to investigate was to obtain faster signals.

4.7.1 Polysiloxane (October 2017)

An interesting alternative to standard plastic scintillators is the polysiloxane [164], [165]; it is more radiation hard to ionizing doses and it is liquid at moderately high temperatures. For this reason, it can be poured around the fibers between the iron slabs and cooled. At room temperature, the scintillator is solid and optically well coupled with the fibers. There is hence no need to drill or cast the polysiloxane, greatly simplifying the construction process. One drawback of the use of the polysiloxane based scintillators is that they have a light yield that is 30% of the one of the EJ-200. A $\sim 12\ X_0$ calorimeter was tested in October at the CERN PS-T9 beamline (Fig. 4.47). The absorbing tiles were 15 mm thick as the previous prototypes, whereas the scintillating ones in polysiloxane were 15 mm thick, 3 times the EJ-200 tiles. The calorimeter was instrumented with Y11 multi-clad WLS fibers of 1 mm diameter by Kuraray and the SiPMs had a $20 \times 20\ \mu m^2$ cell size and a breakdown voltage of 28 V.

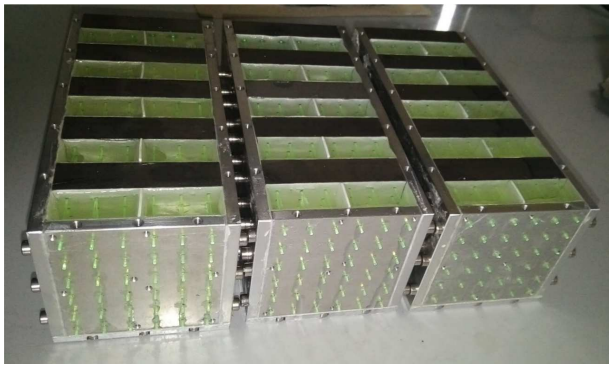

Figure 4.47: The three layers of the polysiloxane calorimeter, without the readout PCBs.

Different values of overvoltage were applied to the SiPMs. The energy resolution was not affected by this, as it is dominated by the sampling term and yielded a similar performance as the calorimeter based on EJ-200 (Fig. 4.48 left). The results showed that the quality of the scintillator-fiber coupling after the cool down at room temperature is comparable with standard scintillators and the process of deposit and hardening of the scintillator does not introduce non-uniformities in the tiles (Fig. 4.48 right).

4.7.2 Uniplast (July 2017)

Another alternative method to have the scintillator tiles without having to cut and drill every piece is to cast them with a mold with the wanted shape and size, for example $3 \times 3\ cm^2$

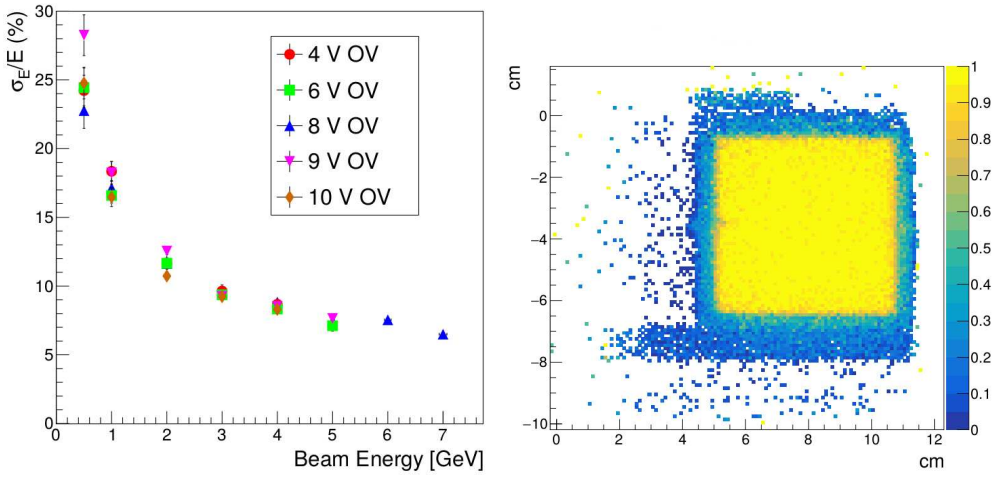

Figure 4.48: (left) Energy resolution for the polysiloxane calorimeter at different overvoltages of the SiPMs. (right) The efficiency map of the polysiloxane calorimeter.

tiles with 9 holes for the WLS fibers. The scintillator, in liquid state, is poured into the mold and then cooled until it becomes solid and is removed from the mold. Uniplast provided scintillator tiles to the ENUBET Collaboration that were 4.5 mm thick, which were placed in between the 15 mm thick iron tiles in a $\sim 12\ X_0$ calorimeter (Fig. 4.49). The energy resolution is dominated by the sampling term in this prototype too and does not deviate significantly from the standard calorimeter with EJ-200 (Fig. 4.50).

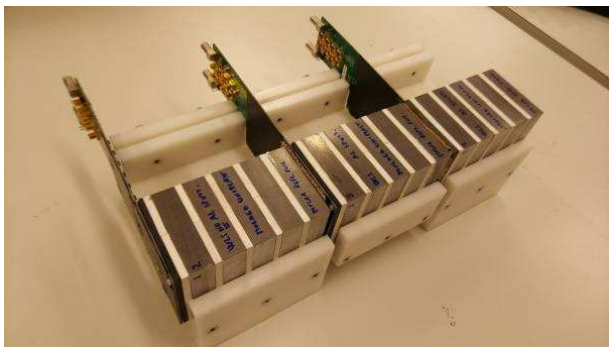

Figure 4.49: The $\sim 12\ X_0$ Uniplast calorimeter, completed with the readout PCBs.

4.7.3 EJ-204 calorimeter (October 2017)

Along with the polysiloxane calorimeter, in October 2017 another prototype with 10 mm thick tiles of EJ-204 plastic scintillator was tested. The EJ-204 is produced by Eljen Technology like the EJ-200, but with a larger scintillation efficiency, combined with high speed

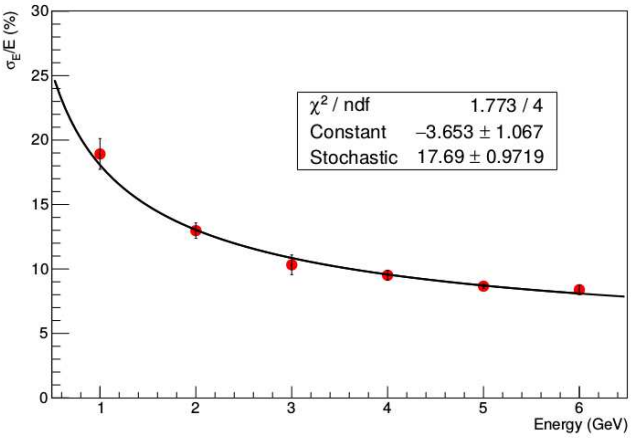

Figure 4.50: Energy resolution of the Uniplast calorimeter.

and good attenuation length. EJ-204 matches the BCF-92 fibers better than the EJ-200. The $\sim 12\ X_0$ was built following the scheme of the previous prototype, with the same 15 mm thick slabs of iron as absorbing material and the same fiber frequency. The used SiPMs, by FBK [140], had a $20 \times 20\ \mu m^2$ cell size and $1 \times 1\ mm^2$ active area. This prototype displayed similar results in terms of energy resolution as the previous prototypes.

Figure 4.51: The $\sim 12\ X_0$ EJ-204 calorimeter.

4.8 2017 conclusions

In 2017, it was assessed that for irradiations $\leq 10^{11}$ n/cm^2 the electron (positron) peak properties remained unmodified and the MIP peak was still visibile above the baseline if the photoelectrons produced by a particle in a UCM were ≥ 150.
It was proved that polysiloxane can be used for shashlik calorimeters, as the fibers-gel

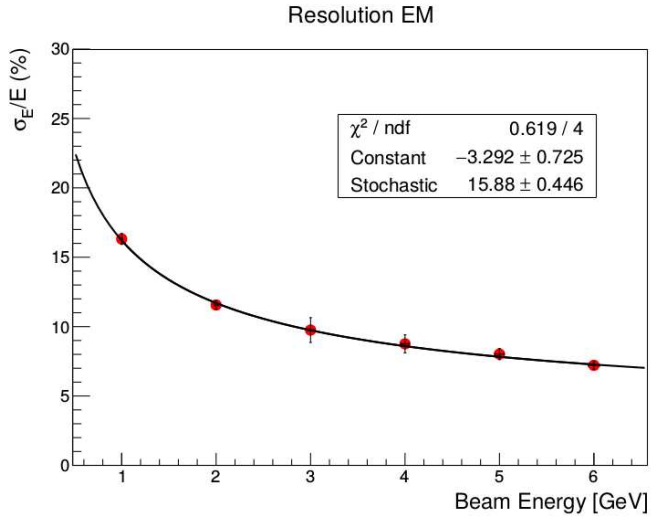

Figure 4.52: Energy resolution of the EJ-204 calorimeter.

coupling did not deteriorate the light yield.
For all the tested calorimeters, the sampling term dominated the energy resolution. The values of the energy resolution for all the tested prototypes are summarized in Table 4.3.

Prototype	Energy resolution (%)
Polysiloxane + iron + 32 V on SiPMs	17.15 ± 0.30
Polysiloxane + iron + 34 V on SiPMs	16.51 ± 0.21
Polysiloxane + iron + 36 V on SiPMs	16.57 ± 0.46
Polysiloxane + iron + 37 V on SiPMs	17.24 ± 0.25
Polysiloxane + iron + 38 V on SiPMs	16.12 ± 0.23
Uniplast + iron	17.69 ± 0.97
EJ-204 + iron	15.88 ± 0.45

Table 4.3: Energy resolution of the 12 UCM calorimeter prototypes tested in 2017.

Conclusions and future perspectives

The neutrino cross sections at the $\sim$ GeV energy scale are currently known with a sensitivity of $O(10\%)$. These large uncertainties affect the measurement of phenomena like the CP violation in the leptonic sector, which could help to explain the predominance of matter over antimatter. The main source of uncertainty is the fact that, in conventional neutrino experiments, the initial neutrino flux is unknown and is deduced from hadron production data and beam simulations.
The ENUBET project aims at proving that a sensitivity of $O(1\%)$ is achievable by measuring the neutrino flux directly inside an "active" decay tunnel. In the K_{e3} decay ($K^+ \rightarrow e^+ \pi^0 \nu_e$) an electron neutrino is emitted with a positron. The flux of the neutrinos can be computed counting the number of positrons produced inside the decay tunnel. If the tunnel is short enough ($\sim$ 50 m), the K_{e3} is the only source of electron neutrinos for a K^+ beam. The ENUBET project involves both the simulation of the hadron beamline, which collects and focuses the K^+, and the construction of prototypes for the active decay tunnel, instrumented with longitudinally segmented shashlik calorimeters in order to perform particle ID and separate the e^+ from the π^+ background.
This thesis work was dedicated to the assessment of the performances of the calorimeter prototypes for the ENUBET decay tunnel. The prototypes were tested at the CERN PS-T9 beamline with a mixed beam of e^-, μ^-, π^- and characterized in terms of linearity and energy resolution. The prototyping activity from July 2016 to October 2017 can be divided into two phases:

- after the feasibility proof of August 2015 of the longitudinal segmentation of a shashlik calorimeter, in 2016 the prototypes were tested in order to assess that the chosen technology met the requirements of the ENUBET project. The energy resolution of both the tested calorimeters (a 12 UCM calorimeter and a "supermodule" one) was $\sim 17\%/\sqrt{E}$, below the $20\%/\sqrt{E}$ set as goal of the project; the same result was obtained with the calorimeter positioned in a "decay tunnel mode" with a 100 mrad tilt angle from the axis beam, showing that the energy resolution was maintained for the average angle of positron emission in the K_{e3} decay;

- the compact readout based on SiPMs allows to segment the shashlik calorimeters,

but exposes the photodetectors to fast neutrons produced by hadronic showers. In 2017 the collaboration performed some irradiation tests in order to assess the SiPM survival to radiation. Moreover new materials were tested, mainly with the goal of easing the construction of the final ~ 50 m detector; the possibility to obtain faster signals was also investigated.
The PCBs hosting the SiPMs were irradiated at the CN van der Graaff accelerator in INFN-LNL; the PCBs were then assembled with several UCM prototypes with different scintillator thickness, whose performace was tested at the CERN PS-T9 beamline. The results showed that, after exposing the SiPMs to a fluence $\leq 10^{11}$ n/cm^2, both the electron and the MIP signals are preserved if a particle produces ≥ 150 photoelectrons inside a UCM.
Among the alternative materials, the polysiloxane was particularly interesting, as its use allows for great simplification of the construction process. The polysiloxane is liquid at room temperature, so it can be poured between the tiles of iron and around the WLS fibers and then, by applying heat, it becomes solid. The scintillator tiles hence are produced without cutting and drilling the material. The tests proved that this material can be used for a shashlik calorimeter, as the fibers-gel coupling did not deteriorate the light yield.
Another calorimeter was assembled with Uniplast tiles; this scintillator too does not require cutting or drilling, as the tiles were casted with a mold of the required size and shape (3×3 cm^2 with 9 holes for the WLS fibers). The last tested ENUBET prototype had EJ-204 scintillating tiles and BCF92 as WLS fibers, assembled to explore the possibility of obtaining faster signals. For all the tested prototypes the sampling term was always the same and the stochastic term of the energy resolution was dominated by it, yielding for all the calorimeters a value of $\sim 16-17\%/\sqrt{E}$.

5.1 Future perspectives

The number of energy tail catcher layers was 3 in the "supermodule" tested in November 2016 and was supposed to be 6 in the final tunnel (see Fig. 3.3), but the latest simulations have shown that a good e/π separation can be maintained even without the energy tail catcher. In a simulation in which a beam of K^+ was injected in the tunnel, the reconstruction efficiency for K_{e3} events was approximately stable at $\sim 25\%$ for tunnel configurations that included from 6 to 0 energy tail catcher layers. By injecting into the tunnel a sample of π^+ that mimicked the π^+ produced by K^+ decays, it was tested how many of these events were mistagged as K_{e3} events with a variable number of energy tail catcher layers. As reported in Table 5.1, the variation of these values, in a range of 0-6 layers, is negligible.
These results hinted to the possibility of reducing or even discarding the energy tail catcher layers, in favor of improving the electromagnetic ones. With a less thick and complicated

Hadronic layers	K_{e3} eff (%)	pure π^+ eff (%)	S/N
6	24.2 ± 0.3	2.6 ± 0.1	1.14
5	24.9 ± 0.3	2.5 ± 0.1	
4	24.7 ± 0.3	2.7 ± 0.1	
3	25.4 ± 0.3	2.8 ± 0.1	
2	25.6 ± 0.3	2.7 ± 0.1	
1	26.1 ± 0.3	2.9 ± 0.1	
0	26.8 ± 0.3	2.9 ± 0.1	1.04

Table 5.1: Tagging efficiencies in the decay tunnel simulated with a different number of energy tail catcher layers. The K_{e3} were selected in a simulation that included all the K^+ decays, while the mistagging "efficiency" of the π^+ mistaken for K_{e3} decays was performed by injecting in the decay tunnel only π^+ that mimicked the energy and the angle emission of those produced in K^+ decays [166].

structure, there is the possibility of bringing the light outside the structure of the calorimeter and at outer radii of the decay tunnel. In this way, the SiPMs are farther from the zones of the calorimeter more subject to radiation, reducing considerably the risk of damage, and are accessible for maintenance. With this perspective in mind, two prototypes of a non shashlik calorimeter were tested in May 2018 and September 2018.

5.1.1 Non shashlik prototypes

In May 2018 the first non shashlik prototype was tested at the CERN PS-T9 beamline. The absorbing iron tiles were 1.5 cm thick and the EJ-204 scintillating ones were 0.5 cm thick. Both had an area of 3×3 cm^2. For each scintillating tile, two WLS fibers were positioned laterally for the light readout (Fig. 5.1).

Every 5 scintillating tiles, the WLS fibers were bundled together on top of the calorimeter and read by a 4×4 mm^2 SiPM (Fig. 5.2). In this way, this prototype had the same longitudinal segmentation (every 4.3 X_0) of its shashlik predecessors and was composed of 18 "UCM like" sub-modules. The positioning of the sub-modules was similar to the one in the 12 UCM prototypes (3 longitudinal layers), but with an extra vertical layer (Fig. 5.3).

The results for the energy resolution reported a stochastic term of $\sim 15.5\%/\sqrt{E}$ and a constant term of $\sim 9\%$ (Fig. 5.4). The reason for such a substantial constant term is still under evaluation.

A bigger (84 channels) prototype of a non-shashlik calorimeter was tested in September 2018 (Fig. 5.5). The data analysis of this prototype is still ongoing.

By the end of 2018, the ENUBET Collaboration will decide which technology will be used for the final prototype, a 3 m $\times \pi$ calorimeter. The next steps needed for the tagger devel-

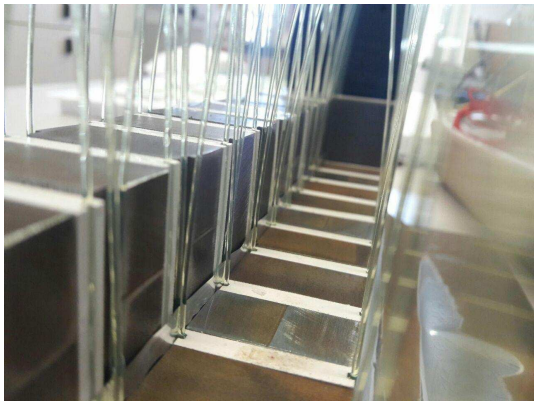

Figure 5.1: Detail of the May 2018 prototype. The WLS fibers collect the light from the sides of the scintillating tiles.

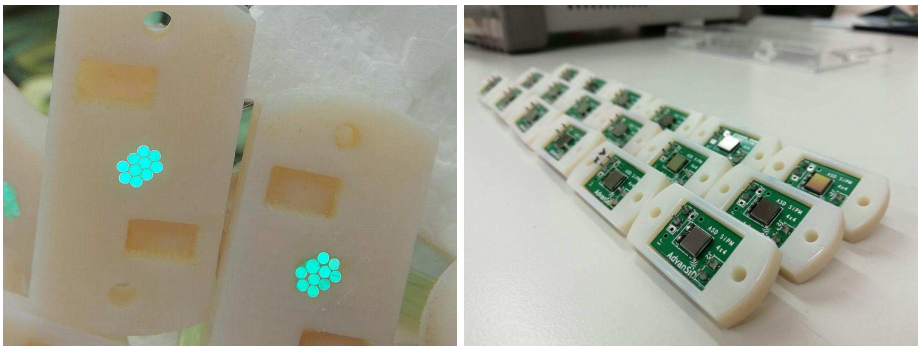

Figure 5.2: (left) Bundling of the 10 fibers that read 5 scintillating tiles. (right) The 4×4 mm^2 SiPMs used for the readout.

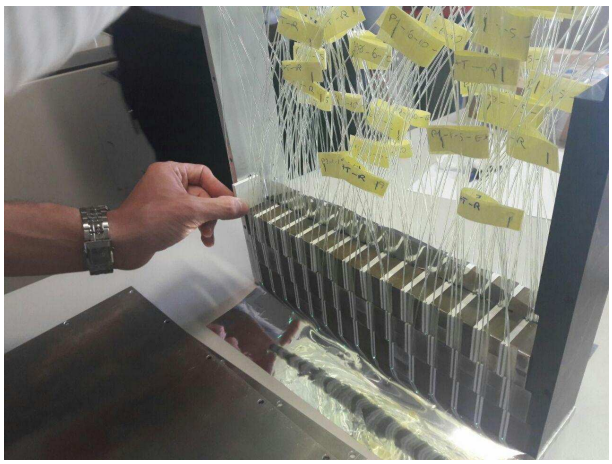

Figure 5.3: The full prototype. The longitudinal and transversal dimensions are the same of the 12 UCM calorimeter, but this prototype had an additional vertical layer.

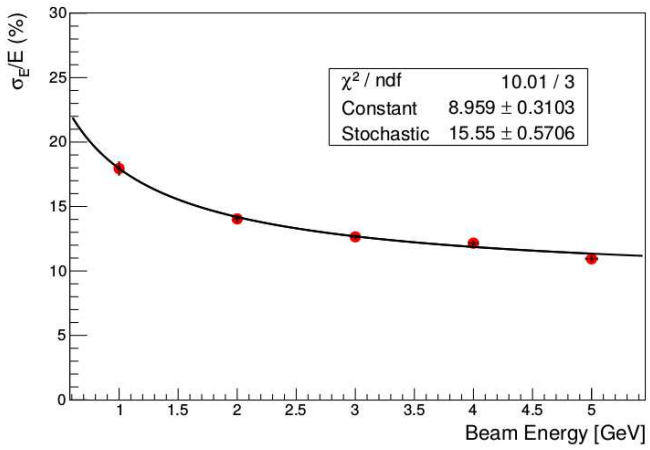

Figure 5.4: Energy resolution of the 18 channels non shashlik calorimeter.

opment include the finalization of the readout electronics (the custom waveform digitizers) and the algorithm used to analyse the waveform acquired with the triggerless acquisition required by the experiment. The algorithm must be able to handle the possible pile-up of signals, correctly reconstructing superimposed ones.

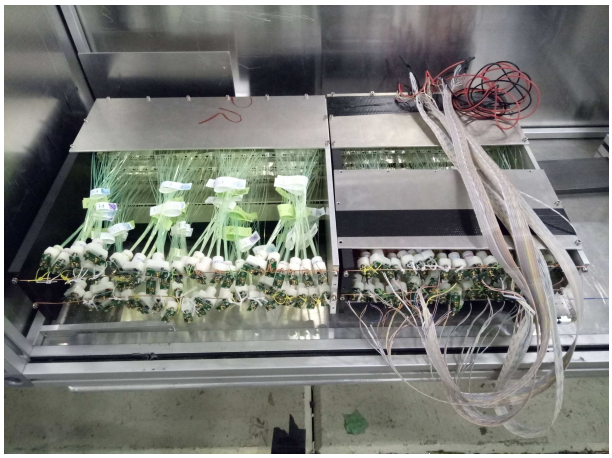

Figure 5.5: The full non shashlik prototype tested in September 2018.

Appendix A

Electromagnetic calorimetry

Calorimeters can be divided in two categories: electromagnetic, to measure electrons and photons via their electromagnetic interactions (bremsstrahlung, pair production), or hadronic, to measure hadrons through their strong and electromagnetic interactions.
Depending on the construction technique, they can be divided into sampling calorimeters and homogeneous calorimeters. In sampling calorimeters the layers of absorbing material, used to degrade the energy of the incoming particle, are alternated with layers of active material, which provide the detectable signal. In homogeneous calorimeter, the absorbing and active material coincide [83].
Since the ENUBET prototypes are shashlik calorimeters, a type of sampling calorimeter, and are used to measure electromagnetic showers, this appendix is dedicated to the description of electromagnetic showers and to the different contributions to the energy resolution of such calorimeters.
For a complete description of calorimetry, see [83].

A.1 Main parameters of the electromagnetic shower

To understand the development of an electromagnetic shower it is useful to know the various mechanisms of energy loss that operate at different energies. Figure A.1 shows the average energy loss by electrons in lead and Fig. A.2 presents the photon interaction cross section as a function of energy.
It is possible to distinguish three energy regimes:

- at low energies, electrons lose energy in collisions with the atoms and molecules of the calorimeter material, ionizing them or producing thermal excitation. For the photons, the main processes for energy loss are the Compton scattering and the photoelectric effect;

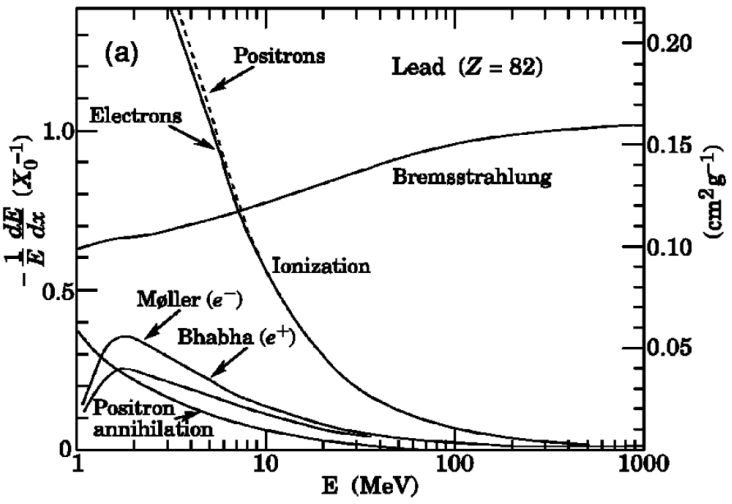

Figure A.1: Fractional energy lost in lead by electrons and positrons as a function of energy [167].

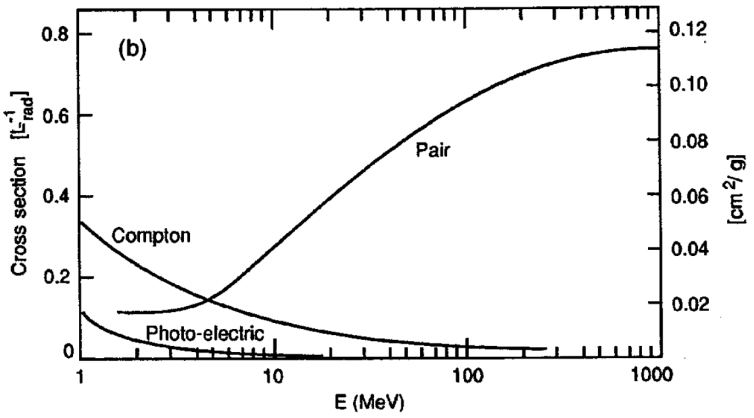

Figure A.2: Photon interaction cross section in lead as a function of energy [168].

- for energies above ~ 10 MeV, electrons lose energy mainly via bremsstrahlung, while photons produce electron-positron pairs;
- above 1 GeV these two processes become energy independent.

These three regimes explain how an electromagnetic shower develops. Starting with an electron or photon with energy > 1 GeV, when it interacts with the calorimeter material it produces secondary photons via bremsstrahlung or pairs of electrons and positrons respectively. These particles create other particles with the same mechanisms and produce a shower of particles with smaller and smaller energies. The number of particles increases until the energy of the electron component falls below a critical energy ε; below this limit, the energy is dissipated via ionization and excitation and no more particles are produced (Fig. A.3).

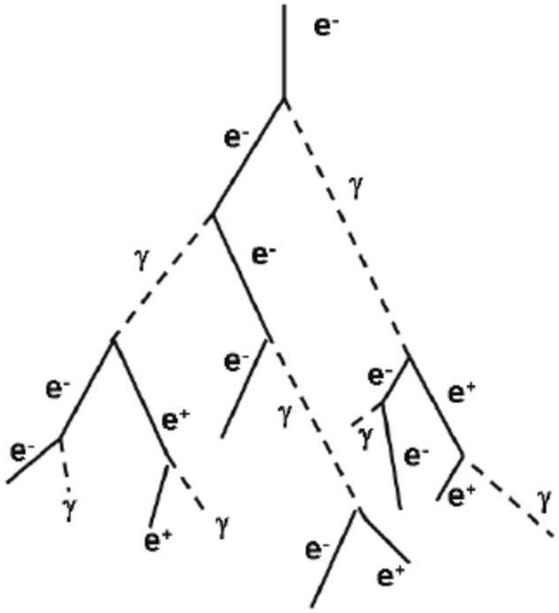

Figure A.3: Schematic diagram of an electron initiated electromagnetic shower [169].

The longitudinal and lateral size of an electromagnetic shower can be described in terms of the radiation length X_0, which depends on the material features [167]:

$$X_0(\mathrm{g/cm^2}) \simeq \frac{716\ \mathrm{g\ cm^{-2}} A}{Z(Z+1)\ln(287/\sqrt{Z})} \tag{A.1}$$

where Z is the atomic number and A is the atomic weight. X_0 describes the rate at which the electrons lose energy by bremsstrahlung. It is used to calculate the average distance x travelled by an electron in a material before its original energy E_0 is reduced to $1/e$ only via bremsstrahlung:

$$\langle E(x)\rangle = E_0 e^{-x/E_0} \tag{A.2}$$

The critical energy ε has two different definitions. ε can be defined as the energy at which the electron ionization losses and bremsstrahlung losses become equal; for solid (gases), this becomes:

$$\varepsilon = \frac{610(710)\ \text{MeV}}{Z + 1.24(0.92)} \tag{A.3}$$

ε can be defined also as the energy at which the ionization loss per X_0 equals the electron energy E [170] :

$$\frac{dE}{dx}(\text{ionization}) = \frac{E}{X_0} \tag{A.4}$$

The two definitions are equivalent in the approximation:

$$\frac{dE}{dx}(\text{bremsstrahlung}) \simeq \frac{E}{X_0} \tag{A.5}$$

As far as the transverse size of the electromagnetic shower is concerned, the main processes that contribute to it are the multiple scattering of electrons and positrons and the emission angle of the bremsstrahlung photons. The parameter that is used to describe the transverse size is the Molière radius (R_M):

$$R_M(\text{g/cm}^2) \simeq 21\ \text{MeV}\frac{X_0}{\varepsilon(\text{MeV})} \tag{A.6}$$

which represents the average lateral deflection of electrons at the critical energy after crossing one radiation length. The Molière radius depends only on the material.

A.2 The energy resolution for electromagnetic calorimeters

The assumption underlying the measurement of the energy of a particle with a calorimeter is that the energy released in the detector is proportional to the initial energy of that particle. The total track length of the shower T_0, given by the sum of all the ionization tracks of all the charged particles of the shower, is proportional to:

$$T_0(\text{g/cm}^2) \propto X_0 \frac{E_0}{\varepsilon} \tag{A.7}$$

in which E_0/ε gives the number of particles in the shower. In this equation, the measurement of the charge released by a shower (for example in the form of light in a scintillating material), gives a measurement of the original particle energy E_0.
The intrinsic energy resolution in an ideal calorimeter (which has infinite dimensions and

perfect response to signals, no disuniformities etc.) is given by T_0. From purely statistical arguments [83], the energy resolution hence is:

$$\sigma(E) \propto \sqrt{T_0} \tag{A.8}$$

from which

$$\frac{\sigma(E)}{E} \propto \frac{1}{\sqrt{T_0}} \propto \frac{1}{\sqrt{E_0}} \tag{A.9}$$

can be derived. In a realistic calorimeter, the energy resolution is deteriorated by other contributions and can be written as:

$$\frac{\sigma}{E} = \frac{a}{\sqrt{E}} \oplus \frac{b}{E} \oplus c \tag{A.10}$$

where $\oplus$ indicates the quadratic sum. On the right hand side of the equation, the terms are called, from left to right: the stochastic term, the noise term ad the constant term (Fig. A.4). Depending on the energy of the incident particle, the three terms have a different relative importance.

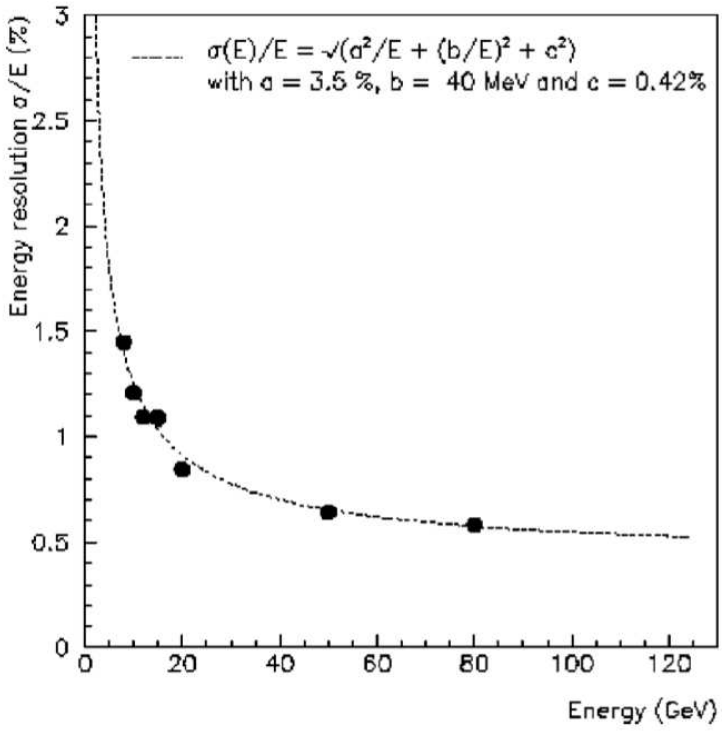

Figure A.4: The energy resolution as a function of the energy measured with a prototype of the NA48 liquid krypton electromagnetic calorimeter [171]. The line is a fit to the experimental points with the form and the parameters indicated in figure.

The stochastic term The stochastic term is given by the intrinsic fluctuations related to the physical development of the shower. If the calorimeter is homogeneous, these fluctuations are small, because the energy deposited in the active material, which coincides with the absorbing one, does not fluctuate event by event.
In sampling calorimeters, since the two materials are not the same one, these fluctuations, in this case called "sampling fluctuations", are more important. They are due to the variation in the number of charged particles N_{ch} across the active layers. N_{ch} is proportional to:

$$N_{ch} \propto \frac{E_0}{t} \tag{A.11}$$

where t is the thickness of the absorber layers in radiation lengths. If the absorbing layers are not too thin, it is possible to assume that the crossings of the active layers are statistically independent. This allows to write the stochastic term for a sampling calorimeter as:

$$\frac{\sigma}{E} \propto \frac{1}{\sqrt{N_{ch}}} \propto \sqrt{\frac{t}{E_0(\mathrm{GeV})}} \tag{A.12}$$

The noise term This term comes from the electronic noise of the readout chain and is linked to the type of detector that is used to collect the signal. If the signal is collected in the form of light, it is possible to keep the electronic noise small, because the used photosensitive devices, such as phototubes, have a high-gain multiplication of the original signal with low to almost no noise. On the other hand, if the signal is collected in the form of charge, the first element of the readout chain is a preamplifier and the electronic noise is larger.

The constant term This term includes all the contributions that do not depend on the energy of the particle but only on disuniformities in the calorimeter response. These disuniformities can be given by the detector geometry, such as layers with irregular shapes, by imperfections in the detector mechanical structure and readout system, by temperature gradients, radiation damage, aging of the detector, etc.

Appendix B

The Cherenkov Counters of the CERN-T9 beamline

A Cherenkov counter is a device that uses Cherenkov radiation to detect and identify charged particles of known momentum. Cherenkov radiation is the radiation emitted when a charged particle travels through a medium at a velocity v that is larger than the phase velocity of light in that medium. Cherenkov counters are composed of a transparent substance (i.e. a gas confined in a tank or tube) in which a particle can have $v > c/n$ (c being the speed of light in vacuum and n the refractive index of the medium), an optical system which focuses the light (Fig. B.1) and photomultiplier tubes to convert the light pulse into an electric signal [172].

Figure B.1: Part of the tube and the optical system of Cherenkov counter B in the T9 beamline at CERN.

The T9 line in the East Area at CERN has two Cherenkov counters. Beam Cherenkov A (BCA) is the upstream counter and is a 5 m long tube, while Beam Cherenkov B (BCB), 2.5 m long, is placed downstream [173]. The pressure of the gas (CO_2 or air) can be set manually up to 3.5 bar, the maximum safe operating pressure. The pressure inside the Cherenkov counters determines which particles produce Cherenkov light in the gas, requiring higher pressure for more massive particles. During the ENUBET beam test in July 2016, a pressure scan was performed in order to assess the signal response and Cherenkov light emission efficiency of the two Cherenkov counters with different particles (electrons and muons) and at different pressures. The following results were obtained analysing both the Cherenkov light emission and the ENUBET calorimeter energy spectrum.

B.1 Data analysis and plots

The mixed beam of electrons, muons and pions in the T9 line is obtained from the interaction of protons accelerated in the PS with a fixed target.
The experimental setup, from upstream to downstream, was composed of:

- Beam Cherenkov A filled with CO_2;
- Beam Cherenkov B filled with CO_2;
- a 10×10 cm^2 plastic scintillator for the trigger;
- two silicon strip detectors (SSD) for the track reconstruction;
- the calorimeter;
- 24 cm of iron;
- a 15×15 cm^2 plastic scintillator.

The events considered in the analysis had to hit both the SSDs, be single cluster on the SSDs to avoid ambiguity, impact the upstream surface of the calorimeter in an area of 3×3 cm^2 around the center of the surface itself and be tagged as either muons or electrons by the Cherenkov counters.
The pressure scan was performed at 2 GeV/c and 3 GeV/c; the threshold for the Cherenkov light emission from muons in CO_2 is 3.38 bar at 2 GeV/c and 1.51 bar at 3 GeV/c, while for the electrons is 0 bar at both energies. The Cherenkov A was kept at 2.3 bar for reference, while in the Cherenkov B the pressure was set to the following values: 0.2, 0.5, 0.8, 1.1, 1.4, 1.7, 2.0 and 2.3 bar.
The tests showed that the signal increases until it reaches 4000 ADC, when the counter saturates. This is clearly visible observing the response of the electrons, at both 2 and 3 GeV/c, whereas for muons a momentum of 3 GeV/c and a pressure of 2.3 bar did not

yield enough light to saturate the counter. However, the muon signal at 3 GeV/c (1.7, 2.0 and 2.3 bar) showed the same correlation with pressure as the electron signal (0.2, 0.5, 0.8, 1.1 bar) not only at 3 GeV/c but also at 2 GeV/c. A linear fit over these two ranges provided a slope equal to 3065±16 for electrons at 2 GeV/c, 3063±32 for electrons at 3 GeV/c, 3093±50 for muons at 3 GeV/c.
The results are plotted in Fig. B.2 and B.3.

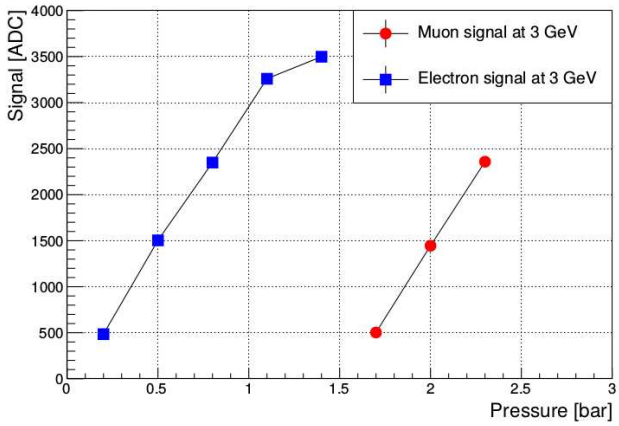

Figure B.2: Signal vs pressure at 3 GeV, for electrons (blue squares) and muons (red dots).

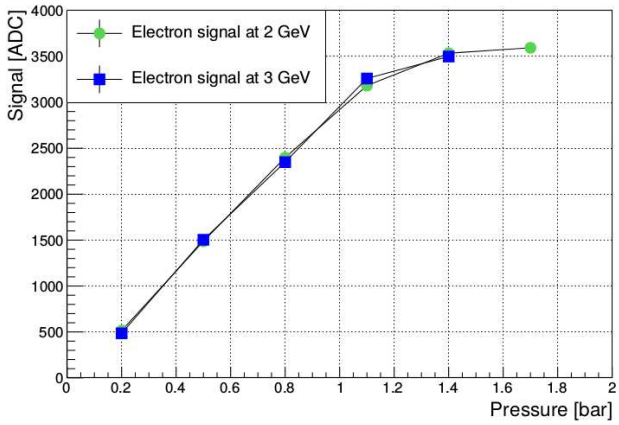

Figure B.3: Comparison between the signal of 2 GeV electrons (green dots) and 3 GeV electrons (blue squares).

The efficiency was computed by taking the BCA as fixed reference. The efficiency of Cherenkov light emission for electrons is plotted in Fig. B.4; at 2 GeV/c BCB is slightly more efficient than at 3 GeV/c, in particular at lower pressure, with a difference of less than

3.5% at most, observed at 0.2 bar. At both energies, BCB is more efficient at higher pressures, those closer to the pressure inside BCA.
The efficiency for muons is plotted in Fig. B.5.

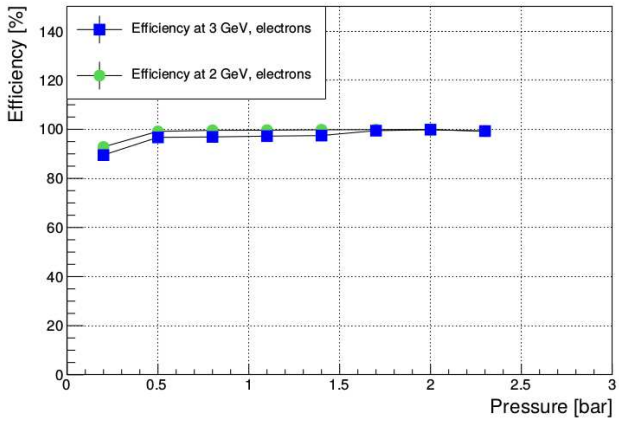

Figure B.4: Light emission efficiency for the electrons at 2 and 3 GeV/c.

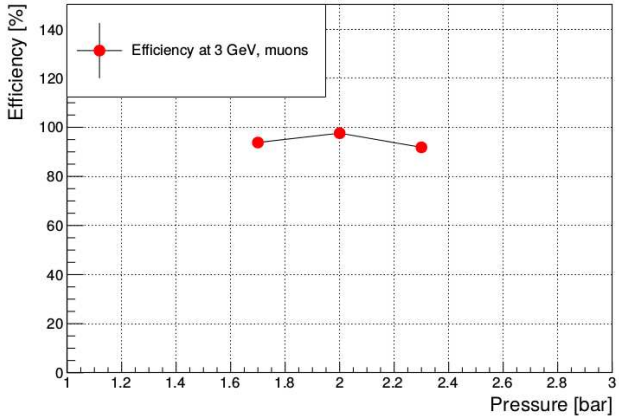

Figure B.5: Light emission efficiency for muons at 3 GeV/c.

List of acronyms

AC	Alternating Current
ADC	Analog to Digital Converter
AGS	Alternating Gradient Synchrotron
AMANDA	Antarctic Muon And Neutrino Detector Array
ANITA	ANtarctic Impulsive Transient Antenna
ANL	Aragonne National Laboratory
ANTARES	Astronomy with a Neutrino Telescope and Abyss environmental RESearch project
ArgoNeuT	Argon Neutrino Test
ASIC	Application Specific Integrated Circuit
BNL	Brookhaven National Laboratory
BR	Branching Ratio
CAMAC	Computer Automated Measurement And Control
CC	Charged Current
CERN	Conseil Européen pour la Recherche Nucléaire
CKP	Cocconi-Koester-Perkins
CL	Confidence Level
CMS	Compact Muon Solenoid
CNC	Computer Numerical Control
CNGS	Cern Neutrinos to Gran Sasso
CP	Charge Parity
CPT	Charge Parity Time
CSNV	Commissione Scientifica Nazionale 5
DAQ	Data AcQuisition
DESY	Deutsches Elektronen-SYnchrotron
DIF	Decay In Flight
DUNE	Deep Underground Neutrino Experiment
EM	ElectroMagnetic
ENUBET	Enhanced NeUtrino BEams from kaon Tagging
ERC	European Research Council

FACTOR	Fiber Apparatus for Calorimetry and Tracking with Optoelectronic Read-out
FBK	Fondazione Bruno Kessler
FNAL	Fermi National Accelerator Laboratory
FORTE	Fast On-orbit Rapid Recording of Transient Events
GEANT4	GEometry ANd Tracking 4
GENIE	Generates Events for Neutrino Interaction Experiments
GLUE	Goldstone Lunar Ultra-high-energy Neutrino Experiment
HiRes	High Resolution Fly's Eye detector
HyperK	Hyper-Kamiokande
HD-RGB	High Density - Red Green Blue
IceCube	IceCube Neutrino Observatory
IDEAS	Integrated Detector Electronics AS
IHEP	Institute of High Energy Physics
ILL	Institut Laue-Langevin
INFN	Istituto Nazionale di Fisica Nucleare
J-PARC	Japan Proton Accelerator Research Complex
K2K	KEK to Kamioka
KEK	Kō Enerugī Kasokuki Kenkyū Kikō (The High Energy Accelerator Research Organization)
LAMPF	Los Alamos Meson Physics Facility
LEP	Large Electron-Positron collider
LEMO	LÉon MOuttet connector
LNL	Laboratori Nazionali di Legnaro
MC	Monte Carlo
MCX	Micro CoaXial connector
MINERνA	Main Injector Experiment for ν-A
MiniBooNE	Mini Booster Neutrino Experiment
MINOS	Main Injector Neutrino Oscillation Search
MIP	Minimum Ionizing Particle
MPV	Most Probable Value
NA	North Area
NC	Neutral Current
NCE	Nuclear Counter Effect
NIM	Nuclear Instrumentation Module
NuMI	Neutrinos at the Main Injector
NuTeV	Neutrinos at the TeVatron
NOMAD	Neutrino Oscillation MAgnetic Detector
NoνA	NuMI Off-Axis ν_e Appearance
particle ID	particle IDentification
PCB	Printed Circuit Board

PMNS	Pontecorvo-Maki-Nakagawa-Sakata
PMT	PhotoMultiplier Tube
POT	Protons On Target
ppp	protons-per-pulse
PS	Proton Synchrotron
QDC	Charge to Digital Converter
RAM	Random Access Memory
RICE	Radio Ice Cherenkov Experiment
SCENTT	Shashlik Calorimeters for Electron Neutrino Tagging and Tracing
SciBooNE	SciBar Booster Neutrino Experiment
SEM	Scanning Electron Microscopes
SiPM	Silicon PhotoMultipliers
SM	Standard Model
SPS	Super Proton Synchrotron
SSD	Silicon Strip Detector
T2K	Tokai to Kamioka
TeV	TeVatron
UCM	Ultra Compact Module
VME	Versa Modular Eurocard
VRB	VME Readout Board
WANF	West Area Neutrino Facility
WLS	WaveLength Shifting

Bibliography

[1] P. Lipari, *Introduction to neutrino physics*, CERN-CLAF School of high-energy physics, Itacuruca, Brazil, 6-19 May, 2001: Proceedings, p. 115-199, 2001

[2] P. Hernández, *Neutrino physics*, CERN-2016-005, 2016

[3] E. Fermi, *Trends to a theory of beta radiation (In Italian)*, Nuovo Cim., vol. 11, p. 1-19, 1934

[4] H. Bethe, R. Peierls, *The 'neutrino'*, Nature, vol. 133, p. 532, 1934

[5] B. Pontecorvo, *Inverse beta process*, Camb. Monogr. Part. Phys. Nucl. Phys. Cosmol., vol. 1, p. 25-31, 1991

[6] F. Reines, C. L. Cowan, *The neutrino*, Nature, vol. 178, p. 446-449, 1956

[7] C. L. Cowan, F. Reines et al., *Detection of the free neutrino: a confirmation*, Science, vol. 124, p. 103-104, 1956

[8] R. Arns, *Detecting the neutrino*, Phys. Perspect., vol. 3, p. 314, 2001

[9] F. Reines, C. Cowan, *The Reines-Cowan experiments: detecting the poltergeist*, Los Alamos Science, vol. 25, p. 4-27, 1997

[10] J. Street, E. Stevenson, *New evidence for the existence of a particle of mass intermediate between the proton and electron*, Phys. Rev., vol. 52, issue 9, p. 1003, 1937

[11] G. Danby et al., *Observation of high-energy neutrino reactions and the existence of two kinds of neutrinos*, Phys. Rev. Lett., vol. 9, p. 36, 1962

[12] https://www.nobelprize.org/prizes/physics/1988/9557-the-hunt-for-the-muon-neutrino/

[13] K. A. Olive et al., *Review of Particle Physics*, Chin. Phys. C, vol. 38, p. 090001, 2014

[14] K. Assamagan et al., *Upper limit of the muon-neutrino mass and charged pion mass from momentum analysis of a surface muon beam*, Phys. Rev. D, vol. 53, p. 6065-6077, 1996

[15] R. Barate et al., *An upper limit on the tau-neutrino mass from three-prong and five-prong tau decays*, Eur. Phys. J. C, vol. 2, p. 395-406, 1998

[16] H. V. Klapdor-Kleingrothaus, H. Päs, A. Y. Smirnov, *Neutrino mass spectrum and neutrinoless double beta decay*, Phys. Rev. D, vol. 63, p. 073005, 2001

[17] J. A. Formaggio, G. P. Zeller, *From eV to EeV: neutrino cross sections across energy scales*, Rev. Mod. Phys., vol. 84, p. 1307, 2012

[18] D. Z. Freedman, D. N. Schramm, D. L. Tubbs, *The weak neutral current and its effects in stellar collapse*, Annual Review of Nuclear Science, vol. 27, p. 167-207, 1977

[19] D. Akimov et al., *Observation of coherent elastic neutrino-nucleus scattering*, Science, vol. 357, issue 6356, p. 1123-1126, 2017

[20] A. Cocco, G. Mangano, M. Messina, *Probing low energy neutrino backgrounds with neutrino capture on beta decaying nuclei*, J. Phys.: Conf. Ser., vol. 110, issue 8, p. 082014, 2008

[21] S. Weinberg, *Universal neutrino degeneracy*, Phys. Rev., vol. 128, p. 1457, 1962

[22] F. Reines, H. S. Gurr, H. W. Sobel, *Detection of* $\overline{\nu}_e - e$ *scattering*, Phys. Rev. Lett., vol. 37, p. 315, 1976

[23] J. Navarro, *Early attempts to detect the neutrino at the Cavendish Laboratory*, Phys. Perspect., vol. 8, issue 1, p. 64, 2006

[24] A. Hoummada et al., *Neutrino oscillations I.L.L. experiment reanalysis*, Appl. Rad. Isot., vol. 46, issues 6-7, p. 449, 1995

[25] H. Kwon et al., *Search for neutrino oscillations at a fission reactor*, Phys. Rev. D, vol. 24, p. 1097, 1981

[26] G. Zacek et al., *Neutrino-oscillation experiments at the Gösgen nuclear power reactor*, Phys. Rev. D, vol. 34, p. 2621, 1986

[27] V. Kuvshinnikov et al., *Precise measurement of the cross section for the reaction* $(\nu - bar)e + p \rightarrow n + e^+$ *at a reactor of the Rovno nuclear power plant*, JETP Lett., vol. 54, p. 253, 1991

[28] G. S. Vidyakin et al., *Detection of antineutrinos in the flux from two reactors*, Sov. Phys. JETP, vol. 66, p. 243, 1987

[29] B. Achkar et al., *Search for neutrino oscillations at 15, 40 and 95 meters from a nuclear power reactor at Bugey*, Nucl. Phys. B, vol. 434, p. 503-532, 1995

[30] Y. Declais et al., *Study of reactor antineutrino interaction with proton at Bugey nuclear power plant*, Phys. Lett. B, vol. 338, issues 2-3, p. 383-389, 1994

[31] G. Mention et al., *Reactor antineutrino anomaly*, Phys. Rev. D, vol. 83, p. 073006, 2011

[32] A. B. McDonald et al. (SNO Collaboration), *Sudbury Neutrino Observatory results*, Physica Scripta, vol. 2005, issue T121, p. 25, 2005

[33] S. E. Willis et al., *Neutrino experiment to test the nature of muon-number conservation*, Phys. Rev. Lett., vol. 44, p. 522, 1980

[34] E. Pasierb et al., *Detection of weak neutral current using fission* $\overline{\nu}_e$ *on deuterons*, Phys. Rev. Lett., vol. 43, issue 2, p. 96, 1979

[35] A. G. Vershinsky et al., *Measurement of the cross sections for the interaction of fission antineutrinos with deuterons at the Rovno atomic power plant*, JETP Lett., vol. 53, p. 513, 1991

[36] Y. Kozlov et al., *Antineutrino-deuteron experiment at the Krasnoyarsk reactor*, Phys. At. Nucl., vol. 63, issue 6, p. 1016-1019, 2000

[37] S. P. Riley et al., *Neutrino-induced deuteron disintegration experiment*, Phys. Rev. C, vol. 59, p. 1780, 1999

[38] K. Nakamura et al. (Particle Data Group), *Review of particle physics*, J. Phys. G, vol. 37, p. 075021, 2010

[39] K. Antipin et al., *Physics results from the Baikal Neutrino Telescope*, Nucl. Phys. B Proc. Suppl., vol. 168, p. 296-298, 2007

[40] V. Aynutdinov et al., *The BAIKAL neutrino experiment: physics results and perspectives*, Nucl. Instrum. Meth. A, vol. 602, p. 14-20, 2009

[41] ANTARES Collaboration, *A deep sea telescope for high energy neutrinos*, eprint arXiv:astro-ph/9907432, 1999

[42] A. Achterberg et al. (IceCube Collaboration), *Five years of searches for point sources of astrophysical neutrinos with the AMANDA-II neutrino telescope*, Phys. Rev. D, vol. 75, p. 102001, 2007

[43] C. P. de los Heros (IceCube Collaboration), *IceCube*, Nucl. Instrum. Meth. A, vol. 630, p. 119-124, 2011

[44] I. Kravchenko et al., *Limits on the ultra-high energy electron neutrino flux from the RICE experiment*, Astropart. Phys., vol. 20, p. 195-213, 2003

[45] N. G. Lehtinen et al., *FORTE satellite constraints on ultrahigh energy cosmic particle fluxes*, Phys. Rev. D, vol. 69, issue 1, p. 013008, 2004

[46] S. W. Barwick et al., *Constraints on cosmic neutrino fluxes from the Antarctic Impulsive Transient Antenna experiment*, Phys. Rev. Lett., vol. 96, p. 171101, 2006

[47] J. Abraham et al., *Upper limit on the diffuse flux of ultrahigh energy tau neutrinos from the Pierre Auger Observatory*, Phys. Rev. Lett., vol. 100, issue 21, p. 211101, 2008

[48] R. U. Abbasi et al., *Measurement of the flux of ultrahigh energy cosmic rays from monocular observations by the High Resolution Fly's Eye experiment*, Phys. Rev. Lett., vol. 92, p. 151101, 2004

[49] P. W. Gorham et al., *Experimental limit on the cosmic diffuse ultrahigh energy neutrino flux*, Phys. Rev. Lett., vol. 93, p. 041101, 2004

[50] J. Madsen et al. (IceCube Collaboration), *Ultra-high energy neutrinos*, XXXVIII International Symposium on Physics in Collision, Bogotá, Colombia, 11-15 September 2018, arXiv:1901.02528 [astro-ph.HE]

[51] M. G. Aartsen et al., *Observation and characterization of a cosmic muon neutrino flux from the northern hemisphere using six years of IceCube data*, Astrophys. J., vol. 883, issue 1, p. 3, 2016

[52] A. M. Ankowski, C. Mariani, *Systematic uncertainties in long-baseline neutrino-oscillation experiments*, J. Phys. G, vol. 44, p. 054001, 2017

[53] T. Katori, M. Martini, *Neutrino-nucleus cross sections for oscillation experiments*, J. Phys. G, vol. 45, p. 013001, 2018

[54] A. Longhin, L. Ludovici, F. Terranova, *A novel technique for the measurement of the electron neutrino cross section*, Eur. Phys. J. C, vol. 75, p. 155, 2015

[55] A. Longhin, *The ENUBET project* , SPSC132, Discussion of Requests Submitted on the Call for Proposals for Projects at the CERN Neutrino Platform after LS2, 2019

[56] ENUBET internal note on simulation, June 2, 2016

[57] ENUBET: publications and presentations available at http://enubet.pd.infn.it/

[58] A. Faessler et al., *Can one measure the Cosmic Neutrino Background?*, International Journal of Modern Physics E, vol. 26, issue 01n02, p. 1740008, 2017

[59] S. E. Kopp, *Accelerator neutrino beams*, Physics Report, vol. 439, issue 3, p. 101-159, 2007

[60] M. Schwartz, *Feasibility of using high-energy neutrinos to study the weak interactions*, Phys. Rev. Lett., vol. 4, p. 306, 1960

[61] B. Pontecorvo, *Electron and muon neutrinos*, J. Exp. Theor. Phys. (U.S.S.R.), vol. 37, p. 1751, 1959 [translation: Sov. Phys. JETP, vol. 10, p. 1236, 1960]

[62] G. Danby et al., *Observation of high-energy neutrino reactions and the existence of two kinds of neutrinos*, Phys. Rev. Lett., vol. 9, p. 36, 1962

[63] H. Wachsmuth, *400 GeV proton-induced prompt neutrinos at 0 and 15 milliradian*, presented at Topical Conference on Neutrino Physics, Oxford, CERN/EP/PHYS 78-29, 1978

[64] R. L. Burman, W. C. Louis, *Neutrino physics at meson factories and spallation neutron sources*, J. Phys. G, vol. 29, p. 2499, 2003

[65] B. Pontecorvo, *'Direct' neutrino production and charmed particles*, Zh. Eksp. Teor. Fiz., vol. 69, p. 452, 1975 [translation: Sov. Phys. JETP, vol. 42, issue 2, p. 229, 1975]

[66] K. Kodama et al., *Observation of tau neutrino interactions*, Phys. Lett. B, vol. 504, p. 218, 2001

[67] M. Giesch et al., *Status of magnetic horn and neutrino beam*, Nucl. Instrum. Meth., vol. 20, p. 58, 1963

[68] G. Plass, B. Kuiper, *Fast beam extraction and the external proton beam*, CERN informal workshop on neutrino physics, CERN-63-37, p. 83-96, 1963

[69] R. L. Kustom et al., *Quasielastic neutrino scattering*, Phys. Rev. Lett., vol. 22, p. 1014, 1969

[70] S. van der Meer, *A directive device for charged particles and its use in an enhanced neutrino beam*, CERN-61-07, 1961

[71] J. M. Gaillard, *The Brookhaven neutrino experiment*, CERN Informal Workshop on Neutrino Physics, CERN-63-37, p. 33-42, 1963

[72] R. A. Lundy et al., $\pi^{\pm}$ *and* $K^{\pm}$ *production cross sections for 12.5-BeV Protons on Be*, Phys. Rev. Lett., vol. 14, p. 730, 1965

[73] A. Asner, C. Iselin, *A new focusing system considerably increasing the actual PS-neutrino beam flux intensity*, CERN-65-17, 1965

[74] G. J. Marmer et al., *Differential production cross sections of low-momentum particles from 12.3-BeV/c protons on beryllium and copper*, Phys. Rev., vol. 179, p. 1294, 1969

[75] M. Derrick, *Plans for neutrino experiments with the 12 ft. bubble chamber at the ZGS*, CERN Informal Workshop on Neutrino Physics, CERN-69-28, p. 3-12, 1969

[76] Y. Cho et al., *Pion production in proton-beryllium collisions at 12.5 GeV/c*, Phys. Rev. D, vol. 4, p. 1967, 1971

[77] J. Campbell et al., *Study of the reaction* $\nu p \rightarrow \mu^{-}\pi^{+}p$, Phys. Rev. Lett., vol. 30, p. 335, 1973

[78] A. Mann et al., *Study of the reaction* $\nu n \rightarrow \mu^{-}p$, Phys. Rev. Lett., vol. 31, p. 884, 1973

[79] R. P. Feynman, *Very high-energy collisions of hadrons*, Phys. Rev. Lett., vol. 23, p. 1415, 1969

[80] G. Collazuol, A. Ferrari, A. Guglielmi, P. R. Sala, *Hadronic models and experimental data for the neutrino beam production*, Nucl. Instrum. Meth. A, vol. 449, issue 3, p. 609-623, 2000

[81] Z. Pavlovic, *Studies of the neutrino flux for the NuMI beam at FNAL*, PhD Thesis, University of Texas at Austin, 2008

[82] S. van der Meer, *Neutrino flux calculations* , CERN Informal Workshop on Neutrino Physics, CERN-63-37, p. 97-110, 1963

[83] C. W. Fabjan, F. Gianotti, *Calorimetry for particle physics*, Review of Modern Physics, vol. 75, p. 1243, 2003

[84] M. H. Ahn et al., *Measurement of neutrino oscillation by the K2K experiment*, Phys. Rev. D, vol. 74, p. 072003, 2006

[85] R. Steerenberg et al., *Accelerators for the PS neutrino beam*, J. Phys.: Conf. Ser., vol. 408, issue 1, p. 012058, 2013

[86] P. Adamson et al., *The NuMI neutrino beam*, Nucl. Instrum. Meth. A, vol. 806, p. 279-306, 2016

[87] S. J. Barish et al., *Study of neutrino interactions in hydrogen and deuterium: description of the experiment and study of the reaction* $\nu + d \rightarrow \mu^- + p + p_s$, Phys. Rev. D, vol. 16, p. 3103, 1977

[88] J. M. Pattison, *The CERN neutrino beam*, CERN informal workshop on neutrino physics, CERN-69-28, p. 13-32, 1969

[89] R. Burns et al., *Determination of neutrino flux*, CERN Informal Workshop on Neutrino Physics, CERN-65-32, p. 97-110, 1965

[90] D. G. Baratov et al., *Neutrino beam of the Institute of High Energy Physics VI: systems for optimization and control in neutrino experiments*, Zh. Tekh. Fiz., vol. 48, p. 99, 1978 [translation: Sov. Phys. Tech. Phys., vol. 23, p. 58, 1978]

[91] A. Carroll et al., *Overview of recent focusing horns for the BNL neutrino program*, Proc. IEEE Part. Accel. Conf., Washington, D. C., p. 1731, 1987

[92] D. Beavis et al., *P889: long baseline neutrino oscillation experiment at the AGS*, Report No. BNL-52459, 1995

[93] G. Ferioli, R. Jung, *Evolution of secondary emission efficiencies of various materials measured in the CERN SPS secondary beam lines*, CERN-SL-97-71(BI), Proceedings of Beam Diagnostics and Instrumentation for Particle Accelerators (DIPAC), 1997

[94] G. Tassotto, *Fermilab primary beam instrumentation*, 2^{nd} International workshop on neutrino beams and instrumentation, 6-9 September, 2000

[95] J. Camas et al., *Screens versus SEM grids for single pass measurements in SPS, LEP, and LHC*, CERN SL/95-62 (BI), 1995

[96] G. Plass, K. M. Vahlbruch, H. W. Wachsmuth, *The determination of the spectra of high-energy neutrino parents*, CERN Informal Workshop on Neutrino Physics, CERN-65-32, p. 121-128, 1965

[97] G. Plass, K. M. Vahlbruch, H. W. Wachsmuth, *Test of a spectrometer for intense nanosecond bursts of high-energy particles*, Nucl. Instrum. Meth., vol. 46, p. 223, 1967

[98] S. Kopp et al., *Secondary beam monitors for the NuMI facility at FNAL*, Nucl. Instrum. Meth. A, vol. 568, p. 503-519, 2006

[99] R. Burns et al., *Search for intermediate bosons in high-energy neutrino interactions*, Phys. Rev. Lett., vol. 15, p. 42, 1965

[100] G. Cocconi, L. Koester, D. H. Perkins, LBL Report No. UCRL 10022, p. 167, 1961

[101] D. Bloess et al., *Determination of the neutrino spectrum in the CERN 1967 neutrino experiment*, Nucl. Instrum. Meth., vol. 91, p. 605, 1971

[102] C. Y. Chi et al., *Segmented ionization chambers for high intensity beam measurements*, Nucl. Instrum. Meth. A, vol. 281, p. 448, 1985

[103] A. P. Bugorsky et al., *Muon flux measuring system for neutrino experiments at the IHEP Accelerator*, Nucl. Instrum. Meth., vol. 146, p. 367-371, 1977

[104] J. E. Hill et al., *Beam monitoring and modeling for the K2K long-baseline neutrino oscillation experiment*, Int. J. Mod. Phys., vol. A16S1B, p. 758-760, 2001

[105] G. Cavallari, E. H. M. Heijne, P. Jarron, P. Lazeyras, M. Musso, *Solid state detectors used for the CERN Neutrino Flux Monitoring (NFM)*, IEEE Trans. Nucl. Sci., vol. 25, p. 600, 1978

[106] E. H. M. Heijne, P. Jarron, P. Lazeyras, W. R. Nelson, G. R. Stevenson, *A tiny telescope of Si-detectors for high energy muon flux measurement with electron rejection*, IEEE Trans. Nucl. Sci., vol. 27, p. 272, 1980

[107] E. H. M. Heijne, *Muon flux measurement with silicon detectors in the CERN neutrino beams*, CERN-83-06, 1983

[108] R. Bailey et al., *The CERN neutrino beam to Gran Sasso (NGS)*, Addendum to report CERN 98-02, INFN-AE-98-05, CERN-SL-99-034(DI), INFN-AE-99-05, 1999

[109] J. Park et al. (MINERνA Collaboration), *Measurement of neutrino flux from neutrino-electron elastic scattering*, Phys. Rev. D, vol. 93, p. 112007, 2016

[110] A. Bravar, Talk at Nufact2015, Rio de Janeiro, Brasil, August 10-15, 2015

[111] L. Aliaga et al. (MINERνA Collaboration), *Neutrino flux predictions for the NuMI beam*, Phys. Rev. D, vol. 94, p. 092005, 2016

[112] R. Gran et al. (K2K Collaboration), *Measurement of the quasielastic axial vector mass in neutrino interactions on oxygen*, Phys. Rev. D, vol. 74 , p. 052002, 2006

[113] P. Adamson et al. (MINOS Collaboration), *Neutrino and antineutrino inclusive charged-current cross section measurements with the MINOS near detector*, Phys. Rev. D, vol. 81, p. 072002, 2010

[114] J. Dobson (T2K Collaboration), *T2K cross section measurements*, Nucl. Phys. B Proc. Suppl., vol. 237-238, p. 199-202, 2013

[115] K. Abe et al. (T2K Collaboration), *Measurement of the inclusive ν_μ charged current cross section on carbon in the near detector of the T2K experiment*, Phys. Rev. D, vol. 87, p. 092003, 2013

[116] K. Abe et al. (T2K Collaboration), *Measurement of the inclusive ν_μ charged current cross section on iron and hydrocarbon in the T2K on-axis neutrino beam*, Phys. Rev. D, vol. 90, p. 052010, 2014

[117] Y. Nakajima et al. (SciBooNE Collaboration), *Measurement of inclusive charged current interactions on carbon in a few-GeV neutrino beam*, Phys. Rev. D, vol. 83, p. 012005, 2011

[118] B. G. Tice et al. (MINERvA Collaboration), *Measurement of ratios of ν_μ charged-current cross sections on C, Fe, and Pb to CH at neutrino energies 2-20 GeV*, Phys. Rev. Lett., vol. 112, p. 231801, 2014

[119] R. Acciarri et al. (ArgoNeuT Collaboration), *Measurements of inclusive muon neutrino and antineutrino charged current differential cross sections on argon in the NuMI antineutrino beam*, Phys. Rev. D, vol. 89, p. 112003, 2014

[120] M. Day, K. S. McFarland, *Differences in quasielastic cross sections of muon and electron neutrinos*, Phys. Rev. D, vol. 86, p. 053003, 2012

[121] J. B. Lagrange et al., *Neutrinos from PIon Beam Line, nuPIL**, NUFACT-2015-124, FERMILAB-CONF-16-160-AD, 2015

[122] E. H. M. Heijne, *Muon flux measurement with silicon detectors in the CERN neutrino beams*, CERN-83-06, 1983

[123] S. Agostinelli et al. (GEANT4 Collaboration), *GEANT4: a simulation toolkit*, Nucl. Instrum. Meth. A, vol. 506, p. 250-303, 2003

[124] J. Allison et al., *Geant4 developments and applications*, IEEE Trans. Nucl. Sci., vol. 53, p. 270, 2006

[125] A. Longhin, *ENUBET Enhanced NeUtrino BEams from kaon Tagging*, presentation at the ENUBET kick-off meeting, Padova, 23 June 2016

[126] G. Aad et al. (ATLAS Collaboration), *Photon conversions at $\sqrt{s} = 900 \setminus GeV$ measured with the ATLAS detector*, ATLAS-CONF-2010-007, 2010

[127] F. Hahn et al. (NA62 Collaboration), *NA62 technical design document* , NA62-10-07, 2010

[128] C. Adloff et al. (CALICE Collaboration), *Construction and commissioning of the CALICE analog hadron calorimeter prototype*, JINST, vol. 5, issue 5, p. P05004, 2010

[129] A. Berra et al. (ENUBET Coll.), *Enabling precise measurements of flux in accelerator neutrino beams: the ENUBET project*, CERN-SPSC-2016-036, SPSC-EOI-014, 2016

[130] G. S. Atoian et al., *Lead-scintillator electromagnetic calorimeter with wavelength shifting fiber readout*, Nucl. Instrum. Meth. A, vol. 320, p. 144, 1992

[131] J. Badier et al., *Shashlik calorimetry: a combined Shashlik + preshower detector for LHC*, CERN/DRDC 93-28, DRDC/P50, 1993

[132] A. C. Benvenuti et al. (CALEIDO Collaboration), *An electromagnetic shashlik calorimeter with longitudinal segmentation*, Nucl. Instrum. Meth. A, vol. 432, p. 232-239, 1999

[133] C. Piemonte, *A new Silicon Photomultiplier structure for blue light detection*, Nucl. Instrum. Meth. A, vol. 568, p. 224-232, 2006

[134] B. Dolgoshein et al., *Limited Geiger-mode microcell silicon photo-diode: new results*, Nucl. Instrum. Meth. A, vol. 442, p. 187-192, 2000

[135] A. Meregaglia, *ENUBET: Enhanced NeUtrino BEams from kaon Tagging*, JINST, vol. 11, p. C12040, 2016

[136] ENUBET Collaboration, *Irradiation and performance of HD-RGB SiPM for calorimetric applications*, in preparation for submission to JINST

[137] C. Piemonte et al., *Characterization of the first FBK High-Density cell Silicon Photomultiplier technology*, IEEE Transactions on Electron Devices, vol. 60, issue 8, p. 2567-2573, 2013

[138] A. Berra et al., *A compact light readout system for longitudinally segmented shashlik calorimeters*, Nucl. Instrum. Meth. A, vol. 830, p. 345-354, 2016

[139] A. Berra et al., *Silicon Photomultipliers as a readout system for a scintillator-lead shashlik calorimeter*, IEEE Trans. Nucl. Sci., vol. 58, p. 1297, 2011

[140] Advansid, Povo (TN), Italy, http://advansid.com/

[141] M. Prest et al., *The AGILE silicon tracker: an innovative gamma-ray instrument for space*, Nucl. Instrum. Meth. A, vol. 501, issue 1, p. 280-287, 2003

[142] A. Berra et al., *A non-conventional neutrino beamline for the measurement of the electron neutrino cross section*, arXiv:1512.08202 [hep-ex], 2015

[143] S. J. Alvsvaag et al. (DELPHI STIC Collaboration), *The small angle tile calorimeter in the DELPHI experiment*, Nucl. Instrum. Meth. A, vol. 425, p. 106-139, 1999

[144] http://sba.web.cern.ch/sba/BeamsAndAreas/East/East.htm

[145] R. Brun, F. Rademakers, *ROOT - an object oriented data analysis framework*, Nucl. Instrum. Meth. A, vol. 389, p. 81-86, 1997, see also http://root.cern.ch/

[146] H. Nyquist, *Certain topics in telegraph transmission theory*, Trans. AIEE, vol. 47, p. 617-644, 1928

[147] CAEN S.p.A., Viareggio, Italy

[148] https://ideas.no/

[149] K. S. Kölbig, B. Schorr, *A program package for the Landau distribution*, Computer Phys. Comm., vol. 31, p. 97-111, 1984

[150] A. Berra et al., *Testbeam performance of a shashlik calorimeter with fine-grained longitudinal segmentation*, JINST, vol. 13, issue 1, p. P01028, 2018

[151] T. Skwarnicki, *A study of the radiative cascade transitions between the upsilon-prime and upsilon resonances*, DESY F31-86-02, PhD Dissertation, Appendix E, 1986

[152] A. Berra et al., *Longitudinally segmented shashlik calorimeters with SiPM readout: the SCENTT experiment*, 2016 IEEE NSS/MIC/RTSD workshop, 2016

[153] A. Berra et al., *Shashlik calorimeters with embedded SiPMs for longitudinal segmentation*, IEEE Trans. Nucl. Sci., vol. 64, issue 4, p. 1056-1061, 2017

[154] R. Boanta, *A shashlik calorimeter for the ENUBET instrumented decay tunnel*, Master Thesis, Università degli Studi di Milano-Bicocca, November 2017

[155] L. Durieu, O. Ferrando, *Design of T9 (ATLAS/CMS) for EHNL*, PS/PA Note 96-xx, 1996

[156] Y. Musienko et al., *Radiation damage in Silicon Photomultipliers exposed to neutron radiation*, JINST, vol. 12, issue 7, p. C07030, 2017

[157] M. Cordelli et al., *Neutron irradiation test of Hamamatsu, SensL and AdvanSiD UV-extended SiPMs*, JINST, vol. 13, issue 3, p. T03005, 2018

[158] M. Centis Vignali et al., *Neutron irradiation effect on SiPMs up to* $\Phi_{neq} = 5 \times 10^{14}$ cm^{-2}, Nucl. Instrum. Meth. A, available online [doi:10.1016/j.nima.2017.11.003], 2017

[159] C. Xu, R. Klanner, E. Garutti, W. L. Hellweg, *Influence of X-ray irradiation on the properties of the Hamamatsu Silicon Photomultiplier S10362-11-050C*, Nucl. Instrum. Meth. A, vol. 762, p. 149, 2014

[160] E. Garutti et al., *Silicon Photomultiplier characterization and radiation damage investigation for high energy particle physics applications*, JINST, vol. 9, p. C03021, 2014

[161] http://www.lnl.infn.it/index.php/en/accelerators-3/cn

[162] S. Agosteo et al., *Characterization of the energy distribution of neutrons generated by 5 MeV protons on a thick Beryllium target at different emission angles*, Appl. Rad. Isot., vol. 69, p. 1664, 2011

[163] Uniplast OOO, Vladimir, st. Bolshaya Nizhegorodskaya, 77, Russia

[164] S. Carturan et al., *Novel polysiloxane-based scintillators for neutron detection*, Radiation Protection Dosimetry, vol. 143, p. 471-476, 2010

[165] A. Quaranta et al., *Doped polysiloxane scintillators for thermal neutrons detection*, Journal of Non-Crystalline Solids, vol. 357, issue 8-9, p. 1921-1925, 2011

[166] F. Pupilli et al., *ENUBET: high precision neutrino flux measurements in conventional neutrino beams*, The 19th international workshop on neutrinos from accelerators NUFACT2017 - Working group 3: Neutrino Factories, vol. 295, 2018

[167] Particle Data Group, *Review of Particle Properties*, Phys. Rev. D, vol. 66, 010001(R), 2002

[168] C. W. Fabjan, in *Experimental techniques in high-energy physics*, edited by T. Ferbel (Addison-Wesley, Menlo Park), 1987

[169] P. Rocca, F. Riggi, *The use of avalanche photodiodes in high energy electromagnetic calorimetry*, in book: Advances in Photodiodes, 2011

[170] B. Rossi, *High energy particles*, Prentice Hall, Englewood Cliffs, NJ, 1952

[171] NA48 Collaboration, *LKr calorimetry for the CP violation experiment NA48: recent test beam results*, Nucl. Instrum. Meth. A, vol. 360, p. 224-227, 1995

[172] *The Great Soviet Encyclopedia*, 3rd Edition, 1970-1979

[173] *Instructions for Changing Beam Cherenkov Gas Conditions*,
http://sba.web.cern.ch/sba/Documentations/Eastdocs/docs/T9-Cerenkov-UG.pdf